*Institute of Space and Aeronautical Science, University of Tokyo*
*Report No. 592, March 1981*

# Separated Flow Noise of a Flat Plate

*By*

Yoshiyuki MARUTA* and Susumu KOTAKE

*Abstract*: Flow noise associated with separated flow of a flat plate with large attack angles was studied experimentally to obtain its acoustic characteristics and to understand its generation mechanism. The acoustic features show that the separated flow noise could be attributed to the wall-pressure fluctuations on the plate surface, being of acoustic dipole sources. The time derivatives of fluctuating wall-surface pressure are highly correlated with the associated acoustic pressure. The noise source strength is proportional to the mean-square time-derivative of fluctuating surface pressure and its correlation area, being proportional to the sixth power of the oncoming flow velocity and distributed uniformly over the plate surfaces. The associated acoustic intensity is well predicted with these noise-source strength distributions.

CONTENTS



* Research Laboratory, EBARA Corp., Fujisawa

## NOMENCLATURE

| | |
|---|---|
| $A$ | surface area of plate |
| $A_c$ | correlation area of noise source |
| $a$ | speed of sound |
| $c$ | cord of plate |
| $f$ | frequency |
| $p_0$ | ambient pressure, reference pressure |
| $p_a$ | acoustic pressure |
| $p_f$ | fluctuating pressure in flow |
| $\dot{p}_f$ | time-derivative of pressure in flow |
| $p_s$ | fluctuating surface-pressure |
| $\dot{p}_s$ | time-derivative of surface-pressure |
| $Q$ | noise source strength per unit surface area |
| $R$ | correlation coefficient |
| $r$ | distance from plate to observer |
| $s$ | span of plate |
| $t$ | time, plate thickness |
| $U$ | oncoming flow velocity |
| $X_c$ | chordwise correlation length |
| $Z_c$ | spanwise correlation length |
| $x$ | chordwise distance from leading edge |
| $z$ | spanwise distance from plate center |
| $\alpha$ | attack angle of plate |
| $\theta$ | azimuth of observer |
| $\chi$ | $=90^\circ-(\alpha+\theta)$ |
| $\tau$ | retarded time, $\tau_c=r/a$ |
| $\omega$ | angular frequency |
| $SPL$ | sound pressure level, $10\log(\overline{p_a^2}/\overline{p_{a0}^2})$, $\sqrt{\overline{p_{a0}^2}}=2.0\times10^{-4}$ $\mu$bar |
| $IL$ | surface-pressure level, $10\log(\overline{p_a^2}/\overline{p_{s0}^2})$, $\sqrt{\overline{p_{s0}^2}}=2.0\times10^{-4}$ $\mu$bar |
| $DPIL$ | intensity level of surface-pressure time derivative, $10\log(\overline{\dot{p}_s^2}/\overline{\dot{p}_{s0}^2})$, $\sqrt{\overline{\dot{p}_{s0}^2}}=2\pi\times10^3\times2.0\times10^{-4}$ $\mu$bar/s |
| $QIL$ | source strength level |
| — | time mean |
| $\langle\ \rangle$ | correlation |
| $\cdot$ | time derivative |

Subscripts

| | |
|---|---|
| 0 | ambient, reference |
| $a$ | sound |
| $f$ | flow |
| $s$ | surface |
| $x$ | chordwise |
| $z$ | spanwise |

## 1. Introduction

A new area in fast, safe and economical transport has resulted from the introduction of commercial jet airplanes in the late 1950s, and the associated expansion of air travel has been accompanied by considerable noise problems. The need for quieter airplanes has long been recognized by aircraft and engine manufactures. A considerable amount of research work in this area has been made with much progress, being systematized as "aeroacoustics."

Noise generation by jet engines has been the main subject of these researches. The several noise-generation processes inherent in the jet engine are fairly well understood. The dominant source of noise from early turbojet engines was jet noise generated in the exhaust. At the appearance of high-bypass-ratio turbofan engines, jet exhaust noise was greatly reduced. With this reduced levels of jet noise, fan noise was elevated from a secondary noise source to one of dominant importance. Fan noise is generally characterized by a frequency spectrum which consists of multiples of blade-passing frequencies and a broad-band spectrum. The former has been reduced by careful selection of various engine parameters and by installation of acoustic treatment, but the latter has remained as an important problem to be solved.

The origin of broad-band noise from a body immersed in flow can be attributed to four types of turbulence; (a) incident turbulence, (b) boundary layer turbulence, (c) turbulent vorticity shedding and (d) separated turbulence. Although the first three contributions to the generation of broad-band noise have been rather well understood, there has been little study of noise associated with separated turbulence because of the complexity of its flow structure.

At the design stage, or for well designed fluid-machineries, there is no flow separation expected and hence no appreciable acoustic radiation associated. At part loads, however, flow separation will not be always avoided. Under certain particular operating conditions of jet engine such as at take-off and landing, a separated flow may occur in its air intake and compressor, contributing to higher levels of broad-band noise. In other fluid machinaries or flow systems, separated flows may also occur in a variety of different circumstances and result in much higher noise levels. Thus, it should be of fundamental importance for noise reduction of aircraft as well as of fluid machinaries to investigate the acoustic characteristics of separated flows and its generation mechanism.

In separated flows around a rigid body, the associated noise can be considered to have its origin in fluctuating turbulent stresses in the flow and fluctuating pressures on the wall surface. Curle [*1*] considered the sound radiation from these fluctuating stresses by extending Lighthill's analogy and obtained a mathematical expression of the sound field.

Gordon [*2*, *3*] measured the sound power spectrum radiated by a flat strip spoiler mounted inside a pipe at various attack angles. With the insertion of a spoiler, the broad-band noise was observed to be increased proportionally to the sixth power of the flow velocity. It is also observed that the overall sound power generated by the spoiler may be described quantitatively by the third power of the total pressure drop

across it and that this parameter can be used to correlate the noise data.

Fricke and Stevenson [4] investigated pressure fluctuations in a separated flow behind a thin fence on a wind tunnel wall as an initial detailed study of separated flows, because the configuration gave a well-defined separation point and the most intense pressure fluctuations. Identifying noise sources within the flow, they showed that a stronger type of noise generation might occur in the neighbourhood of the reattachment point and that the similarity relations for the nearfield of a jet or for a conventional boundary layer would give reasonably accurate perdictions of sound levels behind fences.

Based on Curle's formulation for surface-generated noise, Siddon [5] employed a correlation technique to determine the local acoustic source strength on the surface of flat plates and simple airfoils. Flat plate airfoils were located in a jet flow. By measuring the correlation between the local surface pressure and farfield acoustic pressure, the distribution of dipole strength on the surface was evaluated. The result showed distinctively different distributions for cases of incident turbulence, separated flow and vortex shedding, although identified source regions were definitely localized. This correlation method promises to be a powerful diagnostic tool for determing the location and distribution of acoustic sources.

As mentioned above, understanding of separated flows is not sufficient for estimating the fluctuating stresses associated with them, not only because of the everpresent problem of the turbulent structure but also because the mean flow itself is not well understood. This lack of understanding as well as a great variety of boundary conditions of separated flows make it very difficult to select a particular example for study that will yield results of some universality. The separated flow, behind a flat plate with large attack angles was selected for the present experimental study. The objects of the present study are

(1) to obtain the acoustic characteristics of the associated noise—the sound intensity, directivity and spectral density,
(2) to discuss the mechanism of the noise generation by measuring the correlation between the fluctuating pressure in flow and the sound pressure, and
(3) to know the fluid-dynamical features of the acoustic sources to predict the noise field of separated flows.

## 2. Acoustic Characteristics

### 2–1 *Experimental method*

As shown in Fig. 2–1, a flat plate was immersed in a uniform flow with a large attack angle $\alpha$, and the associated sound field was measured. The air stored in a tank at 15 kg/cm$^2$ was released from a nozzle into the ambient air after passing through a diffuser and a strainer. The nozzle had a cross-section of 240 mm$\times$60 mm and gave a uniform velocity over 220 mm$\times$50 mm area at the outlet. The plate was located within the uniform jet flow at the distance of 180 mm from the nozzle outlet (Fig. 2–2). The range of employed jet velocity was 50 m/s to 150 m/s and the associated turbulent velocity was less than 1% of the mean velocity. Behind the

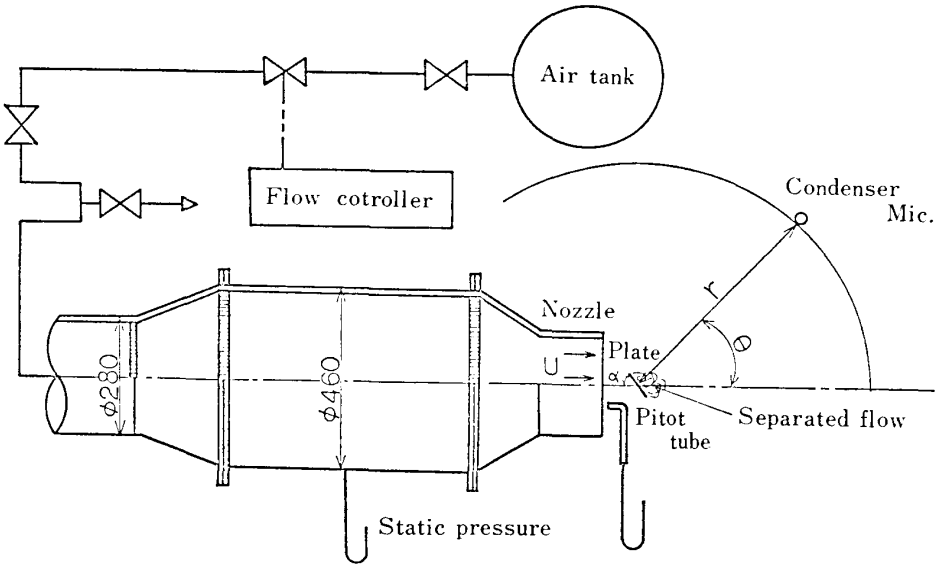


FIG. 2–1. Experimental apparatus for measurement of acoustic field.

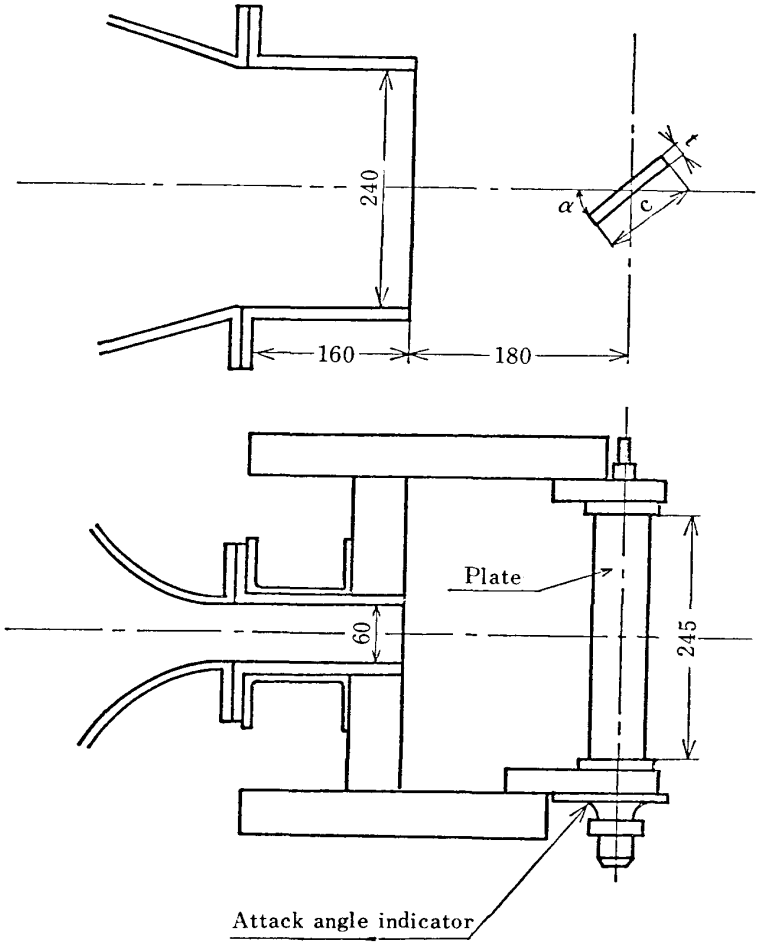


FIG. 2–2. Configuration of plate assembly.

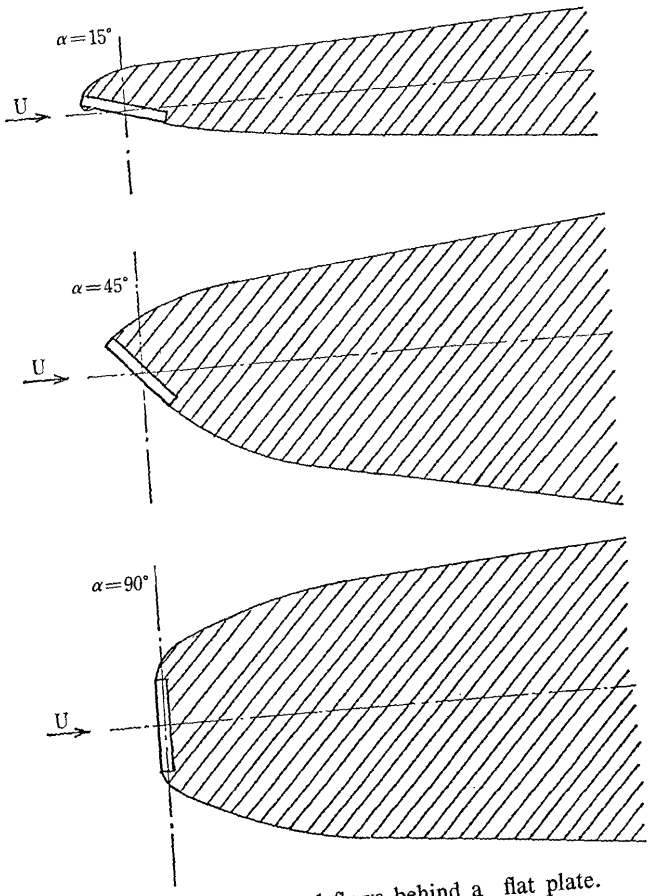


FIG. 2-3. Separated flows behind a flat plate.

plate, turbulent velocities were increased due to the separation of flow. The region where the turbulent velocity was higher than 10% of the local mean velocity was shown in Fig. 2-3 for different attack angles.

Because the plate was located in a jet flow, the span-wise flow variation was likely to cause a three-dimensional effect. After the preliminary experiment with a plate having end-plates in the span-wise direction, such an effect was found to be negligible. The thickness of the plate had no effect on the result provided less than 20% of the chord. For the convenience of surface-pressure measurement, plates 5 mm and 8 mm thick were employed.

The outlet of the jet nozzle was located close to the center of a room of 4 m high as shown in Fig. 2-4. The walls were treated with sound absorptive materials of glasswool 100 mm thick with an air layer 100 mm thick to suppress the major reflections. In Fig. 2-5, the result of an acoustic free-field test is shown in the sound-pressure vs. distance relation. In the space within $r=2.5$ m, acoustic free-field was certified for sound frequencies above 60 Hz. Acoustic pressures were measured mainly at $r=2$ m. Movement of the microphone was limited between azimuths 30° and 120° owing to the jet-nozzle and flow interaction. The background noise level was about 10 dB lower than the noise level under consideration.

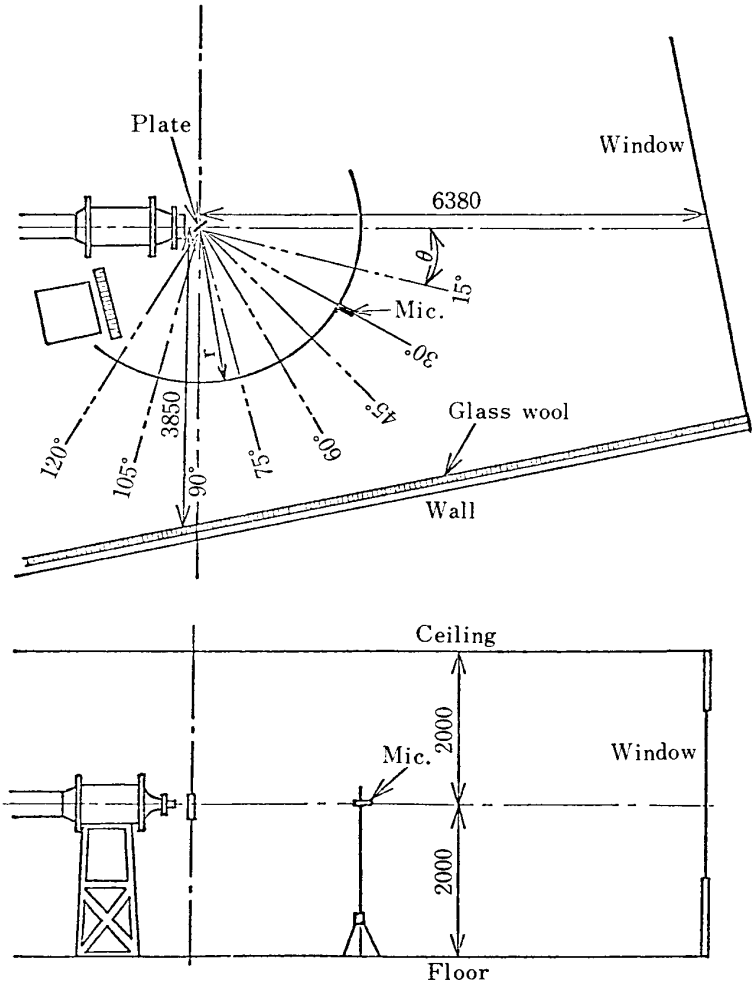


FIG. 2-4. Acoustic environment of experiment.

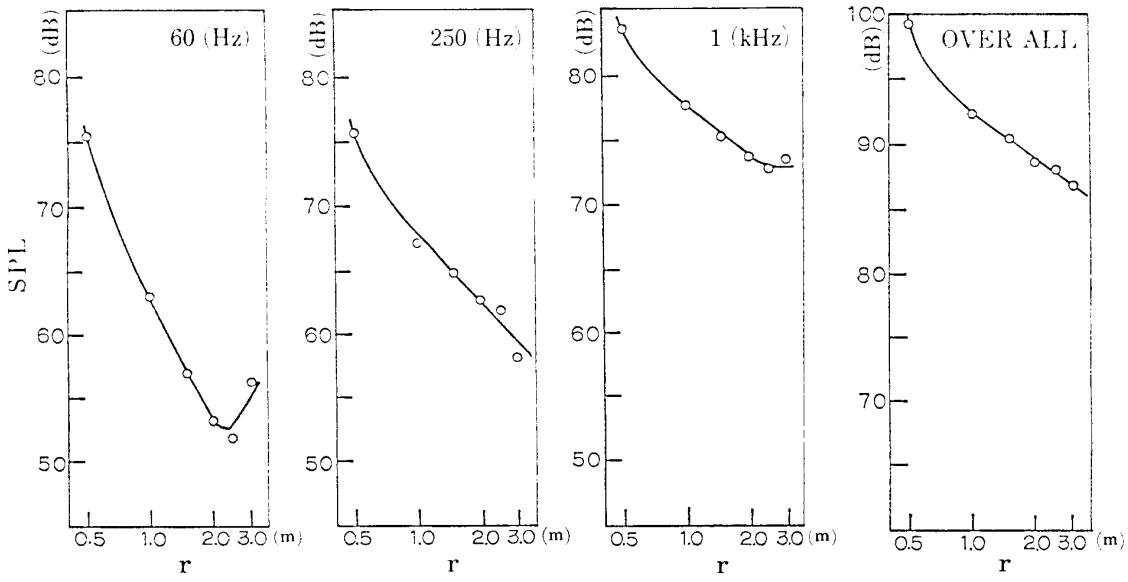


FIG. 2-5. Far-field characteristics; $t \times c = 40 \times 60$, $\alpha = 45°$, $U = 100$ m/s, $\theta = 45°$.

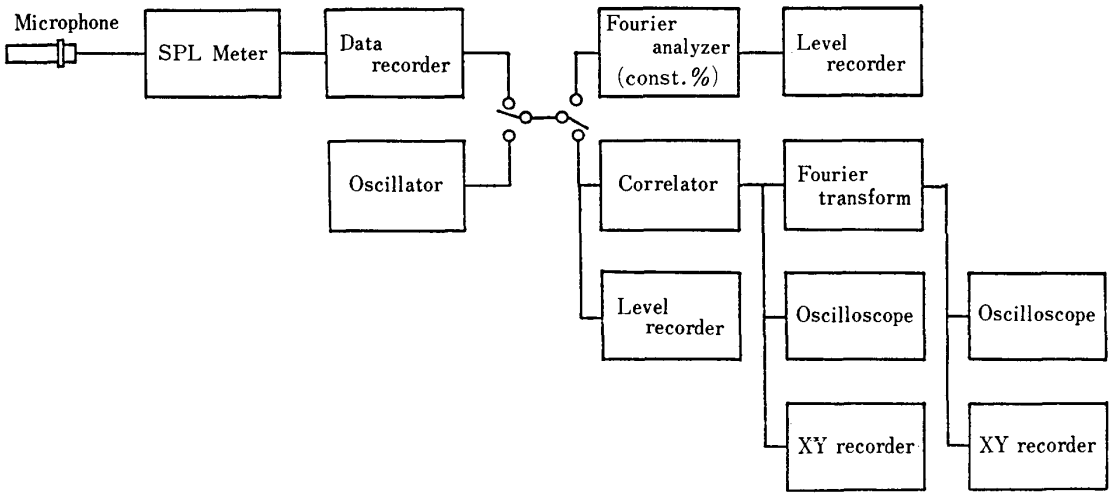


FIG. 2–6. Block diagram of instrumentation for acoustic measurement.

A block diagram of the instrumentation is shown in Fig. 2–6. The signal from the condenseer microphone was fed via an amplifier to a magnetic tape recorder and a level recorder. With a digital correlator, auto-correlation of sound prssure was calculated to give its power spectrum in frequency space (0 ~ 10 kHz).

2–2 *Sound pressure levels*

Sound pressure levels associated with separated flows around flat plates are shown in Fig. 2–7 for various conditions of flow velocity, attack angle and plate dimension. The level takes considerably large values at $\alpha=0°$ and after a minimum at $\alpha=30°$ ~ 60° increases with increasing attack angle. These features imply that the flow

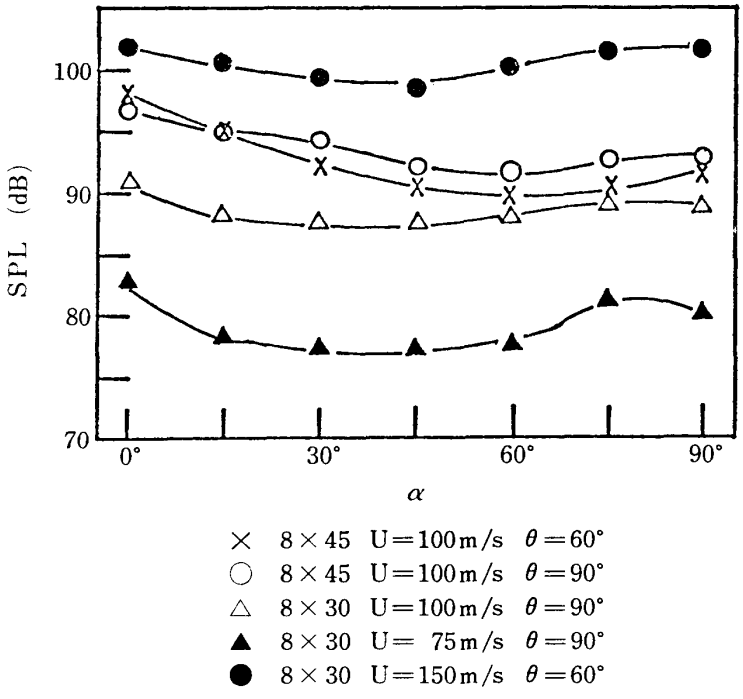


FIG. 2–7. Sound pressure level vs. attack angle; $r=2$ m.

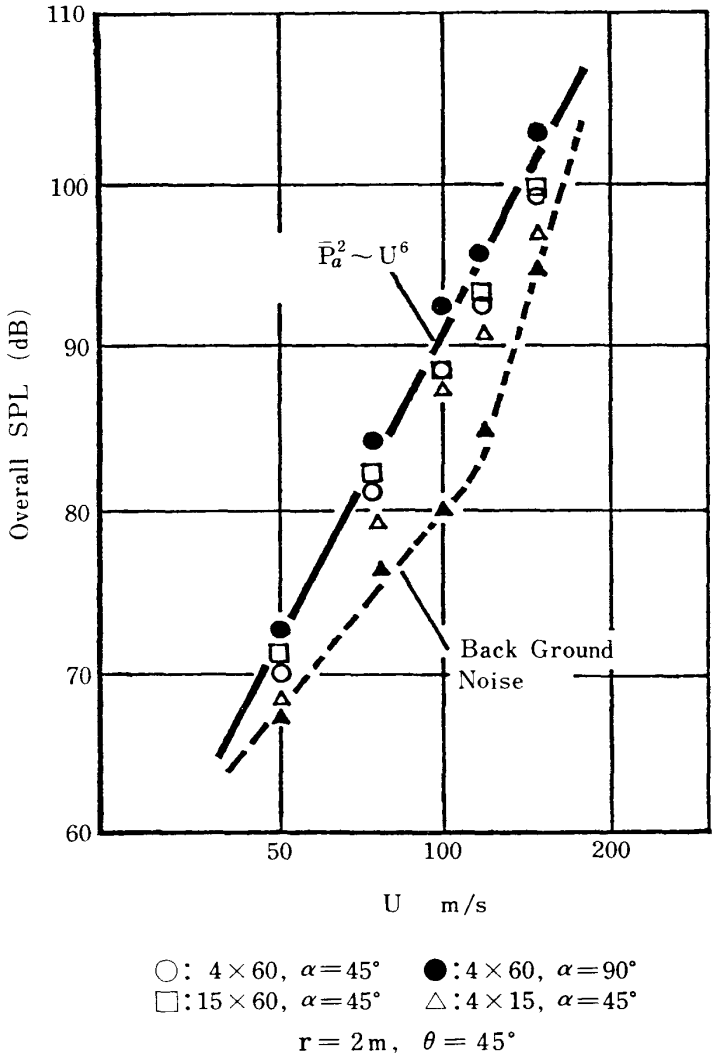


FIG. 2-8. Sound pressure level vs. flow velocity; $r$=2 m, $\theta$=45°.

structures should be different for $\alpha<30°$ and $\alpha>30°$. In the present study, since definitely separated flows of a flat plate are to be considered, cases of $\alpha>30°$ are investigated intensively.

As expected, the flow velocity has a marked effect on the sound pressure level as shown in Fig. 2-8. The sound pressure is proportional to the third power of the flow velocity. This suggests that the associated noise should be generated mainly due to fluctuating forces acting on the plate surface, being of accoustic dipole sources. The background noise level shown in the figure is the sound pressure level of the jet alone without the plate. There is not marked difference in the levels with respect to the azimuth. On this respect of directivity, it is to be mentioned in the next section. The chord of plate has an appreciable effect on the sound pressure level, the smaller chords being associated with the lower levels.

### 2-3 *Directivities*

The distributions of sound pressure level at different frequencies are shown in Fig. 2-9 where the band width is $\pm 3\%$ of the center frequency. From the figure, it is

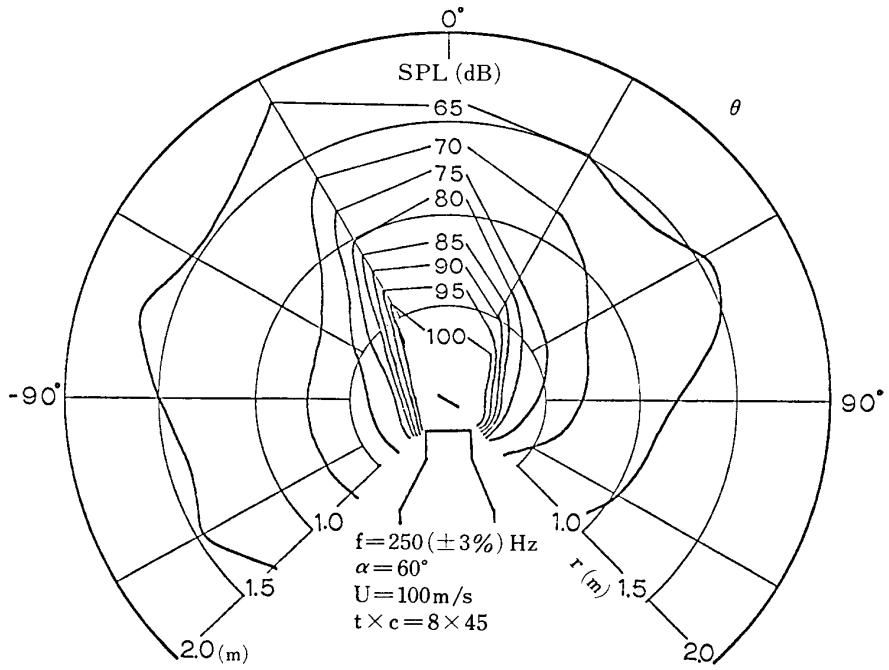


(a) $f$=250(±3%) Hz.

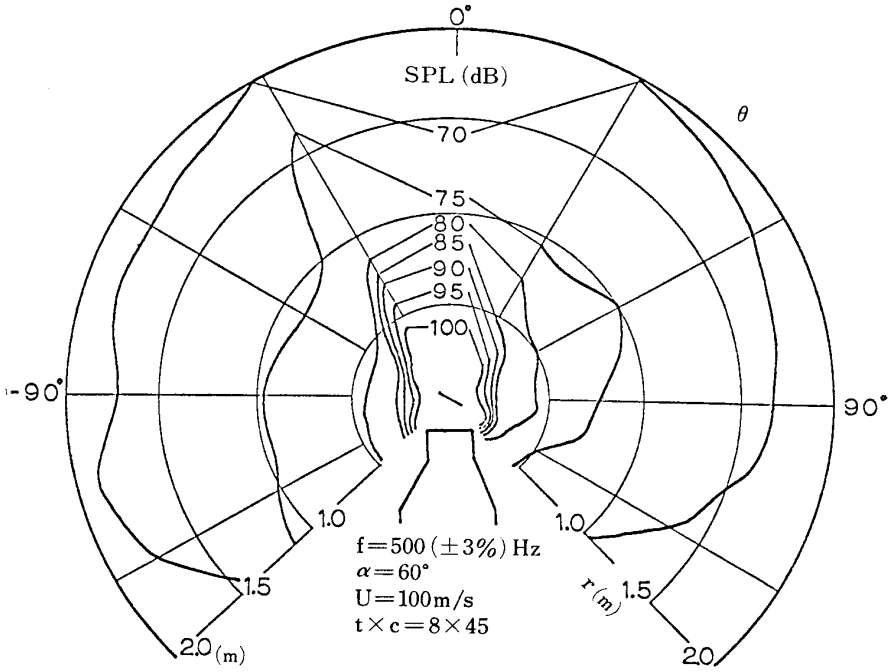


(b) $f$=500(±3%) Hz.

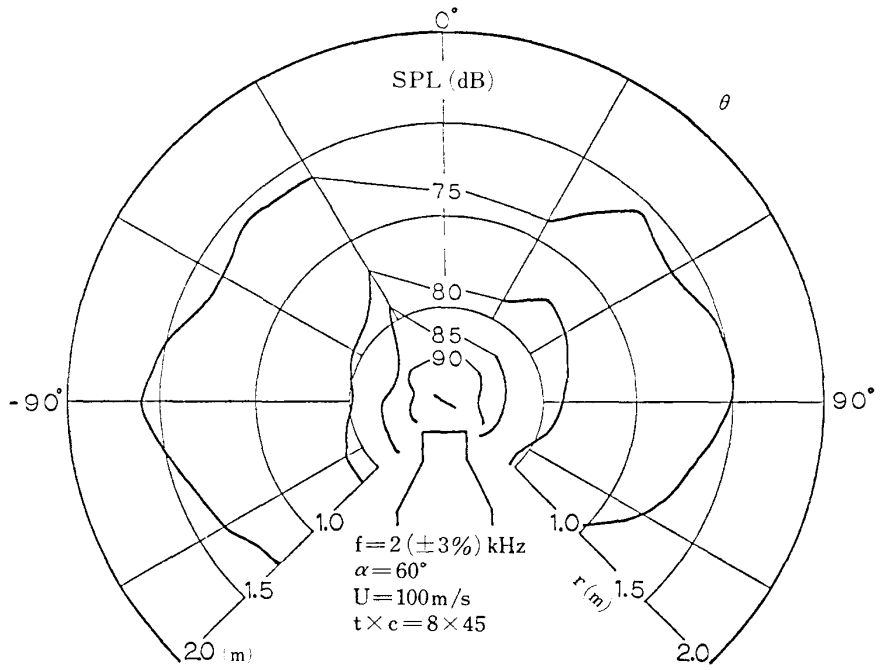


(c) $f=2(\pm 3\%)\,k$Hz.

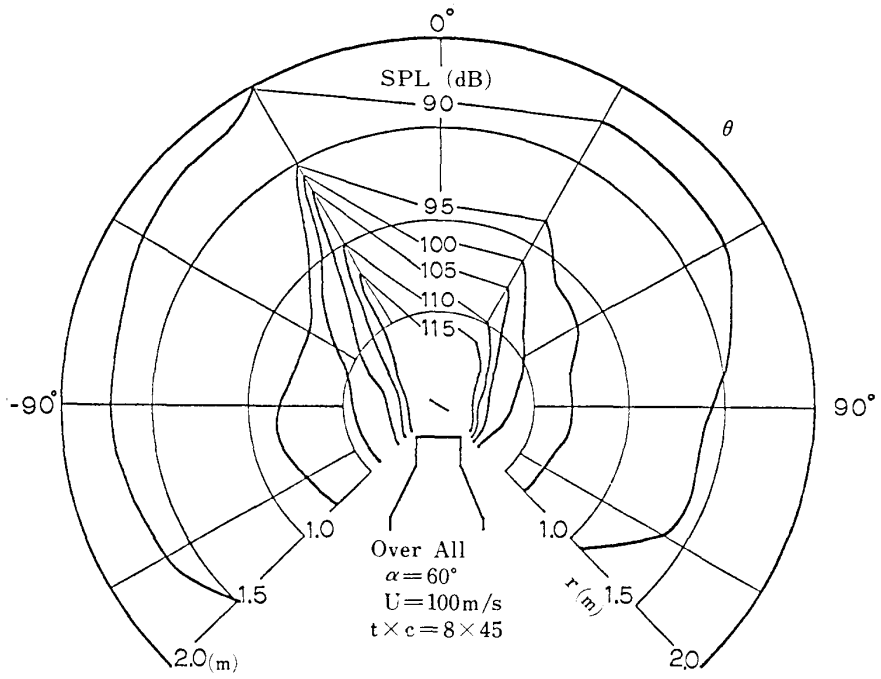


(d) Overall.

FIG. 2-9. Sound pressure level distribution; $t\times c=8\times 45$, $\alpha=60°$, $U=100$ m/s.

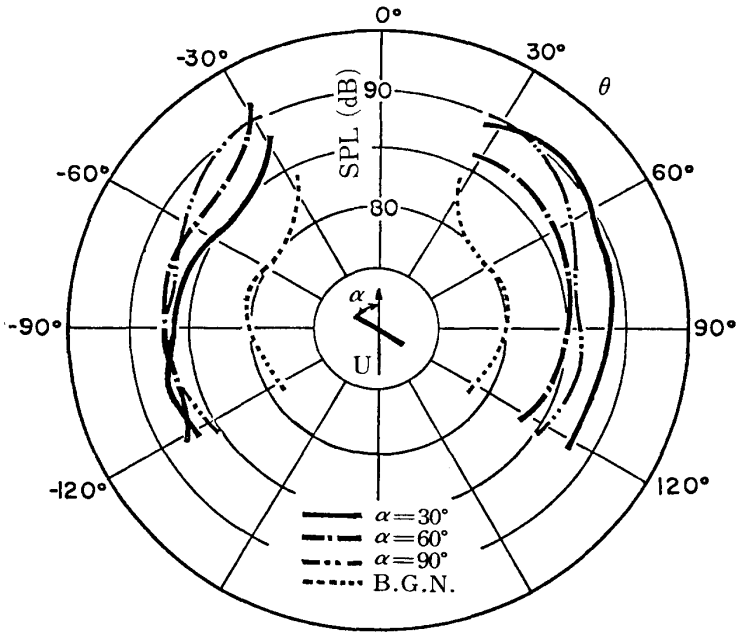


FIG. 2–10. Effect of attack angle on directivity; $t\times c=8\times 45$, $U=100$ m/s, $r=2$ m.

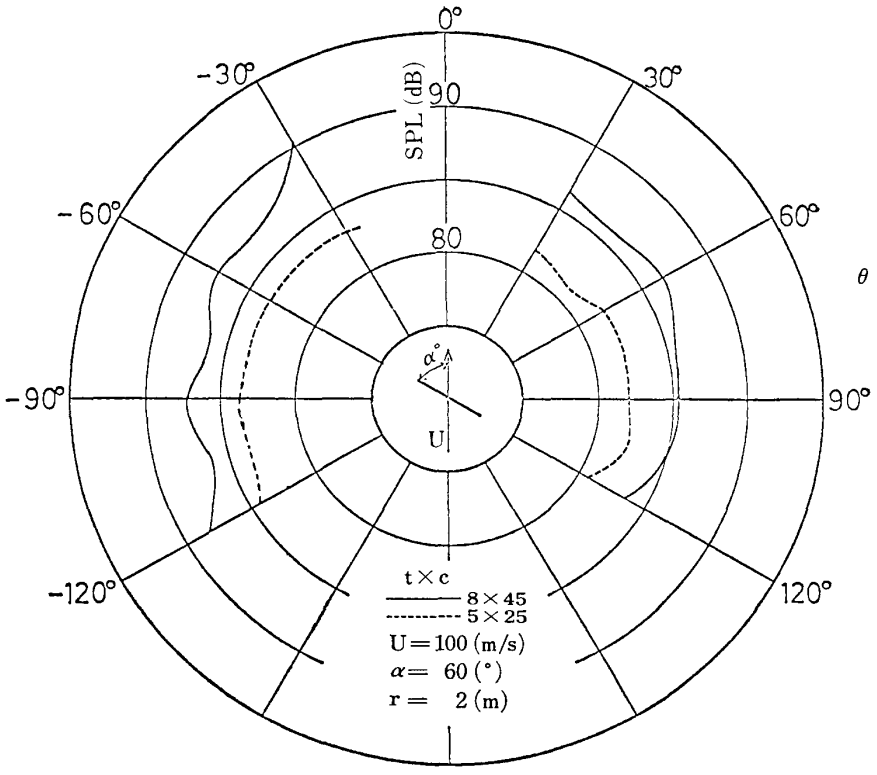


FIG. 2–11. Effect of chord on directivity; $\alpha=60°$, $U=100$ m/s.

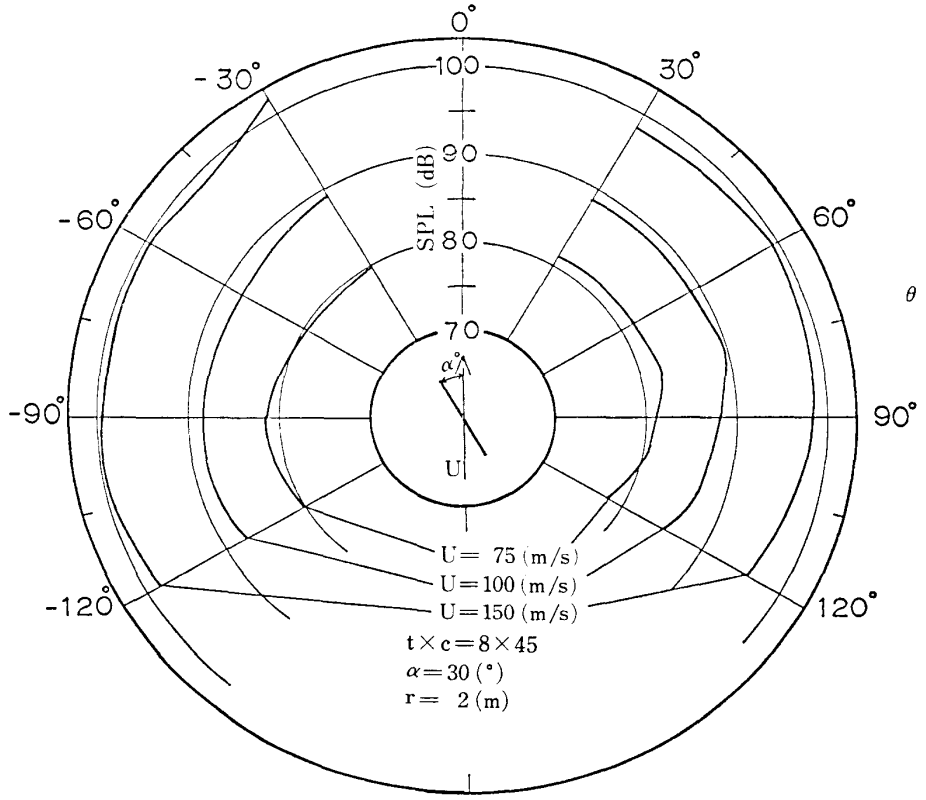


FIG. 2-12. Effect of flow velocity on directivity; $t\times c=8\times 45$, $\alpha=30°$, $r=2$ m.

seen that far-field radiation of the sound could be obtained at $r>0.7$ m for 250 Hz and 500 Hz frequencies and at $r>0.3$ m for 2 kHz frequency. The latter radiates appreciably toward $\theta=\pm 90°$. The directivity of the overall sound pressure is rather close to that of 500 Hz frequency (Fig. 2-9(d)). For the case of $\alpha=60°$, both sound pressure levels take a maximum at $\theta=30°$ and a minimum at $\theta=120°$. This also means the directivity of sound radiation from dipole sources.

Figure 2-10 shows the directivity of the associated noise for different attack angles. Although the directivity of dipole-source sound is not evidently shown, the level is 2~3 dB higher at the azimuth perpendicular to the plate surface ($\theta=60°$ for $\alpha=30°$, $\theta=30°$ for $\alpha=60°$, $\theta=0°$ for $\alpha=90°$) than at others, being of dipole-source radiation. In the figure, the directivity of the background noise is also shown to be different remarkably from those of the separated flow noise. For the plates of 5 mm×25 mm and 8 mm×45 mm, the directivities of the associated noise are shown in Fig. 2-11. There is little difference between them. As shown in Fig. 2-12, the flow velocity has little effect on the directivity, although it tends to shift the azimuth of the maximum level slightly downstream due to convective effect.

### 2-4 *Frequency spectra*

The associated sound pressure has a broad-band spectral density. The spectral density is affected by the plate size, attack angle and flow velocity, but it hardly differs with respect to the azimuth. Typical spectra at different attack angles are shown in Figs, 2-13 (a) to (c). At $\alpha=30°$(a), the spectral density takes a maximum at $f=500$

$\sim$800 Hz with decreasing at about 5 dB/kHz at higher frequencies. At $\alpha=60°$(b), it also takes a maximum at $f=500\sim800$ Hz but decreases at about 3 dB/kHz at higher frequencies. At $\alpha=90°$(c), the maximum occurs at $f=800\sim1200$ kHz and the decrease rate is about 3 dB/kHz. These features are observed same for all cases of the plate thickness ($t=2$, 5, 8 mm) except $t=15$ mm. It means that the separated flow noises, hence the separated flows itself, might be inherently different for the

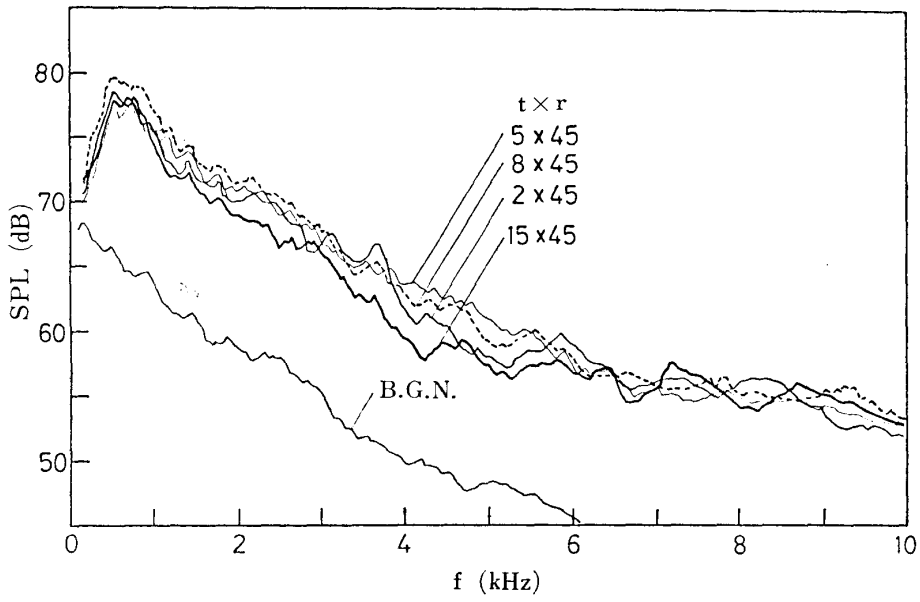


(a) $\alpha=30°$

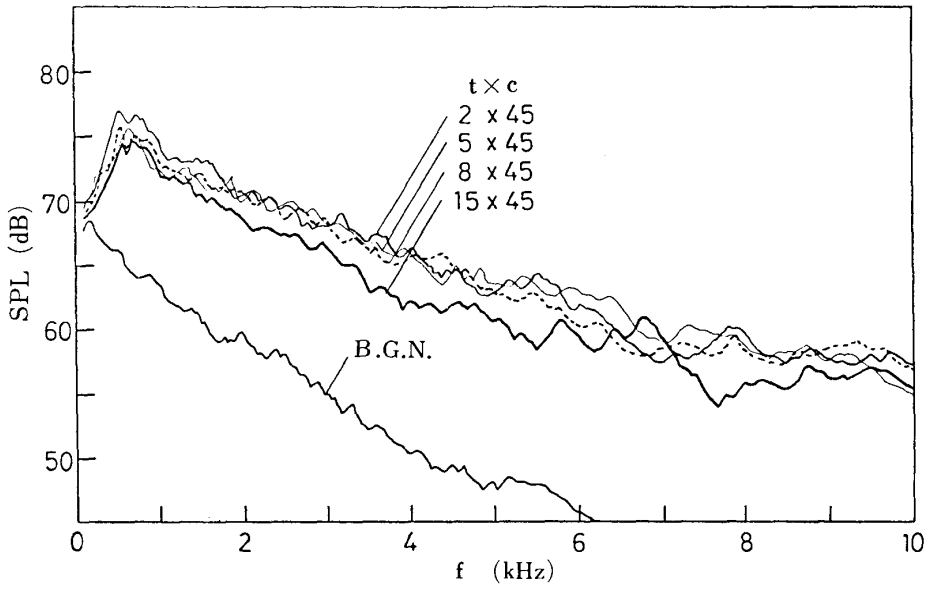


(b) $\alpha=60°$

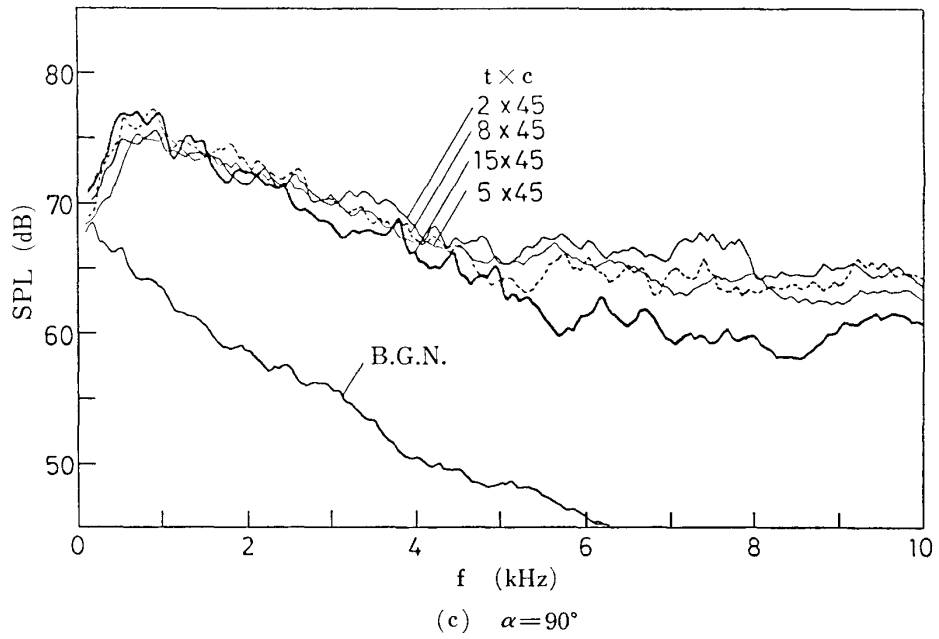


(c) $\alpha=90°$

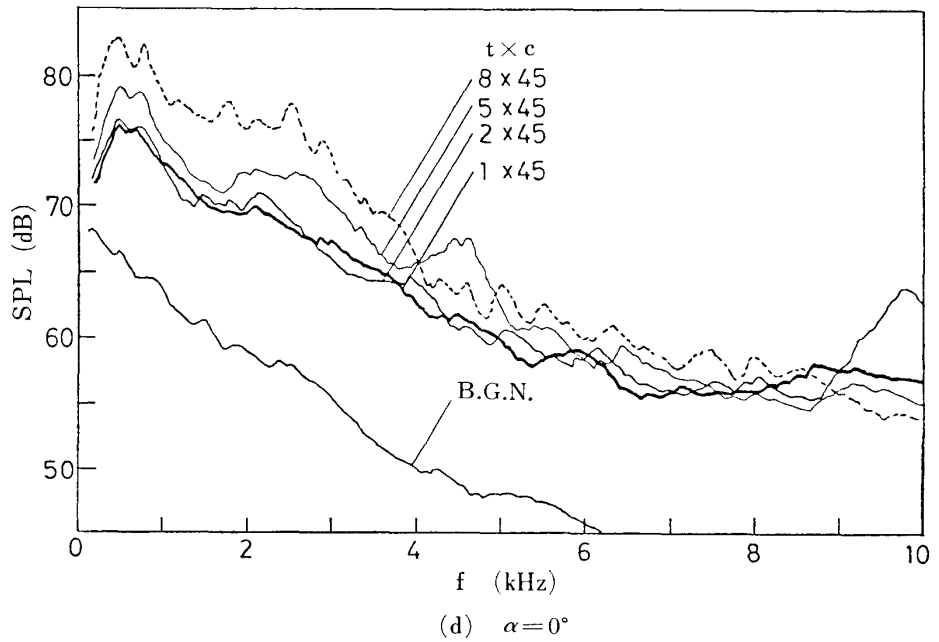


(d) $\alpha=0°$

FIG. 2-13. Frequency spectra; $U=100$ m/s, $r=2$ m, $\theta=60°$.

plates with thickness/chord ratio above and below 1/3. Although plates of 8 mm×45 mm and 5 mm×45 mm were employed almost throughout the present study, the conclusive results obtained would be valid for thinner plates.

In Fig. 2-13(d), the spectra for $\alpha=0°$ are shown. In this case, the plate thickness has a considerable effect on the spectral density. With $\alpha=0°$, the flow field would be expected much different from those with large attack angles. As for the associated

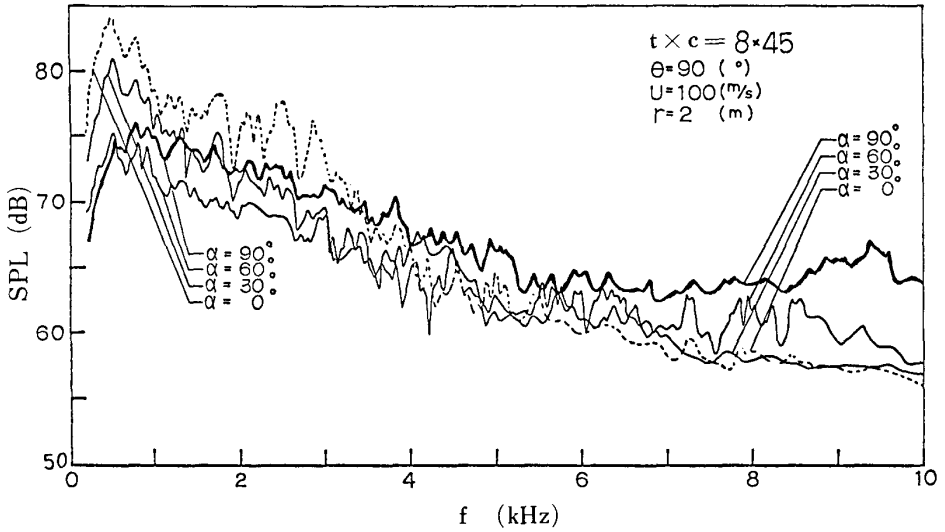


FIG. 2–14. Effect of attack angle on frequency spectra; $t\times c=8\times 45$, $U=100$ m/s, $\theta=90°$, $r=2$ m.

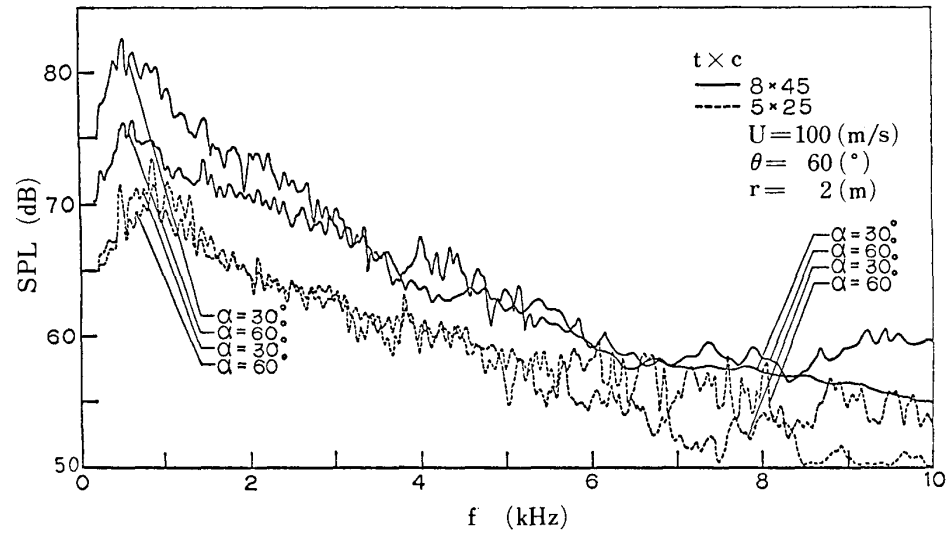


FIG. 2–15. Effect of chord on frequency spectra; $U=100$ m/s, $r=2$ m, $\theta=60°$.

noise, appreciable differences are to be observed. As mentioned before, in the present study, the well-defined separated flows were selected, and only flows with large attack angles were taken into account.

Comparison of spectra at different attack angles is shown in Fig. 2–14. With increasing attack angle from $\alpha=30°$ to $\alpha=90°$, the maximum level decreases and the higher frequency components increase their levels. The frequency of the maximum level hardly changes with the attack angle. The effect of the chord on the spectral density is represented in Fig. 2–15. Smaller chords result in lower levels and higher values of the peak frequency owing to smaller sizes of the separated flow. The oncoming flow velocity increases the peak frequency as well as the higher frequency levels as shown in Fig. 2–16.

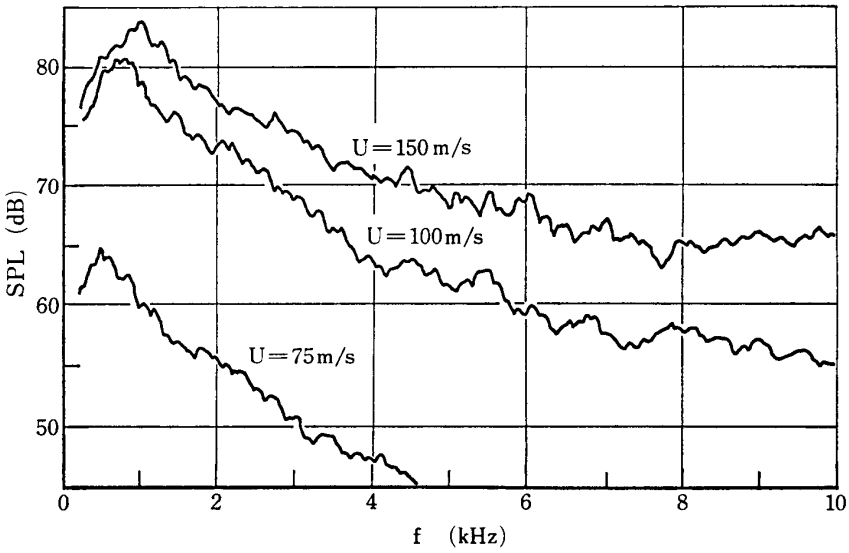


FIG. 2–16. Effect of flow velocity on frequency spectra; $t\times c=8\times 45$, $\alpha=30°$, $r=2$ m, $\theta=60°$.

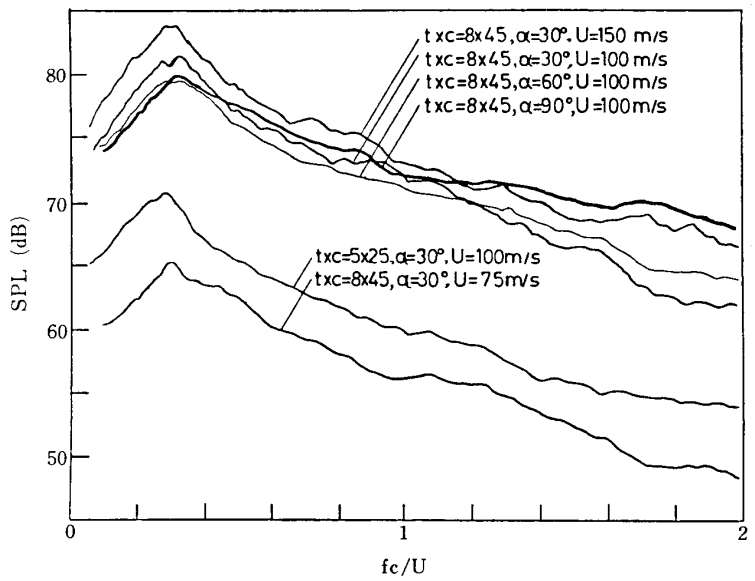


FIG. 2–17. Nodimensional frequency spectra.

In order to obtain a similarity for these spectral densities, correlation with a nondimensional frequency (Strouhal number) based on the oncoming flow velocity and the length of the chord projected onto the main flow direction was tried in vain. The alternative based on the flow velocity and the chord itself ($fc/U$), however, gives rather well-correlated spectra as shown in Fig. 2–17. The peak frequency then is about 0.3.

## 3. GENERATION MECHANISM

### 3–1 *Experimental method*

The far-field radiation of sound from a region of turbulent flow containing an

embedded body is given by [1]

$$p_a(r,t)=\frac{1}{4\pi r}\int_A\left[\frac{\partial}{\partial t}(\rho u_n)\right]ds+\frac{x_i}{4\pi ar^2}\int_A\left[\frac{\partial p_s}{\partial t}\right]ds+\frac{x_ix_j}{4\pi ar^3}\int_V\left[\frac{\partial^2 T_{ij}}{\partial t^2}\right]dv \quad (1)$$

where $p_a$ is the acoustic pressure, $\rho$ the density, $a$ the speed of sound, $r$ the distance from the acoustic source to the observation point (Appendix A). The square brackets [ ] denote evaluation at the retarded time $\tau=t-r/a$. The first two integrals imply noise generation by interaction between the fluid and the body surface $A$ which has a normal velocity $u_n$ and wall-surface pressure $p_s$. The third integral is the Lighthill integral for turbulence-generated quadrupole noise. $T_{ij}$ is the effective stress tensor $\rho u_iu_j+\tau_{ij}+(p-a^2\rho)\delta_{ij}$. When there is no source of fluid flow and the wall-surface is stationary or in rigid steady motion ($\partial u_n/\partial t=0$), the first integral vanishes and only the last two integrals dominate. The radiation then arises mainly from a quadrupole distribution generated with turbulent stress fluctuations and from a dipole layer associated with pressure fluctuations at the surface. Of these two type of acoustic source, which is more dominant is to be determined in this chapter by using a diagnostic technique of correlation between the acoustic far-field pressure and the wall-surface pressure, or the pressure in wake.

The experimental apparatus was the same one used in the preceding chapter except

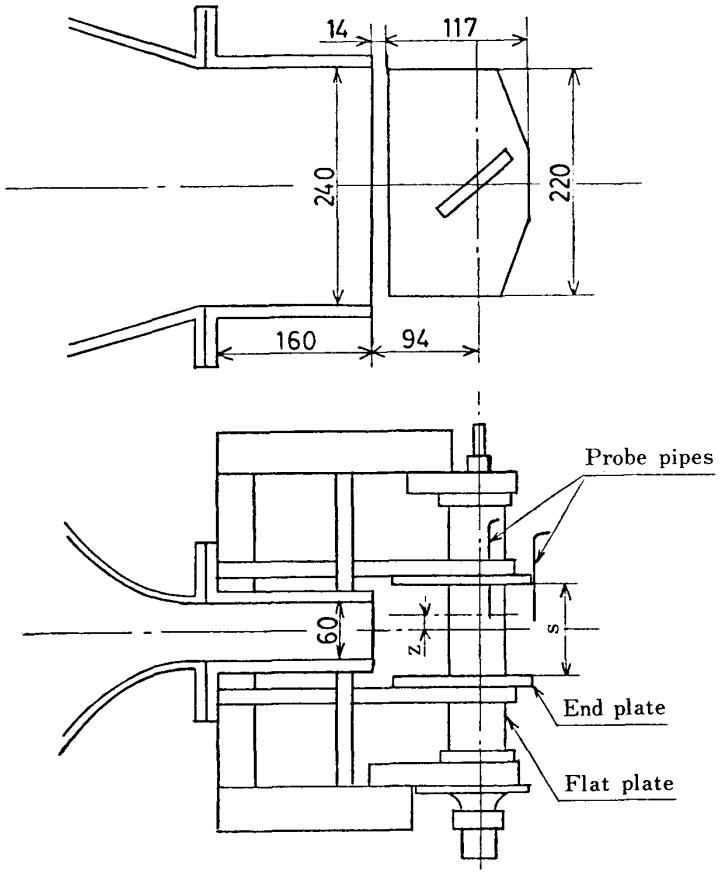


FIG. 3-1. Experimental apparatus for measurement of correlation between acoustic pressure and wall-surface pressure.

for the installation of end plates (Fig. 3–1). In order to examine the effect of the three-dimensional flow of a plate-in-jet system on the associated noise field, the location of the end plates was changed in the range within the jet width. The wall pressure on the plate surface was measured by the surface pinholes of 0.7 mm in diameter coupled to the diaphragm of the 1/2-inch microphone through a 3 mm ID stainless steel pipe embedded in the plate of 5 mm × 45 mm. The plate surface has seven pinholes. The configuration of the plate is illustrated in Fig. 3–2. Such a pressure transdeucer,

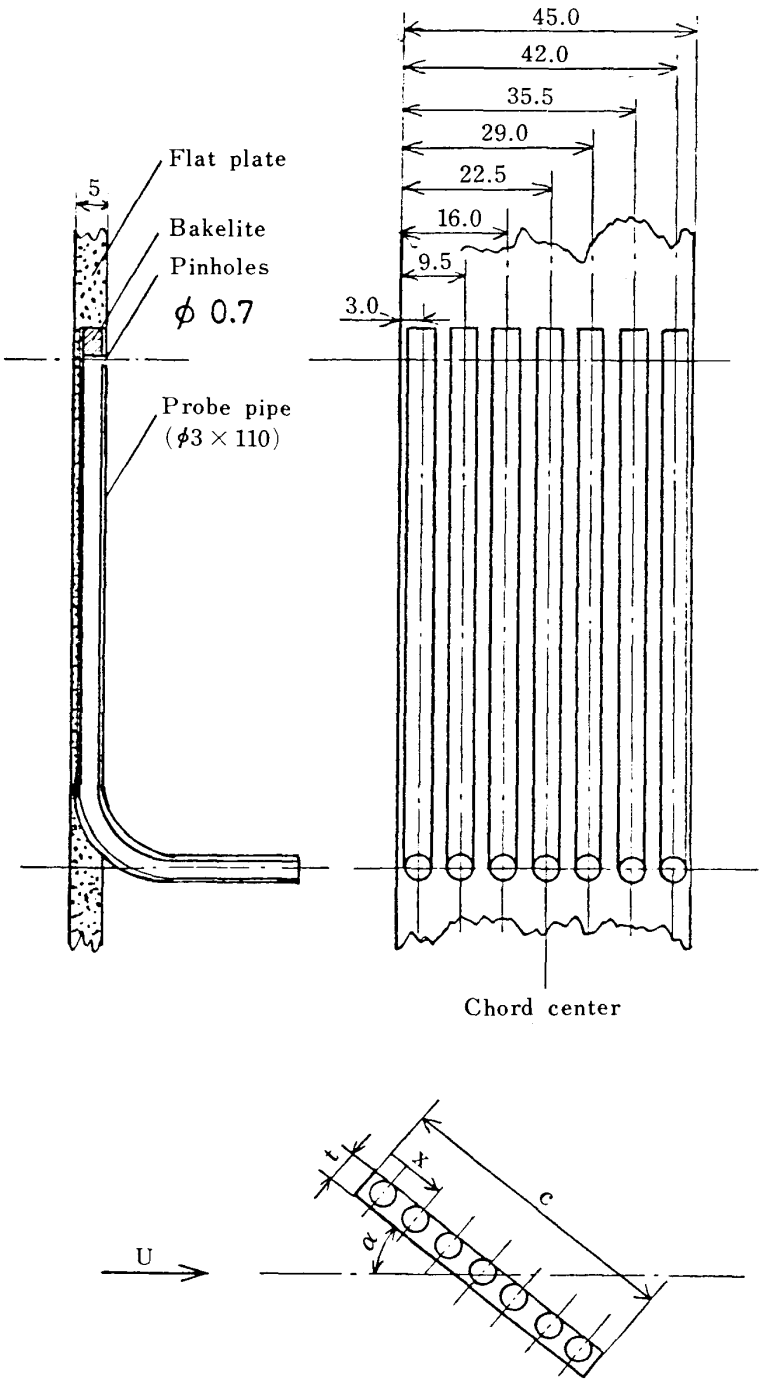


FIG. 3–2. Probe-microphone.

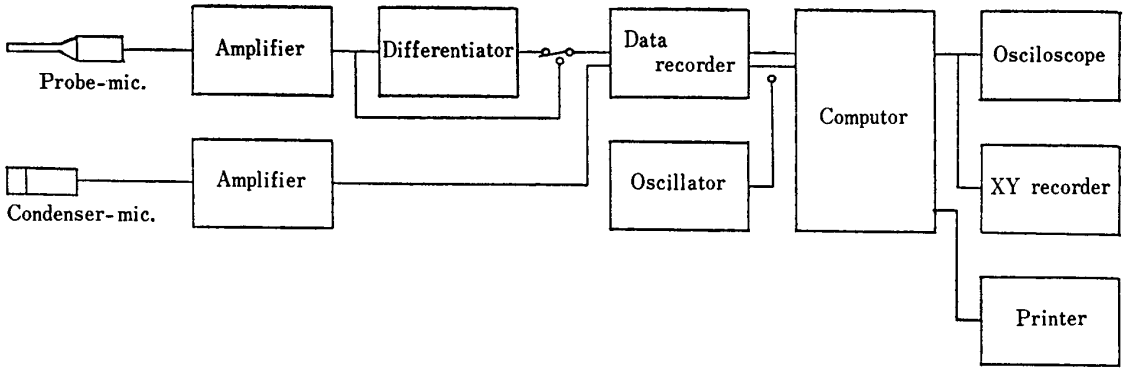


FIG. 3–3. Block diagram of instrumentation for acoustic and surface pressure correlation.

called a probe-microphone, has an inherent characteristics of frequency response to acoustic pressure. The output of the probe-microphone, $p_{sm}$, was fed to an analog differentiator to obtain the time derivative of the fluctuating wall pressure $\dot{p}_{sm}$. The used analog differentiator described in detail in Appendix B has a sufficient response for signals of 20 Hz to 6 kHz. The output should be corrected for the transfer impedance of the probe-microphone to obtain the time derivative of wall-surface pressure $\dot{p}_s$ by the means of a digital computor as mentioned in Appendix B. The correlation between the acoustic pressure $p_a$ and the time derivative wall-surface pressure $\dot{p}_s$ was obtained by a correlator. A block diagram of the overall instrumentation is shown in Fig. 3–3.

For the third volume-integral of Eq. (1), the second time-derivatives of the effective turbulent momentum stresses must be evaluated in the separated flow region. This is a quite difficult problem from the standpoints of measuring the stresses as well as of differential technique. The fluctuating pressure in a flow $p_f$ is largely attributed from the turbulent momentum stresses of the flow in its vicinity. The correlation

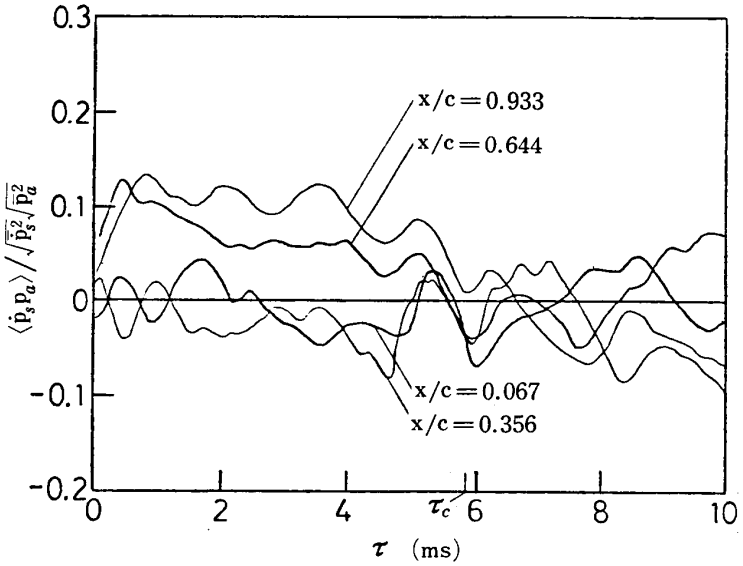


FIG. 3–4. Correlation between acoustic and surface pressures; $t \times c = 5 \times 45$, $s = 84$ mm, $\alpha = 60°$, $U = 100$ m/s, $r = 2$ m, $\theta = 45°$.

between $p_a$ and $p_f$ thus would give indirect inference of the contribution of turbulent momentum stresses to the noise field. By measuring the time derivative of the fluctuating pressure in flow by the probe-microphone, $\dot{p}_f$, the correlation between $p_a$ and $\dot{p}_f$ was evaluated to compare the contribution of the volume integral with that of the surface integral on the right hand of Eq. (1) (Appendix A).

3–2 *Correlation between acoustic and wall-surface pressures*

Figure 3–4 illustrates the correlation between the acoustic pressure and the wall-surface pressure $\langle p_s p_a \rangle / \sqrt{\overline{p_s^2}} \sqrt{\overline{p_a^2}}$. They show little correlation at the expected retarded time $\tau_c = 5.8$ ms (2 m/340 m/s). The same results were obtained for different

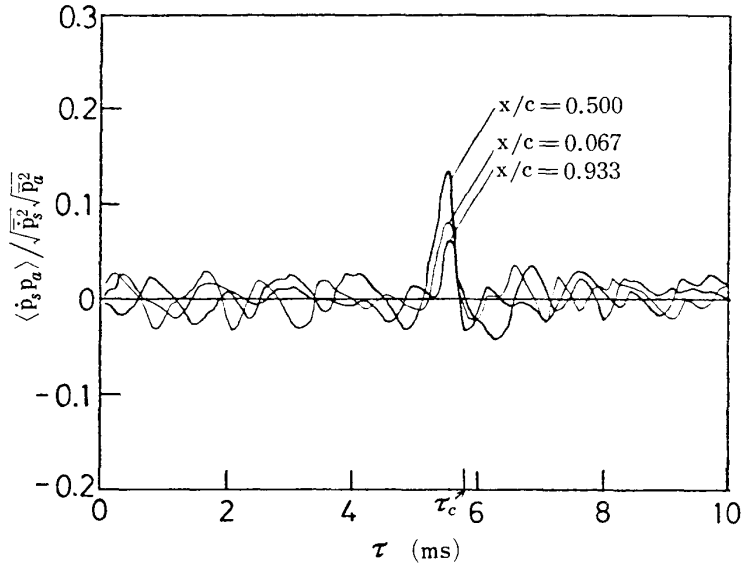


(a) r = 2m

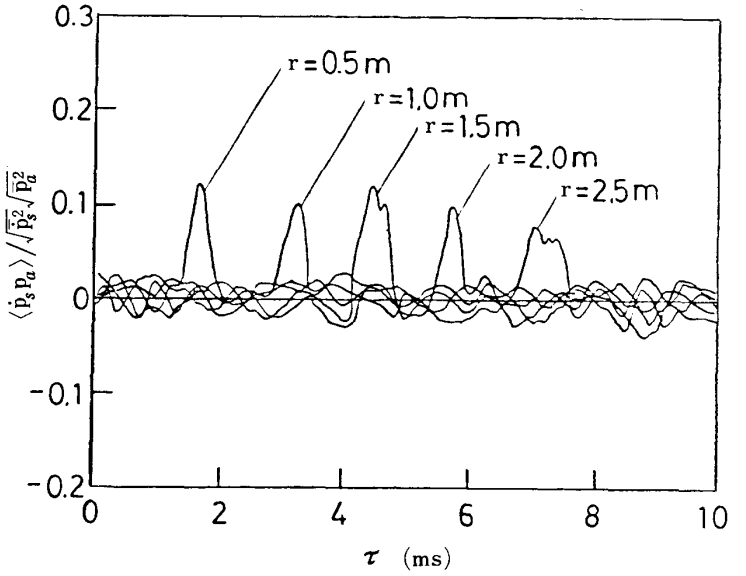


(b) x/c = 0.356

FIG. 3–5. Correlation between acoustic pressure and surface-pressure time-derivative; $t \times c = 5 \times 45$, $s = 84$ mm, $\alpha = 60°$, $U = 100$ m/s, $\theta = 45°$.

attack angles and mean flow velocities. In Fig. 3–5, the correlations between the acoustic pressure and the time derivative of the wall-surface pressure $\langle \dot{p}_s p_a \rangle / \sqrt{\overline{\dot{p}_s^2}} \sqrt{\overline{p_a^2}}$ are shown. Figure 3–5(a) shows an appreciable correlation at $\tau = 5.6$ ms. Although the normalized correlations are small in magnitude depending on the observation point of wall-surface pressure, it is seen evidently for the time derivative of wall-surface pressure to contribute considerably to the associated acoustic field. Figure 3–5 (b) shows the correlations at different diatances $r$. They take a maximum at $\tau = r/a$ $(\equiv \tau_c)$, that is, $|\langle \dot{p}_s p_a \rangle|_{\max} = \langle \dot{p}_s p_a \rangle_{\tau_c}$.

Mean-square fluctuating pressures $\overline{p_f^2}$ as shown in Fig. 3–6 take large values in magnitude at the boundary of the separated flow and relatively small values in its inner region. The correlations between the acoustic pressure and the fluctuating pressure in the flow $\langle p_f p_a \rangle / \sqrt{\overline{p_f^2}} \sqrt{\overline{p_a^2}}$ are shown in Fig. 3–7. Numbers in circle correspond to those in Fig. 3–6 denoting the position in the flow. At the points, ①, ④

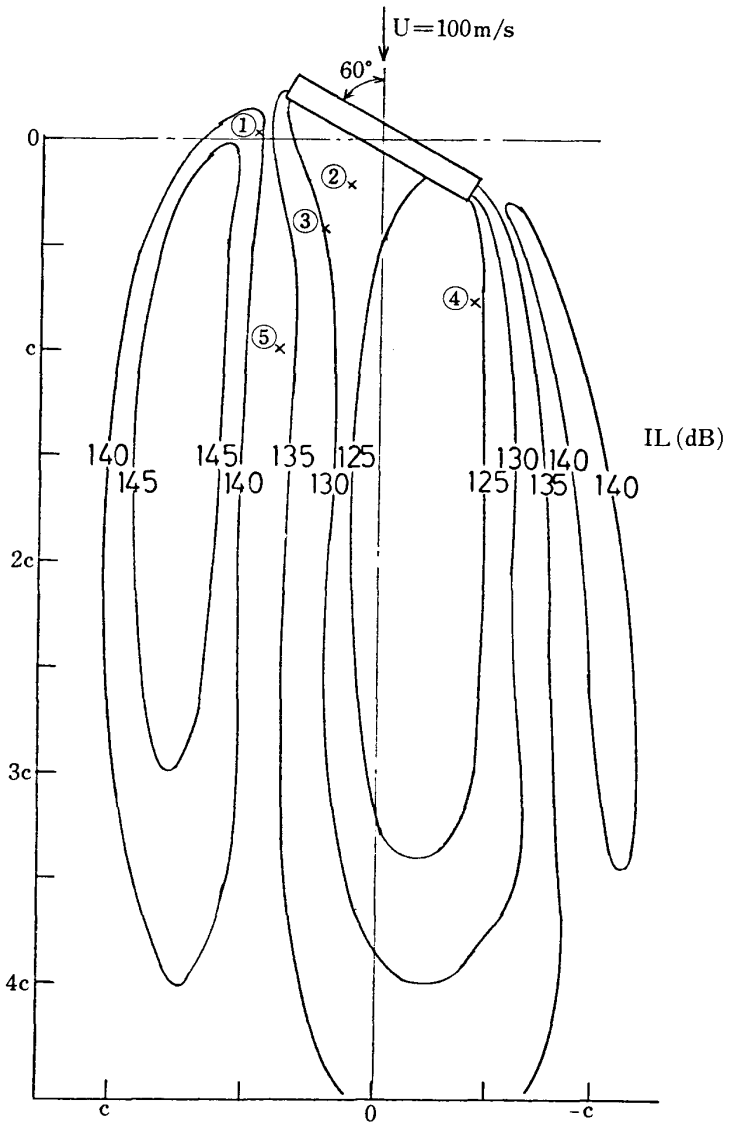


FIG. 3-6. Distribution of fluctuating pressure level; $t \times c = 5 \times 45$, $s = 84$ mm, $\alpha = 60°$, $U = 100$ m/s, $z = 0$.

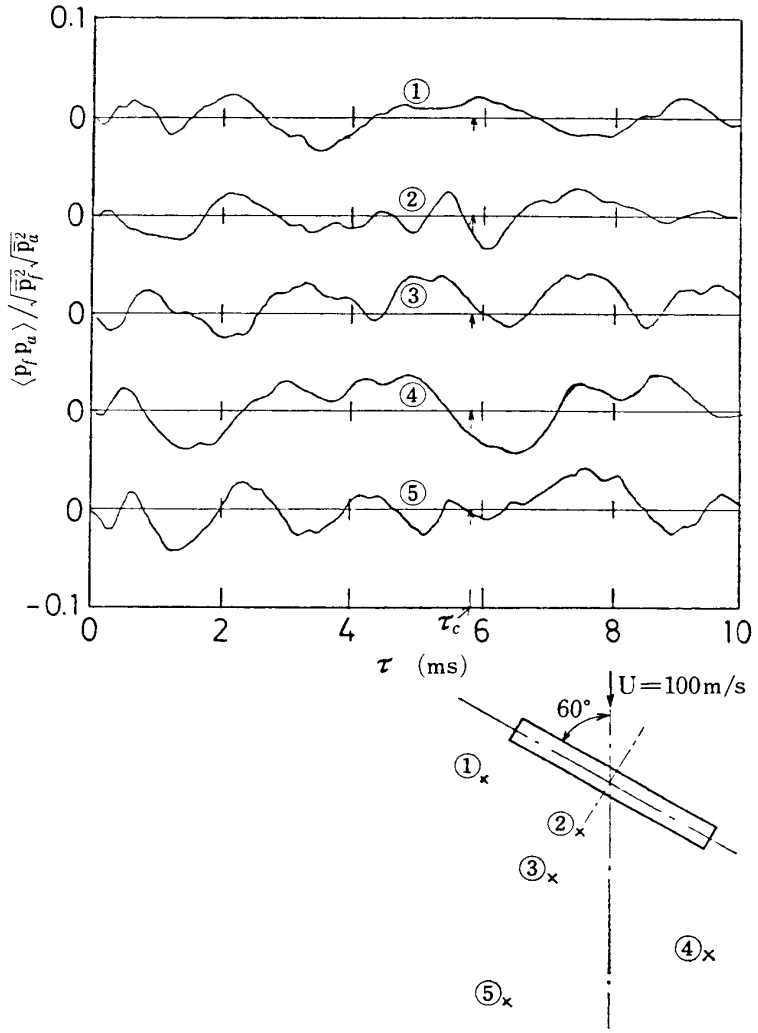


FIG. 3–7. Correlation between acoustic pressure and flow pressure; $t \times c = 5 \times 45$, $s = 84$ mm, $\alpha = 60°$, $U = 100$ m/s, $r = 2$ m, $\theta = 60°$.

and ⑤, where the fluctuating pressure takes large values, there is little correlation with the acoustic pressure. The time derivative of fluctuating pressure in flow $\dot{p}_f$ is likely to contribute to the associated acoustic field. The distribution of its mean-square $\overline{\dot{p}_f^2}$ is shown in Fig. 3–8 which is almost similar to the fluctuating pressure distribution in Fig. 3–6. Relatively strong intensities are found only close to the plate surface. The correlations between the acoustic pressure and the time derivative of the pressure in flow $\langle \dot{p}_f p_a \rangle / \sqrt{\overline{\dot{p}_f^2}} \sqrt{\overline{p_a^2}}$ is shown in Fig. 3–9. At the points of larger $\overline{\dot{p}_f^2}$, the correlation is smaller than that at the points of smaller $\overline{\dot{p}_f^2}$. The distribution of the maximum correlation is shown in Fig. 3–10. It is seen from the figure that at the points where the fluctuating pressure and its time derivative in flow have strong intensities there is little correlation with the far-field acoustic pressure. Only close to the plate surface, appreciable correlations are observed.

Further, it may be considered for the second time derivative of fluctuating pressure in flow $\ddot{p}_f$ to contribute to the acoustic far-field radiation (Appendix A). Because of the signal-to-noise ratio the measurement of $\ddot{p}_f$ is too difficult to correlate with the

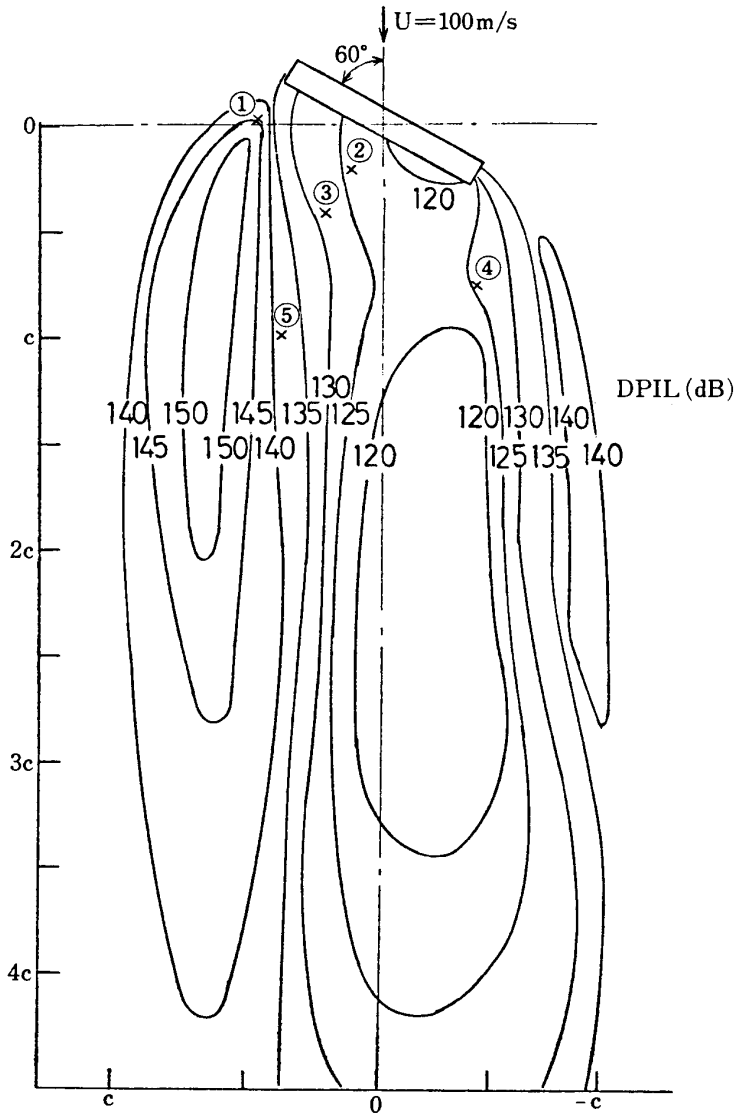


FIG. 3-8. Distribution of intencity level of flow-pressure time-derivative; $t\times c=5\times 45$, $s=84$ mm, $\alpha=60°$, $U=100$ m/s, $z=0$.

acoustic pressure. By using the relation

$$\langle \ddot{p}_f(t)p_a(t+\tau)\rangle = -\frac{\partial}{\partial\tau}\langle \dot{p}_f(t)p_a(t+\tau)\rangle$$

the correlation $\langle \ddot{p}_f p_a\rangle$ can be evaluated from the correlation $\langle \dot{p}_f p_a\rangle$. The result shows little correlation at the retarded time $\tau_c=r/a$.

In order to consider the relation of the fluctuating pressure in flow with that on the wall surface, their correlation $\langle p_f p_s\rangle$ and their time derivative correlation $\langle \dot{p}_f \dot{p}_s\rangle$ are obtained and shown in Fig. 3-11 and Fig. 3-12, respectively. They are strongly correlated with at the expected retarded time. It means that the fluctuating pressures close to the plate surface which are well-correlated with the acoustic pressure should be considerably attributed to the fluctuating wall-surface pressures through their propagation. This is also supported by the facts that these pressures have similar spectral

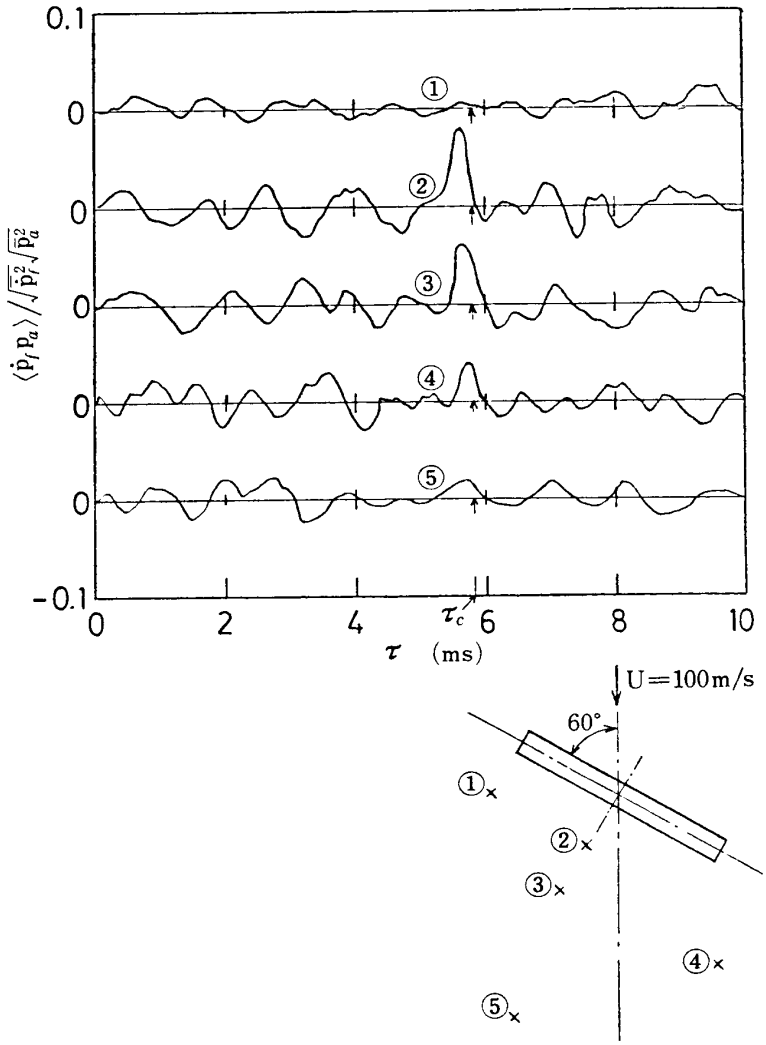


FIG. 3-9. Correlation between acoustic pressure and flow-pressure time-derivative; $t \times c = 5 \times 45$, $s = 84$ mm, $\alpha = 60°$, $U = 100$ m/s, $r = 2$ m, $\theta = 60°$.

densities and that the fluctuating pressures far from the plate have higher frequency components different from those of the acoustic pressure.

From these results obtained above, it can be said that the turbulence-generated quadrupole sources should have little contribution to the associated acoustic field and the dipole sources of fluctuating surface pressure dominate the field. Then Eq. (1) may be reduced to

$$p_a(r, \chi, t) = \frac{\cos \chi}{4\pi a r} \int_A [\dot{p}_s] ds \qquad (2)$$

where $\chi$ is the angle between the observation azimuth and the normal line to the plate surface, $\chi = 90° - (\alpha + \bar{\theta})$. The correlation $\langle \dot{p}_s p_a \rangle / \sqrt{\overline{\dot{p}_s^2}} \sqrt{\overline{p_a^2}}$ at different azimuths are shown in Fig. 3-13 for the case of $\alpha = 30°$. The peak correlation takes positive and negative values depending on the azimuth as shown in Fig. 3-14. For $\alpha = 30°$, it takes a maximum at $\theta = 60°$, zero at $\theta = -30°$ and a minimum at $\theta = -120°$. For

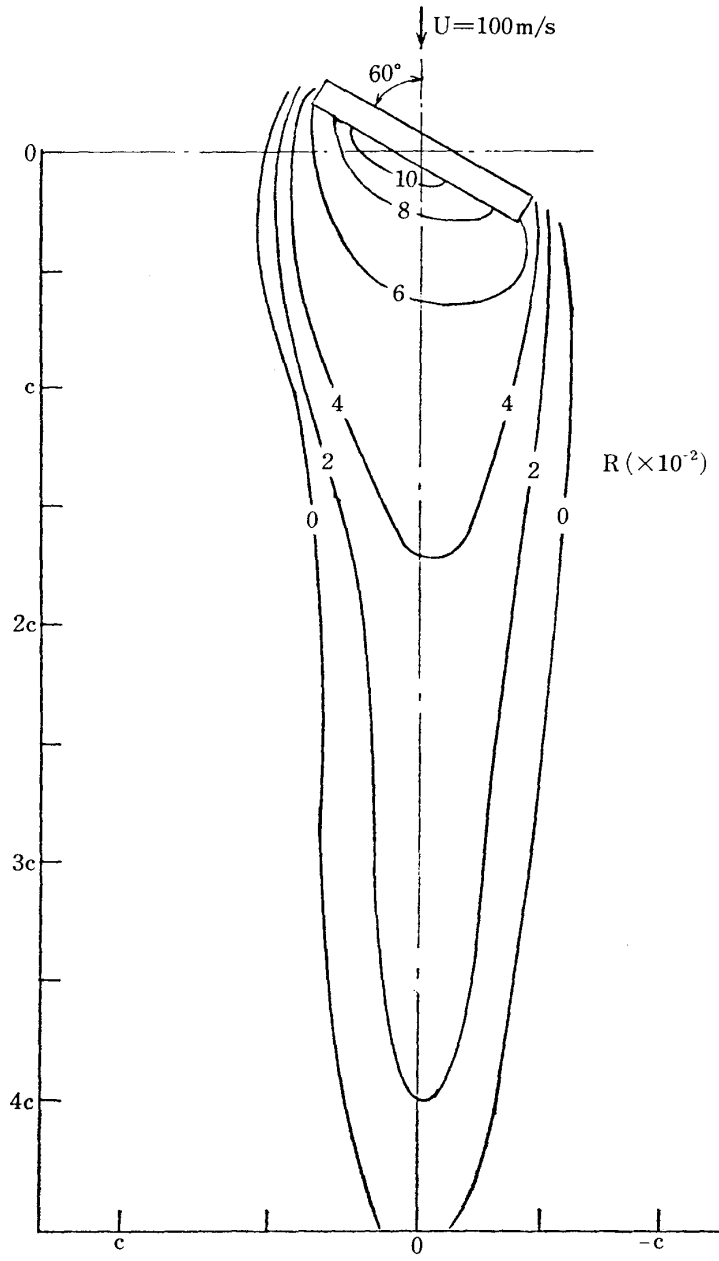


Fig. 3-10. Distribution of peak correlation between acoustic pressure and flow-pressure time-derivative; $t\times c=5\times 45$, $s=84$ mm, $\alpha=60°$, $U=100$ m/s, $z=0$, $r=2$ m, $\theta=60°$.

$\alpha=60°$, a maximum at $\theta=30°$ and zero at $\theta=120°$ and $-60°$. These features hold the relation deduced from Eq. (2)

$$\langle \dot{p}_s p_a \rangle_{\tau_c} = \frac{\cos\chi}{4\pi a r} \int_A \langle \dot{p}_s [\dot{p}_s] \rangle ds$$

that is, $\langle \dot{p}_s p_a \rangle_{\tau_c}$ is proportional to $\cos\chi$. This also verifies the above conclusion of dominant contribution of fluctuating surface pressure to the noise generation.

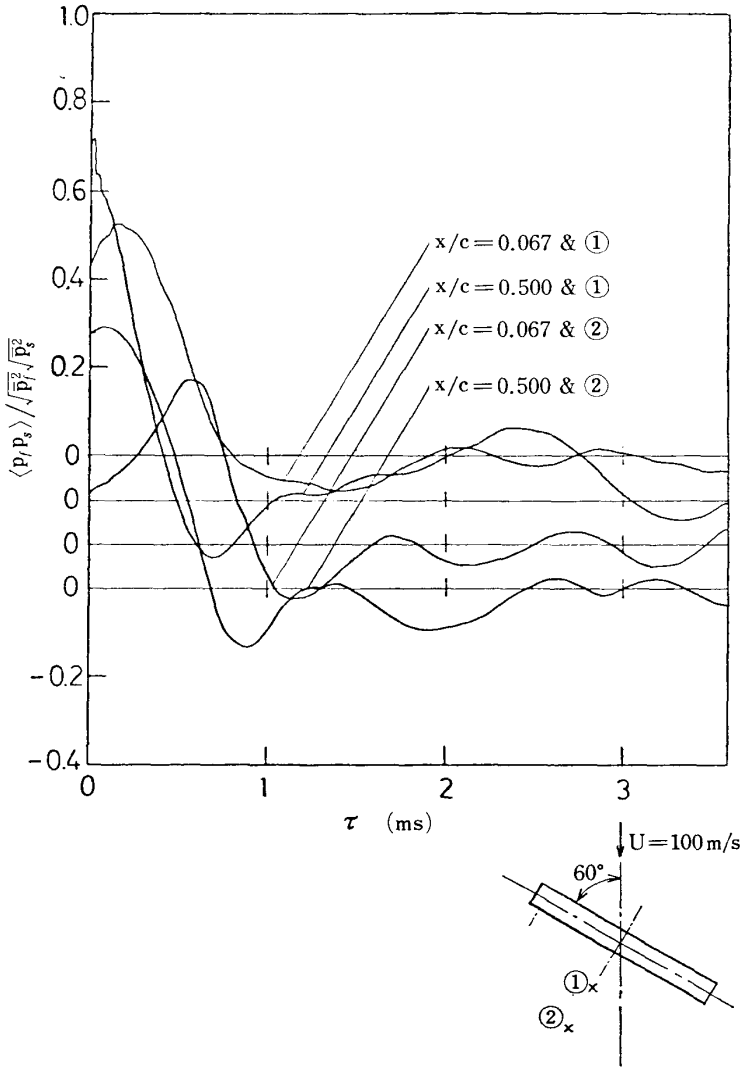


FIG. 3-11. Correlation between surface-pressure and flow-pressure; $t\times c=5\times 45$, $s=84$ mm, $\alpha=60°$, $U=100$ m/s, $z=0$.

3–3 *Effective noise source*

Multiplying the acoustic pressure to Eq. (2) yields

$$p_a(t)p_a(t')=\frac{\cos\chi}{4\pi ar}\int_A[\dot{p}_s(t)]p_a(t')ds.$$

Taking a time average leads to

$$\overline{p_a^2}=\langle p_a(t)p_a(t+\tau)\rangle_{\tau=0}=\frac{\cos\chi}{4\pi ar}\int_A\langle\dot{p}_s(t)p_a(t+\tau)\rangle_{\tau=\tau_c}ds. \qquad (3)$$

The auto correlation of the acoustic pressure, hence the acoustic intensity, is related to a surface integral of the cross correlation between the acoustic pressure and the wall-surface pressure time-derivative. Further, from Eq. (3), the effective acoustic source strength on the surface is

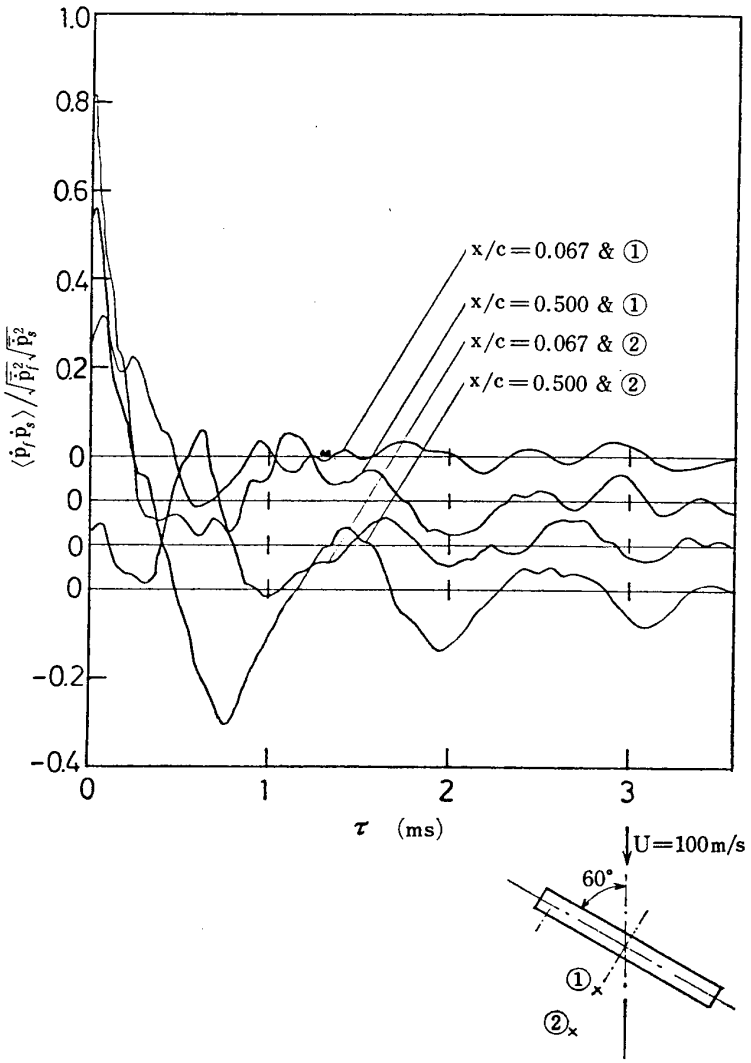


FIG. 3–12. Correlation between surface-pressure time-derivative and flow-pressure time-derivative $t\times c=5\times 45$, $s=84$ mm, $U=100$ m/s, $z=0$.

$$\frac{\partial \overline{p_a^2}}{\partial s}=\frac{\cos\chi}{4\pi a r}\langle \dot{p}_s p_a\rangle_{\tau_c}$$

that is, the strength is proportional to the cross correlation $\langle \dot{p}_s p_a\rangle_{\tau_c}$ [5].

The retarded cross correlation on the separated surface of the plate that is, the peak correlation, is shown in Fig. 3–15 for the case of $U=100$ m/s and $\alpha=30°$, 60°. Since $\overline{\dot{p}_s^2}$ is approximately constant throughout the surface as seen in the next chapter, the normalized correlation $R$ indicates the strength distribution of the effective acoustic source on the surface. It is seen from the figure that the source is strong at the center of the surface and relatively weak at both leading and training edges. These features resembles the Siddon's result [5] of a circular plate that the acoustic sources are concentrated substantially under the separation bubble and along the plate boundary the source strength is to be extremely weak. It should be noted that close to the end plates the source strength is considerably weak. As far as the acoustic radiation, the

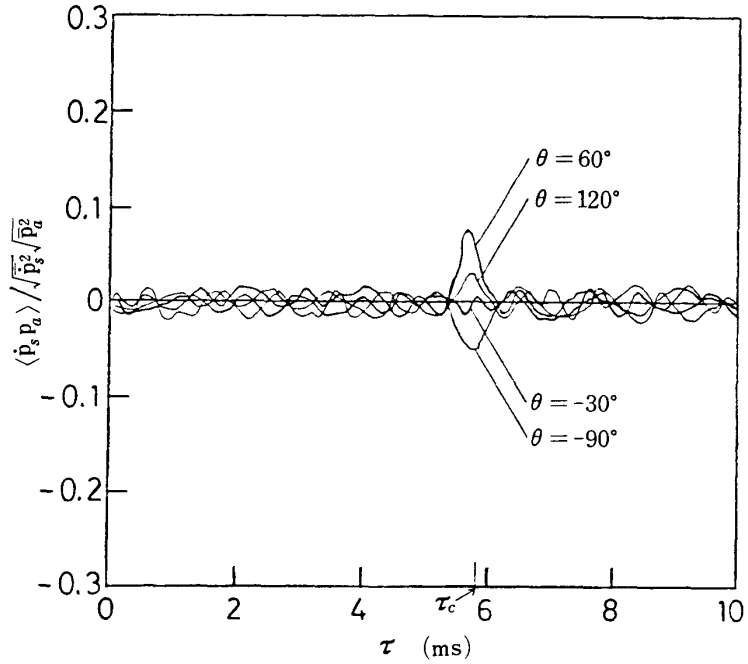


FIG. 3–13. Correlation between acoustic pressure and surface-pressure time-derivative at different azimuths; $t \times c = 5 \times 45$, $s = 84$ mm, $\alpha = 30°$, $U = 100$ m/s, $x/c = 0.356$, $r = 2$ m.

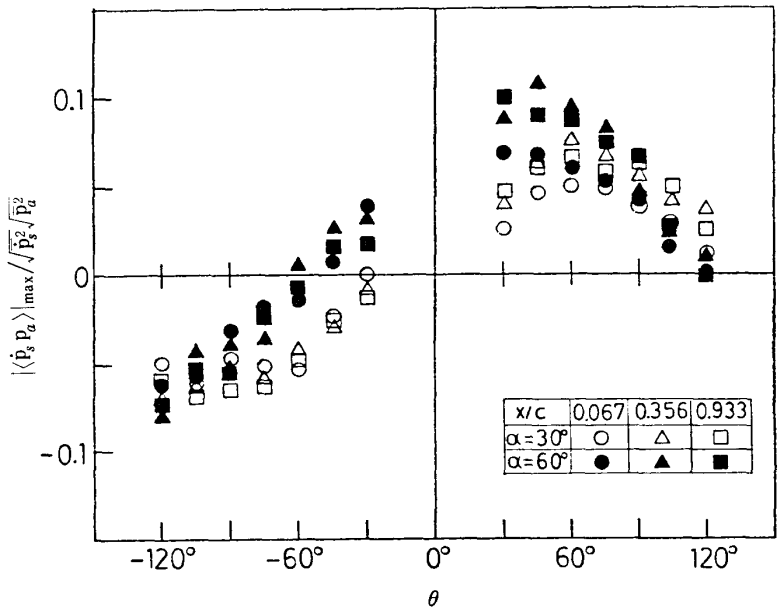


FIG. 3–14. Effect of azimuth on peak correlation between acoustic pressure and surface-pressure time-derivative; $t \times c = 5 \times 45$, $s = 84$ mm, $U = 100$ m/s, $r = 2$ m.

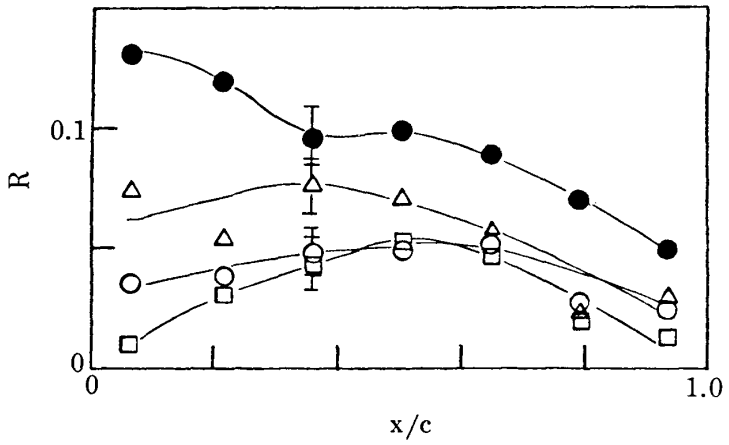


(a) $\alpha=30°$ $(\theta=90°)$

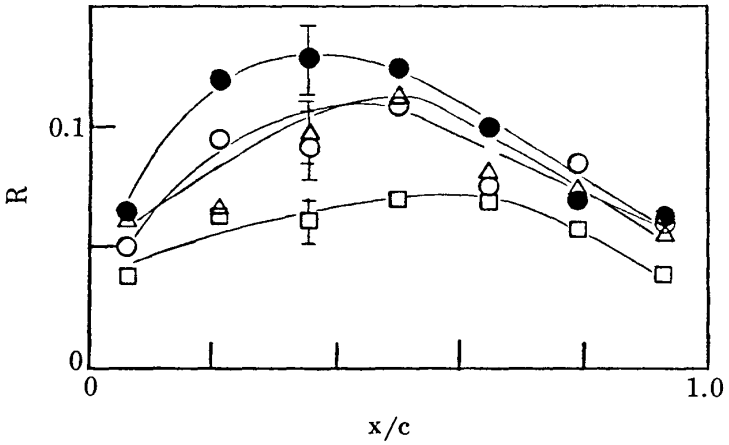


(b) $\alpha=60°$ $(\theta=60°)$

○ : s=72, z=0 ; △ : s=72, z=30
□ : s=72, z=35 ; ● : s=∞, z=0

FIG. 3–15. Chordwise distribution of peak correlation between acoustic pressure and surface-pressure time-derivative; $t\times c=5\times 45$, $U=100$ m/s, $r=2$ m.

source is likely to be distributed two-dimensionally. The three-dimensional flow close to the end plate has little effect on the acoustic pressure generation.

## 4. NOISE-SOURCE CHARACTERISTICS

### 4–1 *Experimental method*

In the preceding chapters, it is concluded that the dipole layer of fluctuating pressures on the plate surface should be the dominant source of the associated acoustic radiation. In this chapter, by measuring the time-derivative of fluctuating wall-surface pressure, the characteristics of noise source is to be investigated, and then the associated acoustic field is to be predicted with them.

The experimental apparatus employed is shown in Fig. 4–1. For the convenience

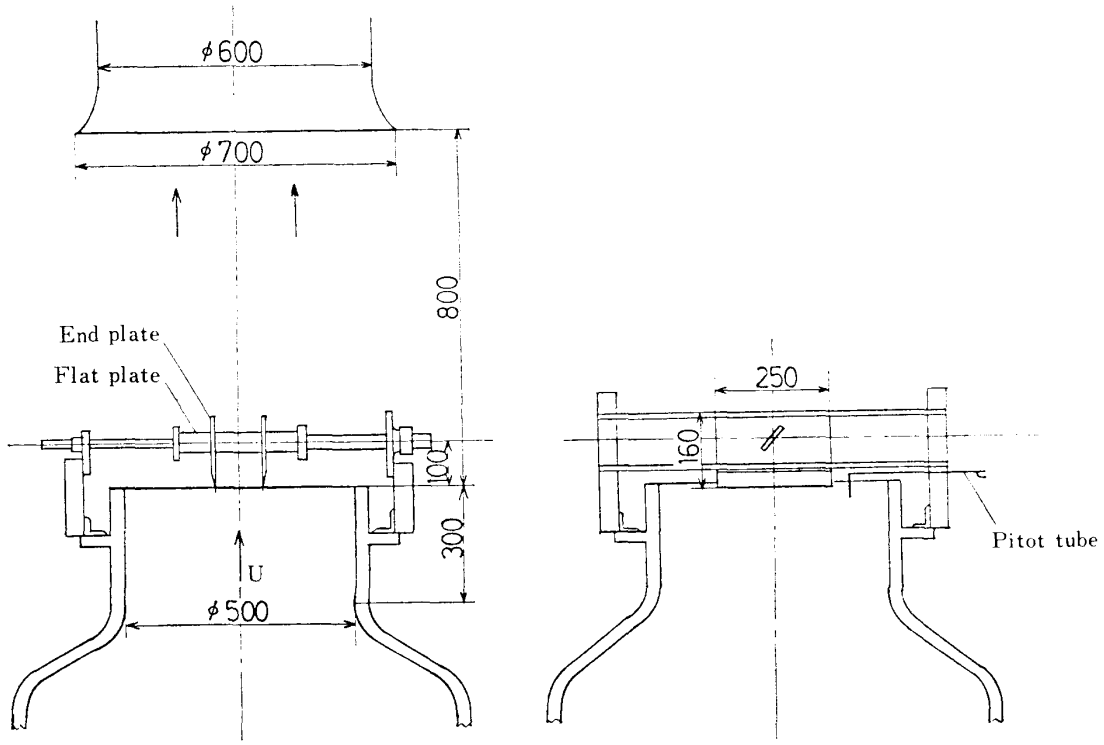


FIG. 4–1. Experimental apparatus for measurement of correlation between surface pressures.

of measurement, a wind tunnel with larger test section (500 mm in diameter) and lower wind speeds (0～45 m/s) than that used in the preceding chapters was employed. The plate with end plates was located at 100 mm from the outlet in a uniform oncoming flow of which the turbulent velocity was within about 1.5% of the mean velocity. The fluctuating wall-surface pressure was measured by a probe-microphone immersed in the plate to obtain its chordwise and spanwise intensity, cross correlation and spectral density.

From Eq. (2),

$$p_a(\boldsymbol{x}, t)p_a(\boldsymbol{x}, t+\tau)=\left(\frac{\cos\chi}{4\pi ar}\right)^2\int_{A_1}\int_{A_2}[\dot{p}_s(\boldsymbol{x}_1, t)][\dot{p}_s(\boldsymbol{x}_2, t+\tau)]ds_1ds_2 \qquad (5)$$

where $\boldsymbol{x}=(r, \chi)$, $\boldsymbol{x}_1=(x_1, z_1)$, $\boldsymbol{x}_2=(x_1, z_1)$, $ds_1=dx_1dz_1$, $ds_2=dx_1dz_1$ where the subscripts 1 and 2 denote different points on the surface. Taking a time average gives

$$\overline{p_a(\boldsymbol{x})^2}\equiv\langle p_a(\boldsymbol{x}, t)p_a(\boldsymbol{x}, t+\tau)\rangle_{\tau=0}=\left(\frac{\cos\chi}{4\pi ar}\right)^2\int_{A_1}\int_{A_2}\langle[\dot{p}_s(\boldsymbol{x}_1, t)][\dot{p}_s(\boldsymbol{x}_2, t+\tau)]\rangle_{\tau=0}ds_1ds_2. \qquad (6)$$

The inner integral on the right hand can be expressed in terms of correlation area $A_c$ for the time derivative of surface pressure,

$$\int_{A_2}\langle[\dot{p}_s(\boldsymbol{x}_1, t)][\dot{p}_s(\boldsymbol{x}_2, t+\tau)]\rangle ds_2=A_c(\boldsymbol{x}_1)\cdot\overline{\dot{p}_s(\boldsymbol{x}_1)^2} \qquad (7)$$

where the retarded time difference is accounted for in the correlation area by taking the maximum values of the cross-correlation. Thus, the mean-square acoustic pressure is expressed as

$$\overline{p_a(\boldsymbol{x})^2}=\left(\frac{\cos\chi}{4\pi ar}\right)^2\int_A A_c(x,z)\overline{\dot{p}_s(x,z)^2}dxdz=\left(\frac{\cos\chi}{4\pi ar}\right)^2\int_A Q(x,z)dxdz \quad (8)$$

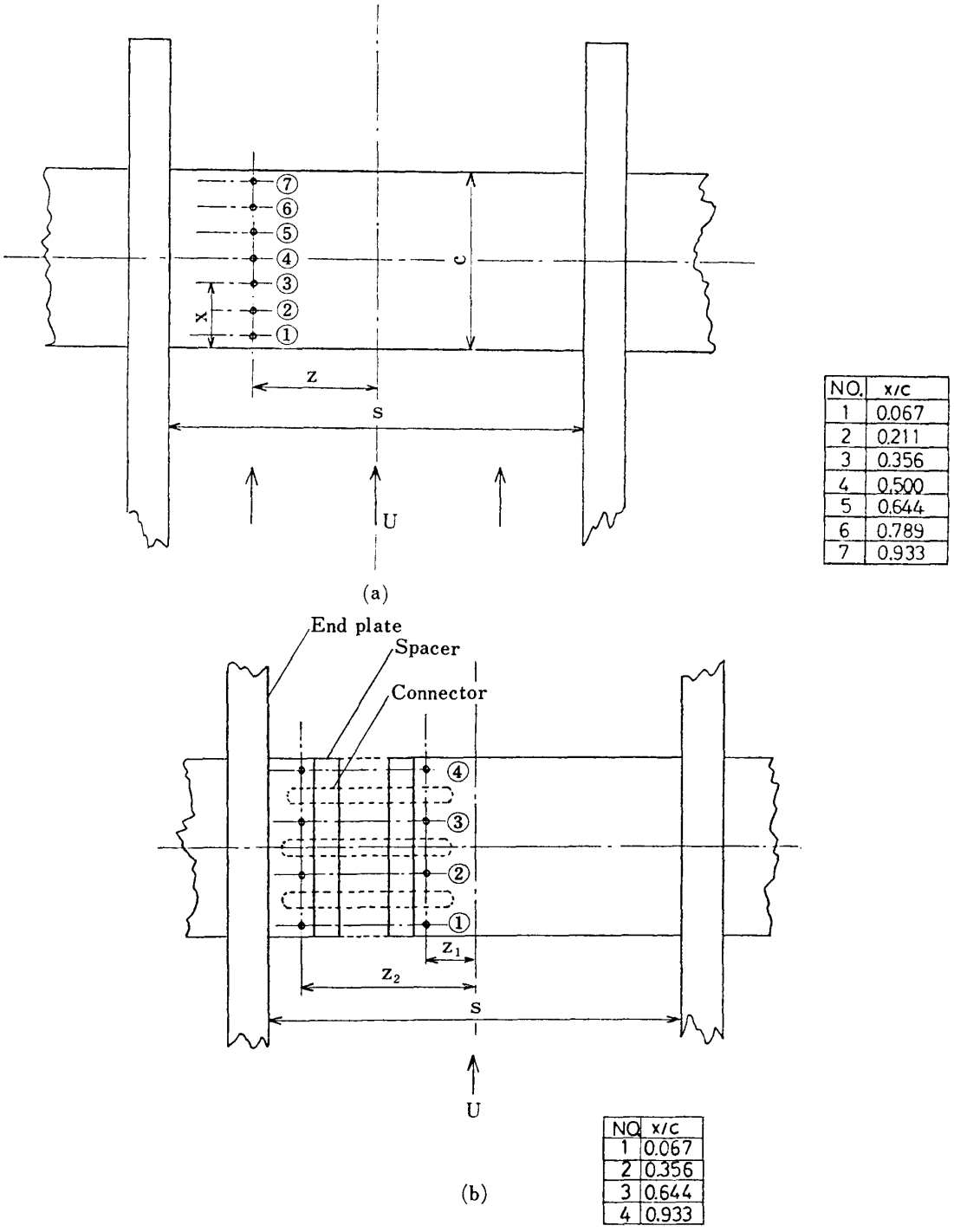


| NO. | x/c |
|---|---|
| 1 | 0.067 |
| 2 | 0.211 |
| 3 | 0.356 |
| 4 | 0.500 |
| 5 | 0.644 |
| 6 | 0.789 |
| 7 | 0.933 |

| NO. | x/c |
|---|---|
| 1 | 0.067 |
| 2 | 0.356 |
| 3 | 0.644 |
| 4 | 0.933 |

FIG. 4-2. Pinhole position for surface-pressure measurement; (a) Chordwise direction, (b) Spanwise direction.

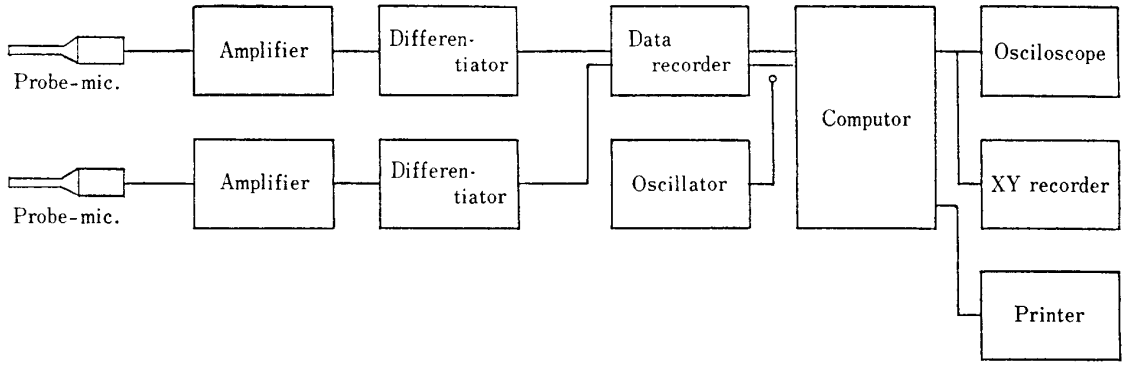


FIG. 4–3. Block diagram of instrumentation for surface-pressure correlation measurement.

where $Q$ denotes the acoustic source strength per unit surface area,

$$Q(x, z)=A_c(x, z)\cdot\overline{\dot{p}_s(x, z)^2}. \tag{9}$$

The correlation area can be obtained by measurement of the cross-correlation of the surface-pressure time-derivatives with Eq. (7). It may be convenient for this purpose to introduce chordwise and spanwise correlation lengths of surface-pressure time-derivatives, $X_c$ and $Z_c$, defined by respectively,

$$\begin{aligned} X_c(x, z)&=\int_{-c}^{c}\frac{\langle\dot{p}_s(x, z, t)\dot{p}_s(x', z, t+\tau)\rangle_{\max}}{\langle\dot{p}_s(x, z, t)\dot{p}_s(x, z, t+\tau)\rangle_{\tau=0}}dx', \\ Z_c(x, z)&=\int_{-s/2}^{s/2}\frac{\langle\dot{p}_s(x, z, t)\dot{p}_s(x, z', t+\tau)\rangle_{\max}}{\langle\dot{p}_s(x, z, t)\dot{p}_s(x, z, t+\tau)\rangle_{\tau=0}}dz'. \end{aligned} \tag{10}$$

If the correlation area is assumed to be of an ellipse, these lengths are related to the area by

$$A_c(x, z)=\frac{\pi}{4}X_c(x, z)Z_c(x, z) \tag{11}$$

The chordwise correlation length was obtained by measuring the surface pressure at seven pinholes of which interval was 6.5 mm as shown in Fig. 4–2(a). The spanwise correlation length was measured by four pinholes in two rows of which interval distance was variable by 6.0 mm step with inserting spacers as shown in Fig. 4–2(b). A block diagram of the instrumentation is illustrated in Fig. 4–3. The fluctuating wall-surface pressures were measured by two probe-microphones. Their output signals were fed to analog differentiators and then to a data recorder. The recorded signals were corrected for the transfer response of the probe-microphone to obtain the cross-correlation.

4–2 *Dipole strength*

(a) Fluctuating wall-surface pressure

Figures 4–4 and 4–5 show the static surface pressure and root mean-square fluctuat-

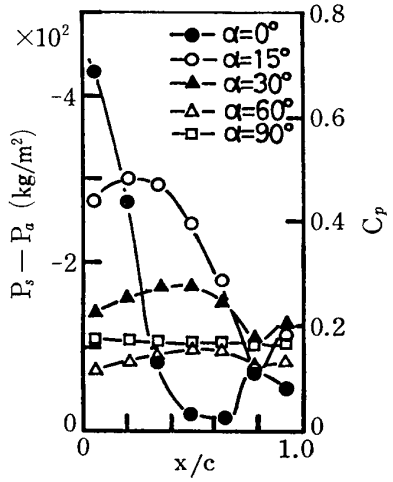


Plate 5×45
U=100m/s

FIG. 4–4. Static pressure distribution; $t\times c=5=45$, $U=100$ m/s.

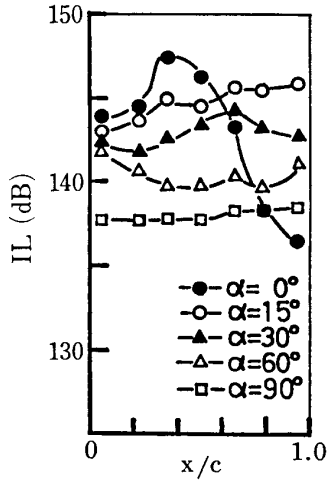


Plate 5×45
U=100m/s

FIG. 4–5. Fluctuating surface-pressure distribution; $t\times c=5\times 45$, $U=$ 100 m/s.

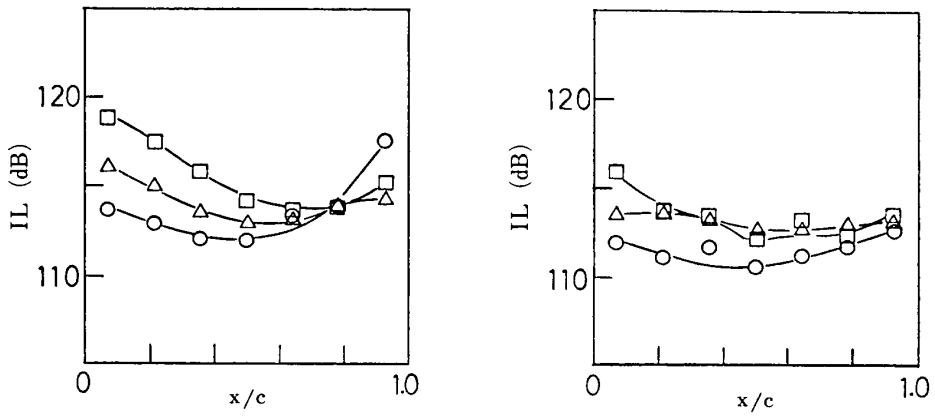


FIG. 4–6. Fluctuating surface-pressure distribution; $t\times c=5\times 45$, $s=100$ mm, $U=$ 30 m/s, (a) $\alpha=30°$, (b) $\alpha=60°$.

ing surface-pressure along the plate chord, respectively, which were measured with the equipment used in chapter 2. The pressure level $IL$ is defined as

$$IL=10\log\frac{\overline{p_s^2}}{\overline{p_{s0}^2}} \qquad \sqrt{\overline{p_{s0}^2}}=2\times 10^{-4}\ \mu\text{bar}$$

For $\alpha>30°$, both pressures are distributed uniformly over the surface; the fluctuating surface pressure is about 20% of the static pressure and 3% of the total pressure for the case of $p_t-p_a=-1.0\times 10^2$ kg/m² and $IL=140$ dB ($\sqrt{\overline{p_s^2}}\approx 2\times 10^{-3}$ bar). It should be noted that the fluctuating surface pressures shown in Fig. 4–5 are not corrected for the frequency response of the probe-microphone, being about 5 dB higher than

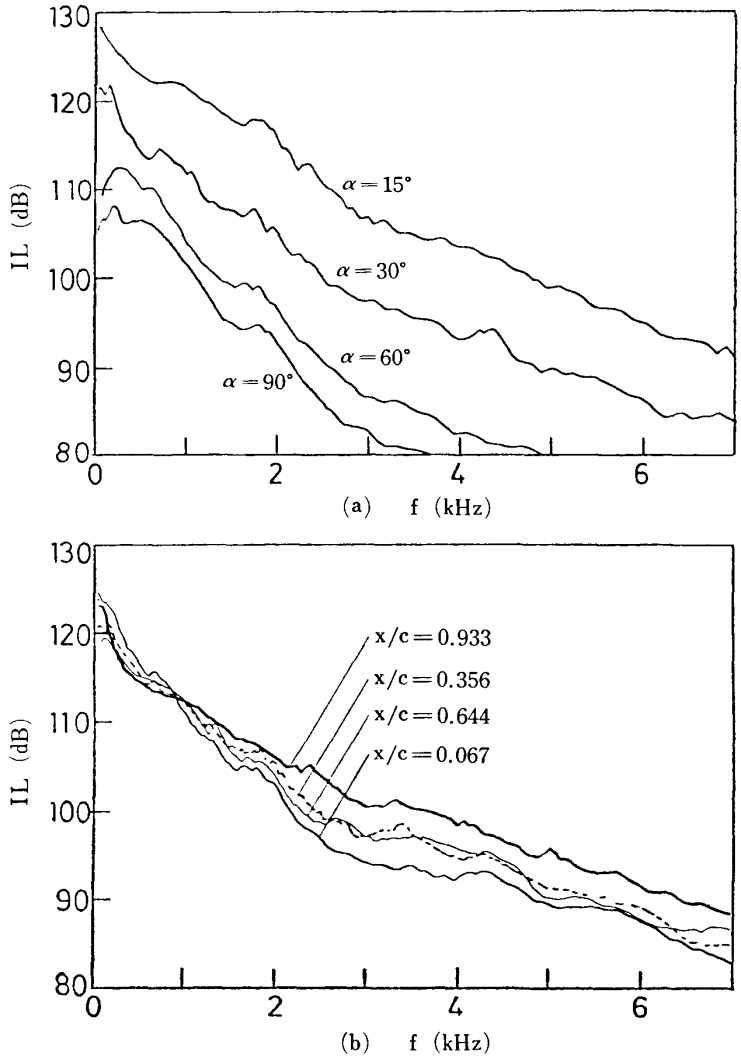


FIG. 4–7. Frequency spectra of surface pressure; $t\times c=5\times 45$, $s=84$ mm, $U=100$ m/s, $z=0$, (a) Effect of attack angle ($x/c=0.356$), (b) Effect of chordwise position ($\alpha=30°$).

the corrected. The corrected-pressure distribution obtained by the present equipment is shown in Fig. 4–6 at different spanwise positions. At both $\alpha=30°$ and 60°, they show a uniform chordwise distribution near the span center, although close to the end plate the pressure fluctuation takes larger amplitude at the leading edge. If the pressure fluctuation is assumed to be proportional to the square of the mean flow velocity, the pressure level of 113 dB at $U=30$ m/s in Fig. 4–6 corresponds to 134 dB at $U=100$ m/s which is close to the corrected levels in Fig. 4–5.

The power spectral density of the fluctuating wall-surface pressure shown in Figs. 4–7 and 4–8 has a peak at about 100 Hz and an attenuation of about 5 to 10 dB per 1 kHz at high frequencies. The spectra are hardly affected by the mean flow velocity. As shown in Fig. 4–7(a), with increasing attack angle the spectral density is shifted to lower frequencies and has a larger attenuation at higher frequencies. It is seen from Fig. 4–7(b) that the spectra are almost similar over the surface although near

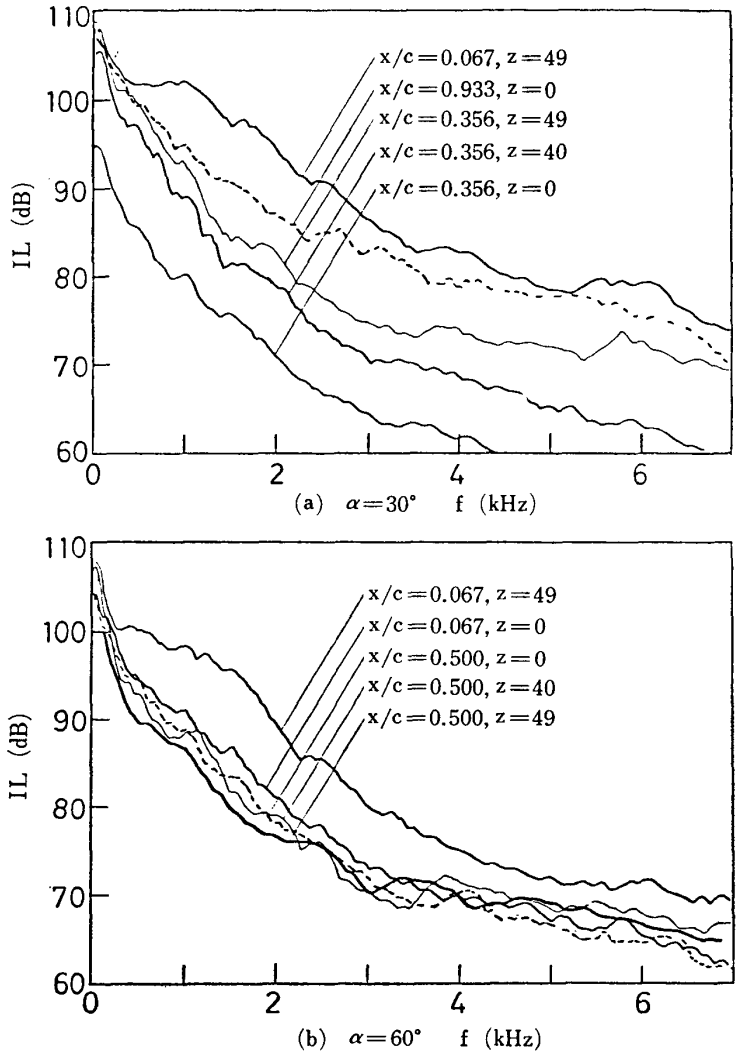


FIG. 4–8. Frequency spectra of surface pressure; $t\times c=5\times 45$, $s=100$ mm, $U=30$ m/s, (a) $\alpha=30°$, (b) $\alpha=60°$.

the leading edge they include slightly large amount of higher frequency components.

The effect of the end plate on the spectra is shown in Fig. 4–8. As far as the spectrum is concerned, the observation point does not provide any difference except for the overall level.

(b) Time-derivative of fluctuating wall-surface pressure

Figure 4–9 shows the mean-square time-derivative of fluctuating wall-surface pressure in the relation to the oncoming flow velocity. The coordinate of the figure, DPIL, represents the intensity level of the time derivative of fluctuating pressure on the wall-surface in decibel (dB) referred to $2\times 10^{-4}$ $\mu$bar at 1 kHz;

$$\mathrm{DPIL\,(dB)}=10\log\frac{\overline{\dot{p}_s^2}}{\omega_0^2\overline{p_{s0}^2}}$$

$$\omega_0=2\pi\times 1000\ \mathrm{Hz},\quad \sqrt{\overline{p_{s0}^2}}=2\times 10^{-4}\ \mu\mathrm{bar}$$

The data for the flow velocity higher than 50 m/s were obtained with the wind tunnel

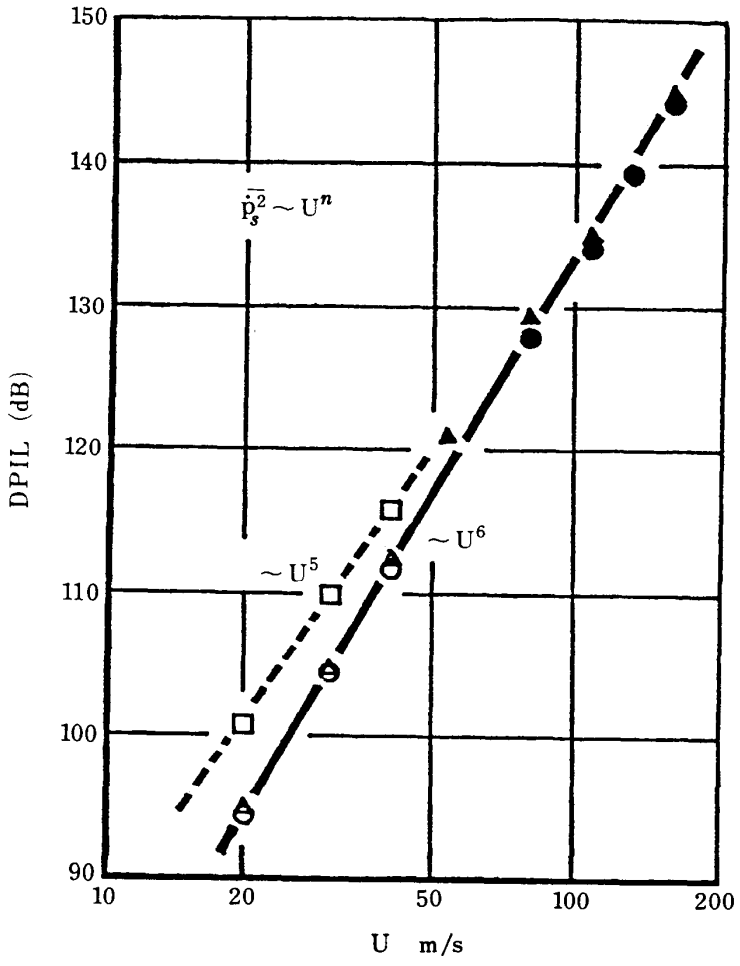


FIG. 4–9. Surface-pressure time-derivative vs. flow-velocity; $t \times c = 5 \times 45$, $\alpha = 30°$, $z = 0$.

used in the preceding chapter and those for lower velocities were measured by the present wind tunnel. Both data show consistent features on a straight line $U^6$. The values on $U^5$ line are at the trailing edge of the plate. Since the latter acts as a weak acoustic source as seen later, the mean-square time derivative of fluctuating wall-surface pressure can be said to be proportional to the sixth power of the oncoming flow velocity, which brings a straightforward contribution to the sixth-power relation of the acoustic intensity with the flow velocity.

The chordwise distribution of the mean-square time derivative of fluctuating wall-surface pressure is illustrated in Fig. 4–10 for the case of $\alpha = 30°$. The mean-square takes slightly small values near the leading edge and slightly large values near the trailing edge, although it is distributed rather uniformly over the chordwise distance without any appreciable variation. Close to the end plate, however, it increases markedly near the leading edge. In Figs. 4–11(a) to (f), the spanwise distributions

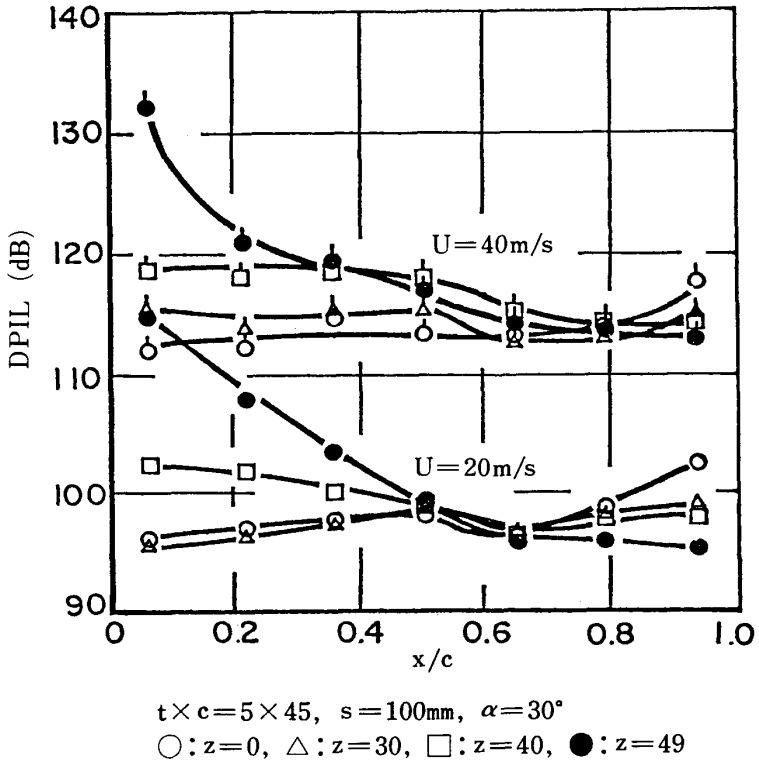


FIG. 4–10. Chordwise distribution of surface-pressure time-derivative; $t \times c = 5 \times 45$, $s = 100$ mm, $\alpha = 30°$.

of the mean-square time-derivative pressure on both surfaces faced to the separated flow and to the oncoming flow are presented for $\alpha = 30°$(a, b), 60°(c, d), 90°(e) with $s = 100$ mm and $\alpha = 30°$, $s = 70$ mm(f). On the separated surface the values are found to be distributed uniformly in the spanwise direction over the surface of about 60% span length. Closer to the end plate, $z \geqslant 0.6\, s/2$, they increases remarkably at the leading edge. At $\alpha = 90°$, the uniformity of distribution appears remarkable over the larger surface area of the plate than it does at $\alpha = 30°$ and 60°. On the surface faced to the oncoming flow, the opposite side to the separated surface, the mean-square values also take a uniform distribution over the surface of about 70% span length, being about 3 dB lower than those on the separated surface. Close to the end plate on this surface, they increase over the whole chordwise length. In the vicinity of the unseparated surface, appreciable velocity turbulences, hence turbulent surface pressures are unlikely to be associated with. The observed fluctuating pressures on the surface may be attributed to those propagated from the separated surface.

The effect of the span length on the mean-square levels of the surface-pressure time-derivative at the span center is shown in Fig. 4–12. The levels are constant for $s \geqslant$ 70 mm. It means that the end plates should hardly affect the level provided that they are separated farther than 1.5 times the chord length.

Consequently, the mean-square time derivative of wall-surface pressure is approximately uniformly distributed over the surface area of about the chord length and 70% of the span length, being proportional to the sixth power of the oncoming flow velocity. These features are hardly affected by the attack angle of the plate.

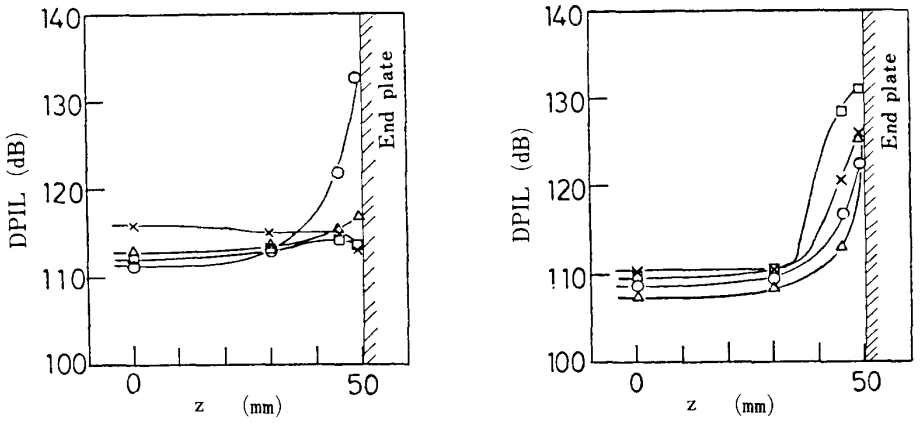


(a) s=100, $\alpha$=30°, Separated surface (b) s=100, $\alpha$=30°, Upstream surface

○ : x/c=0.067, △ : x/c=0.356, □ : x/c=0.644, × : x/c=0.933

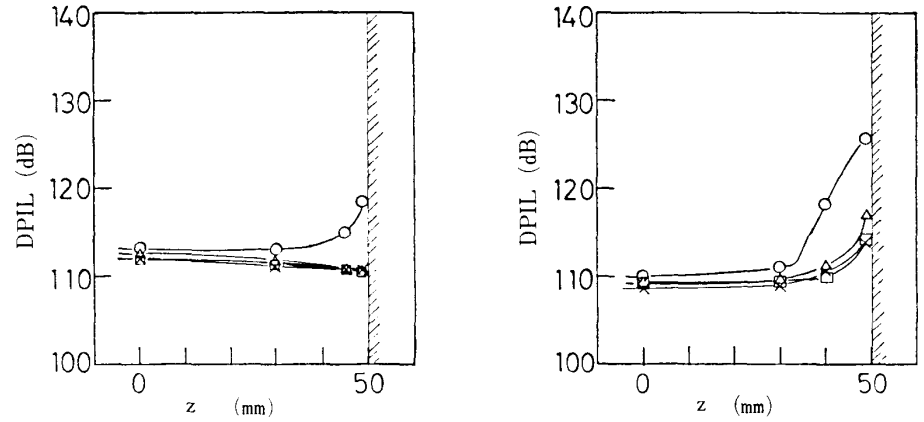


(c) s=100, $\alpha$=60°, Separated surface (b) s=100, $\alpha$=60°, Upstream surfac

○ : x/c=0.067, △ : x/c=0.356, □ : x/c=0.644, × : x/c=0.933

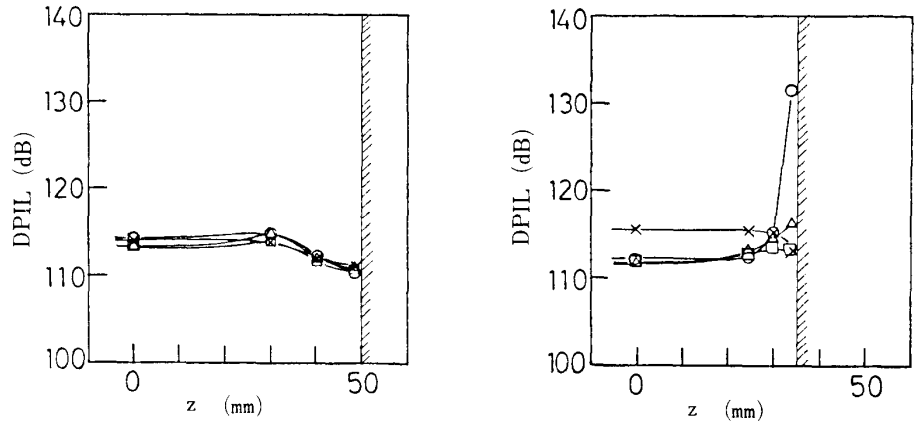


(e) s=100, $\alpha$=90°, Separated surface (f) s=70, $\alpha$=30°, Separated surface

○ : x/c=0.067, △ : x/c=0.356, □ : x/c=0.644, × : x/c=0.933

FIG. 4-11. Spanwise distribution of surface-pressure time-derivative.

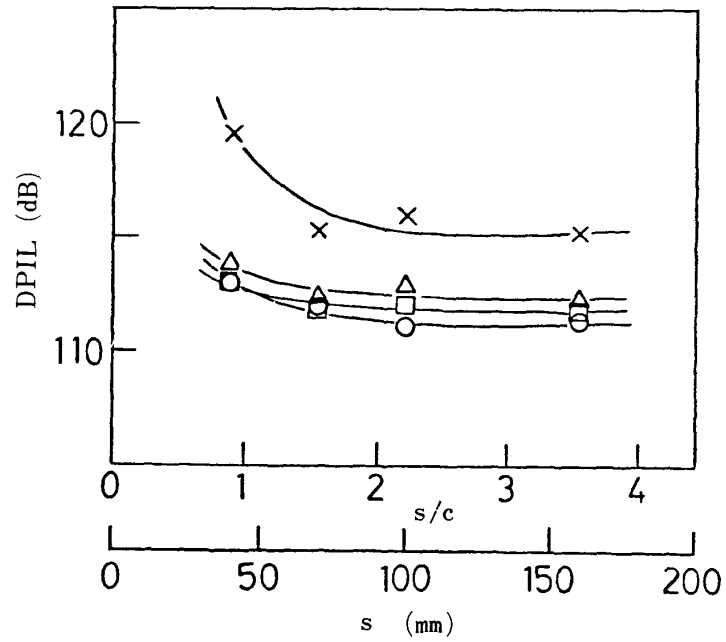


○ : x/c=0.067, △ : x/c=0.356
□ : x/c=0.644, × : x/c=0.933

FIG. 4-12. Effect of span length on surface-pressure time-derivative; $t\times c=5\times 45$, $U=40$ m/s, $z=0$.

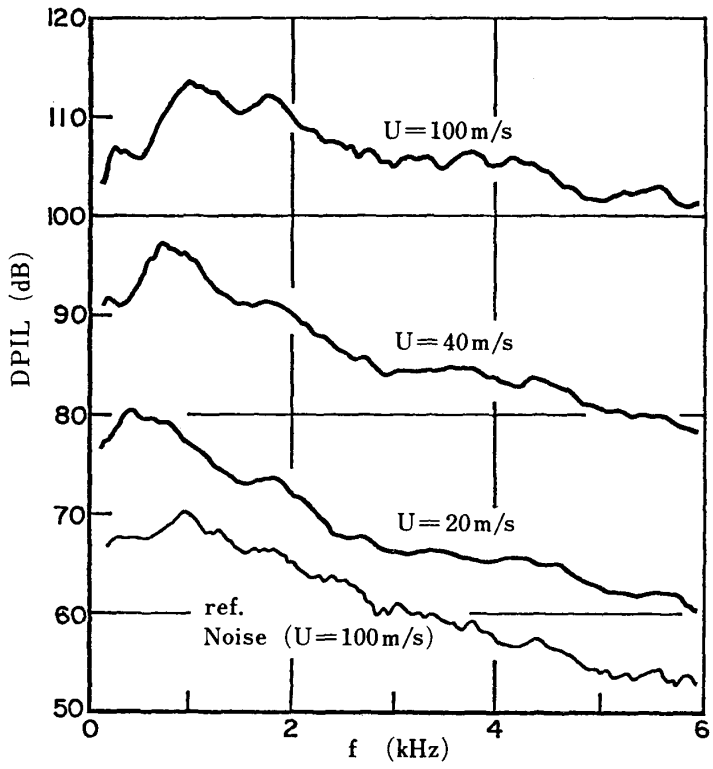


t×c=5×45, s=100mm, $\alpha=30°$, x/c=0.356, z=0

FIG. 4-13. Frequency spectra of surface-pressure time-derivative at different flow velocities; $t\times c=5\times 45$, $s=100$ mm, $\alpha=30°$, $x/c=0.356$, $z=0$.

(c) Frequency spectrum of surface-pressure time-derivative

Typical frequency spectra of surface-pressure time-derivative are shown in Fig. 4–13. They take a maximum at a frequency between 400 Hz and 1.2 kHz. The peak frequency becomes slightly higher as the flow velocity increases. Above the peak frequency, the spectral density decreases gradually with increasing frequency. The attenuation at higher frequencies tends to be reduced with increasing flow velocity. The spectral features resemble those of the associated acoustic pressure as shown in the figure. If the frequency is nondimensionalized based on the flow velocity and the plate chord, the peak of the spectral density occurs at the nondimensional frequency of 0.3 to 0.4. At higher frequencies, however, the spectra with respect to the non-dimensional frequency are not well-correlated.

The frequency spectra at the different points of the plate surface are shown in Fig. 4–14. Closer to the trailing edge, they have more high-frequency components, although the difference in the shape is not appreciable. In the vicinity of the end plate, the spectra have little difference except close to the leading edge, although they are somewhat different from those at the span center, having less high-frequency

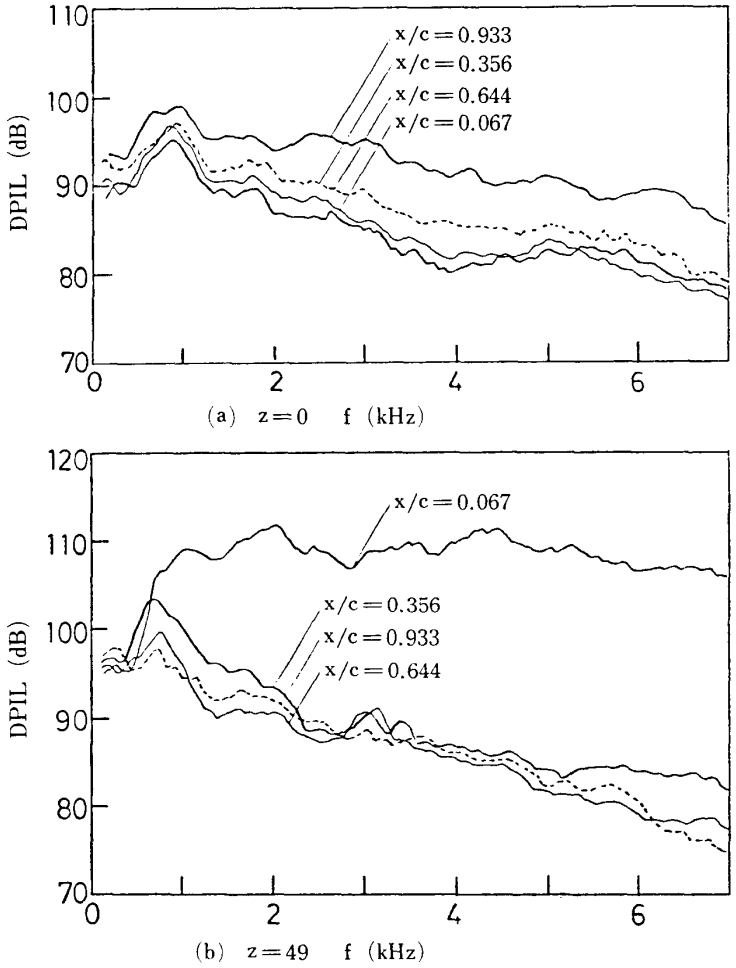


FIG. 4–14. Frequency spectra of surface-pressure time-derivative at different points on separated surface; $t \times c = 5 \times 45$, $s = 100$ mm, $\alpha = 30°$, $U = 40$ m/s.

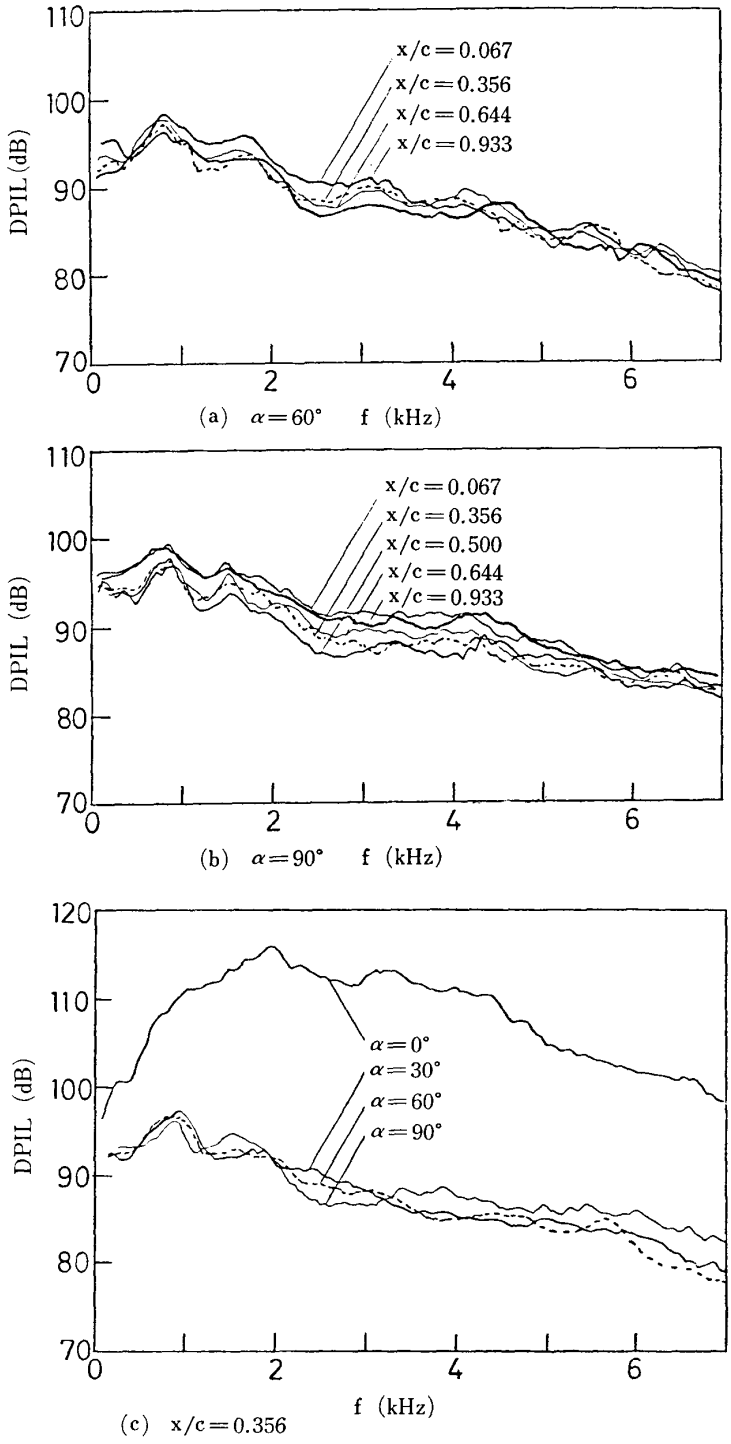


FIG. 4–15. Frequency spectra of surface-pressure time-derivative on separated surface at different attack angles; $t \times c = 5 \times 45$, $s = 100$ mm, $U = 40$ m/s, $z = 0$.

components. In Figs. 4–15(a) and (b), the spectra at $\alpha = 60°$ and 90°, respectively, are shown. They hardly differ from each other, being almost accordant. These spectra are also hardly affected by the attack angle as seen in Fig. 4–15(c).

The frequency spectra of surface-pressure time-derivative on the surface faced to

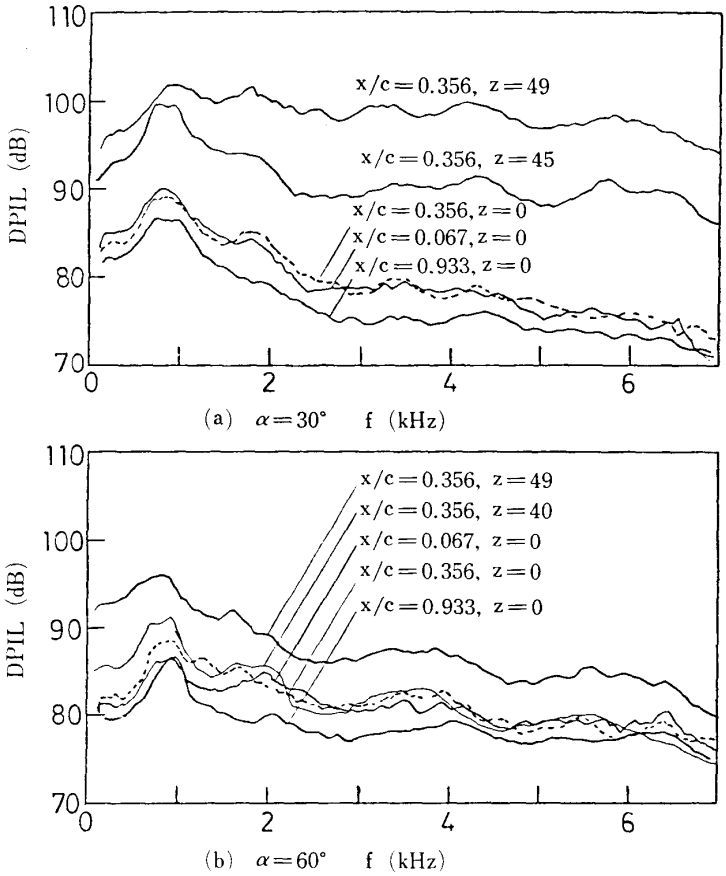


FIG. 4–16. Frequency spectra of surface-pressure time-derivatice at different points on upstream surface; $t \times c = 5 \times 45$, $s = 100$ mm, $U = 30$ m/s.

the oncoming flow are presented in Fig. 4–16. They are almost similar over the surface, having more high-frequency components compared with those on the separated surface. However, the difference between spectra on both surfaces is not remarkable. This also implies that the wall-surface pressure fluctuations on the unseparated upstream surface would be associated with those on the separated surface. The spectra close to the end plate are markedly different from those near the span center. This means the wall-surface pressure fluctuations close to the end plate generated by the other mechanism different from the flow separation.

In conclusion, the frequency spectra of surface-pressure time-derivative are closely similar to those of the associated acoustic pressure, having a broad-band peak at a frequency between 400 Hz and 1.2 kHz. They hardly change with the observed position on the surface and the attack angle of the plate. With increasing flow velocity, the peak frequency is shifted toward higher frequencies which are about $0.3 \sim 0.4$ in nondimensional frequency based on the flow velocity and the plate chord.

### 4–3 *Correlation area*

(a) Correlation coefficients

The correlation of the surface-pressure time-derivatives at two different points on the separated surface and on the upstream surface is indicated in Figs. 4–17(a) to (g).

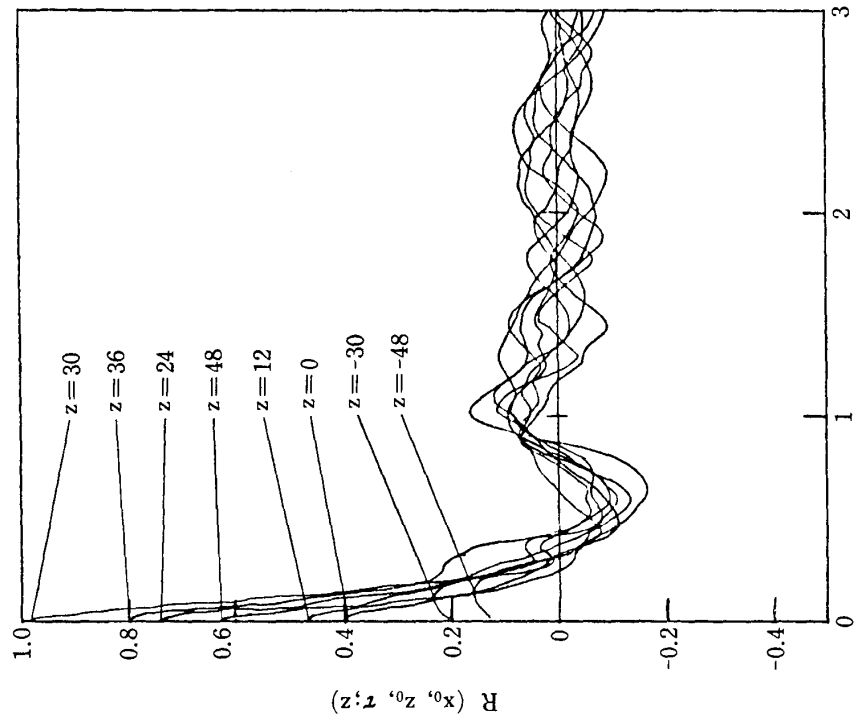


(b) $\alpha=30°$, $x_0/c=0.356$, $z_0=30$

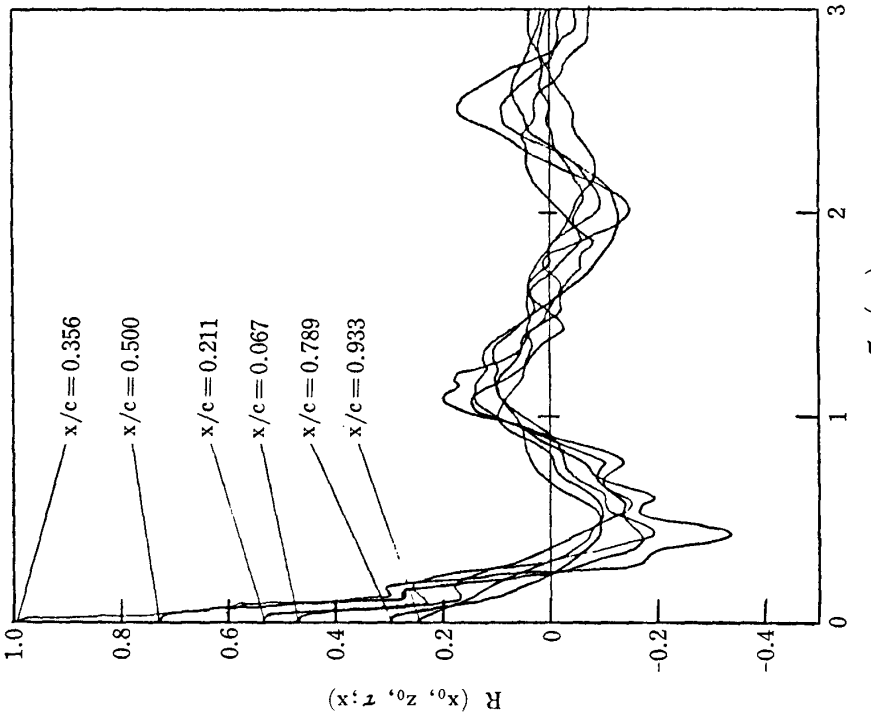


(a) $\alpha=30°$, $x_0/c=0.356$, $z_0=30$

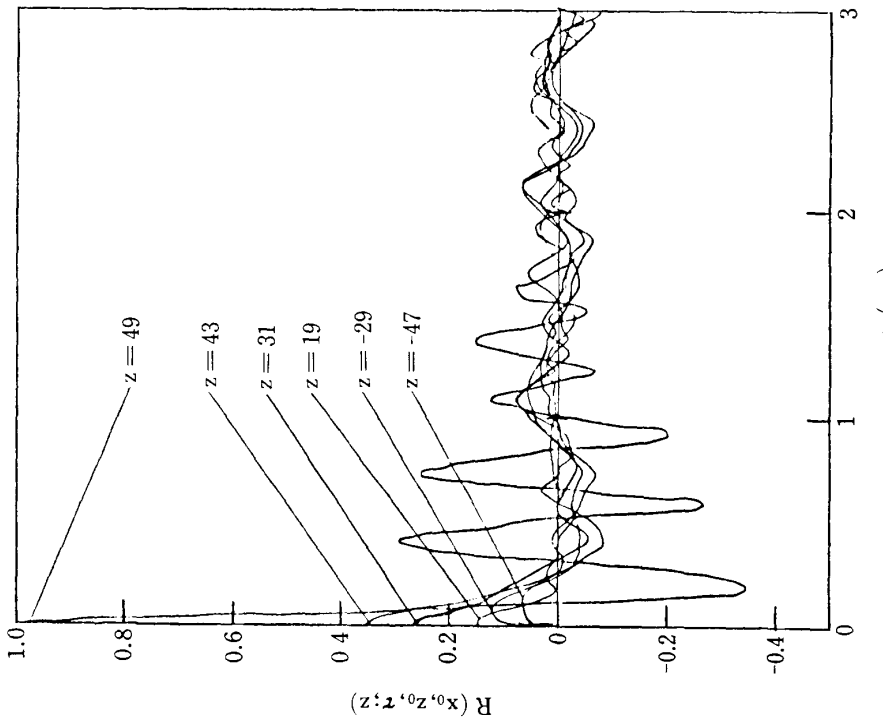


(e) $\alpha = 30°$, $x_0/c = 0.067$, $z_0 = 49$

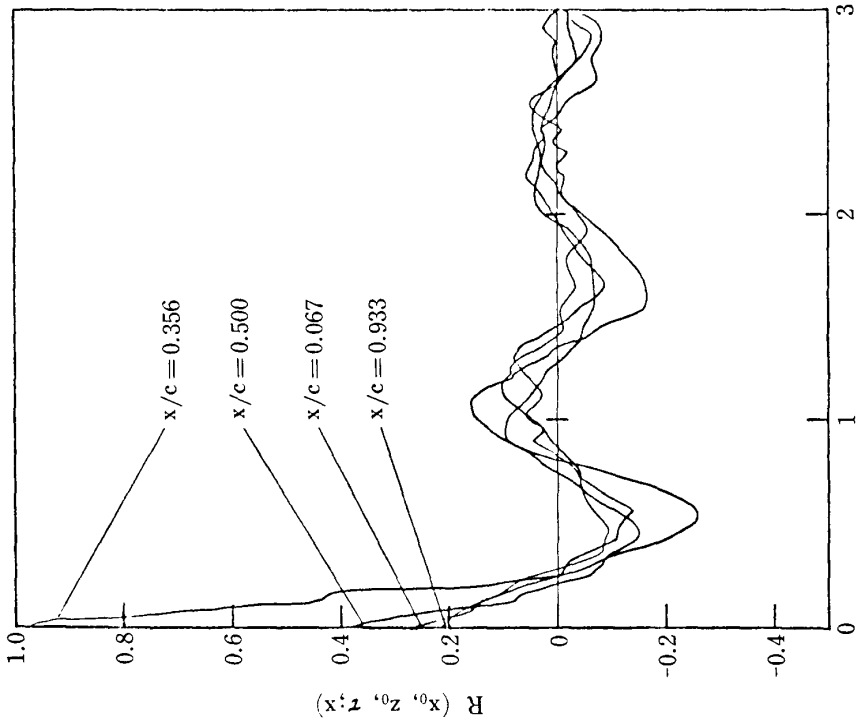


(c) $\alpha = 60°$, $x_0/c = 0.356$, $z_0 = 0$

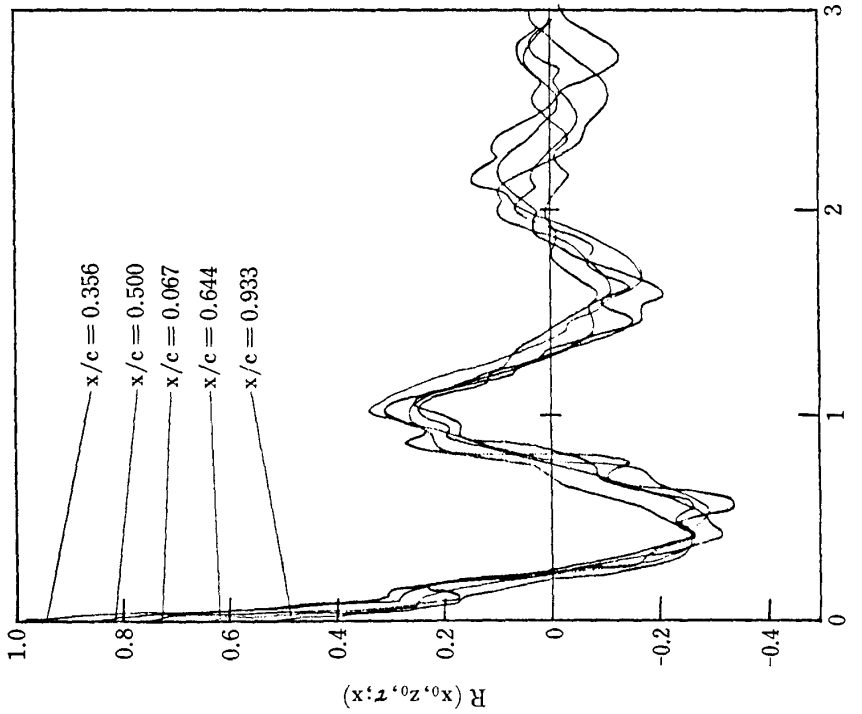


(f) Upstream surface, $\alpha = 30°$, $x_0/c = 0.356$, $z_0 = 0$

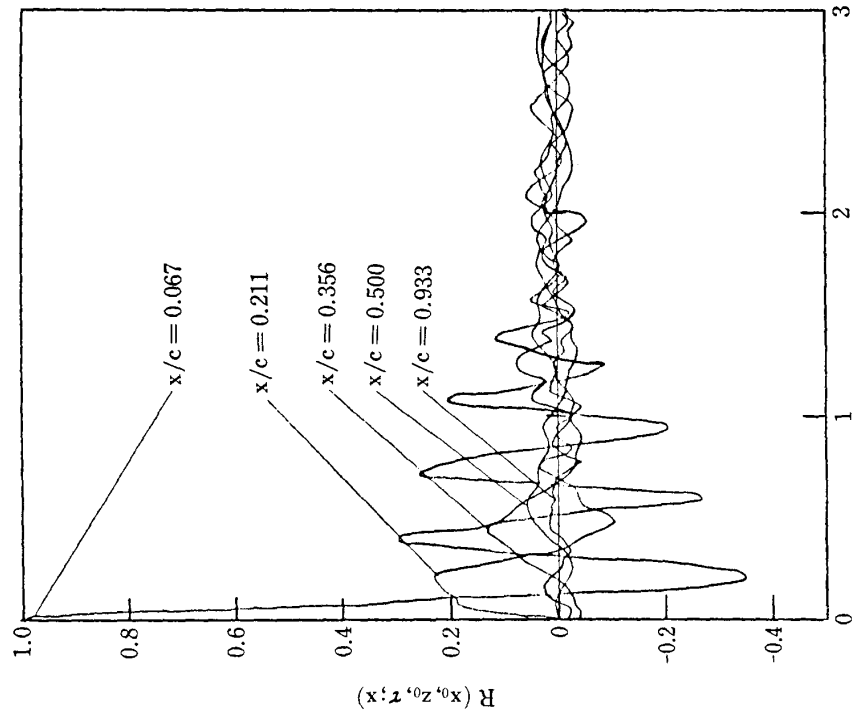


(d) $\alpha = 30°$, $x_0/c = 0.067$, $z_0 = 49$

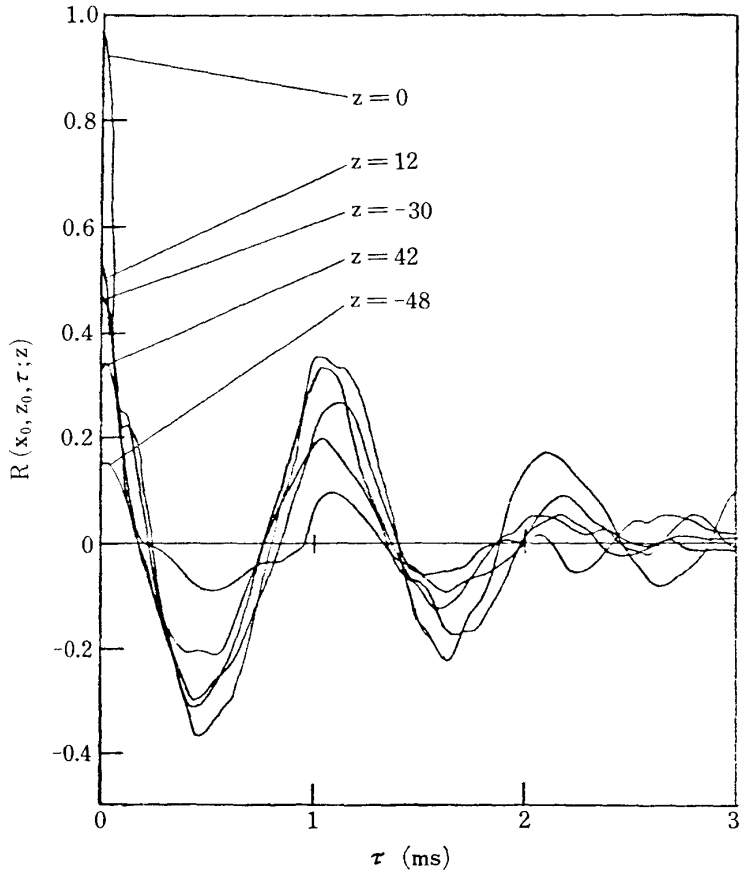


(g) Upstream surface, $\alpha=30°$, $x_0/c=0.356$, $z_0=0$

FIG. 4–17. Correlation of surface-pressure time-derivatives; $t\times c=5\times 45$, $s=100$ mm, $U=40$ m/s.

In Figs. 4–17(a) and (b), the chordwise and spanwise correlations are shown for $\alpha=30°$ referred to the point $x_0/c=0.356$ and $z_0=30$ mm. Here, the chordwise and spanwise correlations are normalized by the mean-square of the surface-pressure time-derivative at the point;

$$R(x_0, z_0, \tau; x)=\frac{\langle \dot{p}_s(x_0, z_0, t)\dot{p}_s(x, z_0, t+\tau)\rangle}{\{\dot{p}_s(x_0, z_0, t)\}^2},$$
$$R(x_0, z_0, \tau; z)=\frac{\langle \dot{p}_s(x_0, z_0, t)\dot{p}_s(x_0, z, t+\tau)\rangle}{\{\dot{p}_s(x_0, z_0, t)\}^2}. \tag{12}$$

Both correlations take a maximum at a retarded time. As the distance between the points increases, the correlation decreases and the retarded time of its maximum increases. The features of the correlations are little affected by the attack angle (Fig. 4–17(c)). As mentioned before, however, close to the end plate, the different features of surface-pressure fluctuation yield different behavior of the correlations (Fig. 4–17 (d) and (e)). Figures 4–17(f) and (g) show the correlations on the upstream surface. Since the pressure fluctuations on the surface are highly attributed to the propagation of those from the separated surface, they are highly correlated with over the whole

surface even with those on the separated surface.

The chordwise and spanwise correlation coefficients, $R_x$ and $R_z$, can be defined as the maximum of the correlations with respect to $\tau$;

$$\begin{aligned} R_x(x_0, z_0; x) &= R(x_0, z_0, \tau; x)_{\max}, \\ R_z(x_0, z_0; z) &= R(x_0, z_0, \tau; z)_{\max}. \end{aligned} \tag{13}$$

These coefficients are shown in Figs. 4–18 to 4–20 in the chordwise and spanwise distribution. They are distributed symmetrically with respect to the reference point except for close to the end plate. At the trailing edge, $R_z$ takes a sharp distribution, implying a small correlation scale of pressure fluctuation. These coefficient distributions are not appreciably affected by the attack angle and the span length (Fig. 4–20 (a, b, c)) although $R_z$ takes relatively smaller values for $\alpha=90°$ (Fig. 4–20(b)). Both coefficients on the upstream surface are of largely diffused distribution, indicating well-correlated pressure fluctuations over the surface (Fig. 4–20(d, e)).

(c) Correlation lengths and correlation area

The correlation lengths defined by Eq. (10) are expressed with the correlation coefficients as

$$\begin{aligned} X_c(x, z) &= \int_{-c}^{c} R_x(x, z; x')dx', \\ Z_c(x, z) &= \int_{-s/2}^{s/2} R_z(x, z; z')dz'. \end{aligned} \tag{14}$$

The correlation area $A_c$ is given by Eq. (11). These correlation lengths are shown

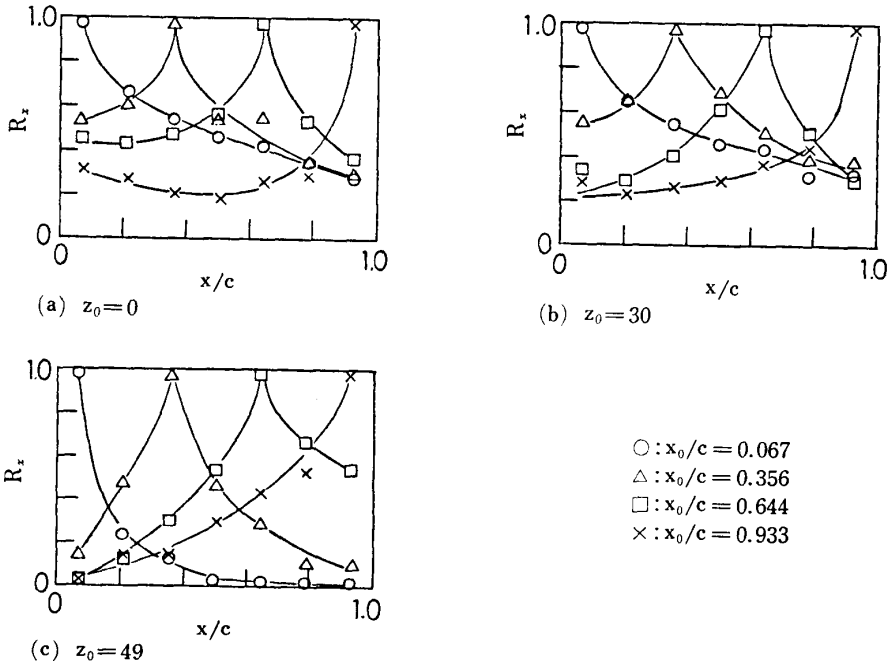


FIG. 4–18. Chordwise distribution of correlation coefficient $R_x$; $t\times c=5\times 45$, $s=100$ mm, $\alpha=30°$, $U=40$ m/s.

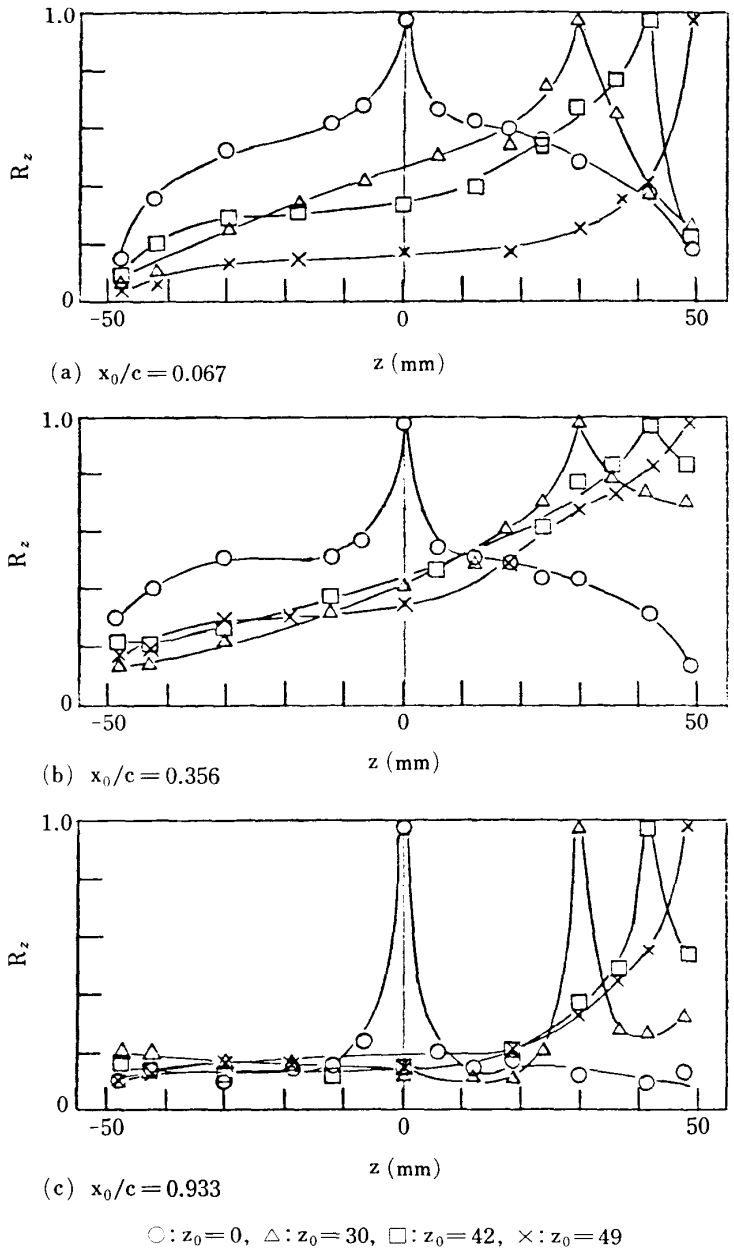


FIG. 4–19. Spanwise distribution of correlation coefficient $R_z$; $t\times c=5\times 45$, $s=100$ mm, $\alpha=30°$, $U=40$ m/s.

in Figs. 4–21(a) to (f). In the case of $\alpha=30°$ (Fig. 4–21(a)), both lengths take uniformly constant values over the surface except close to the end plate where they take smaller values. The constant values are about $X_c\simeq 0.6c$ and $Z_c\simeq(0.5\sim 0.6)s$. As a reference, in the figure, the similar correlation lengths of fluctuating surface pressures are presented. They take larger values than those of their time-derivatives, being about 80% of the chord and the span, respectively. In the case of $\alpha=60°$ (Fig. 4–21 (b)), the chordwise correlation length is shorter than that at $\alpha=30°$; $X_c\simeq 0.5c$. The spanwise length is about $Z_c=0.6s$ although close to the trailing edge it takes larger values. For $\alpha=90°$, Fig. 4–21(c) gives $X_c\simeq 0.5c$ and $Z_c=0.45s$. These features are

little affect by the span length as shown in Fig. 4–21(d) which gives the same values of $X_c/c$ and $Z_c/s$ both for $s=70$ mm and 100 mm.

The correlation lengths on the upstream surface are presents in Figs. 4–21(e) and (f). Both $X_c$ and $Z_c$ take larger values compared with those on the separated surface, being $0.8c$ and $0.8s$, respectively. Close to the end plate, they are remarkably reduced to smaller values. These are also mainly due to the propagation of the fluctuating surface pressure from the separated surface onto the upstream surface.

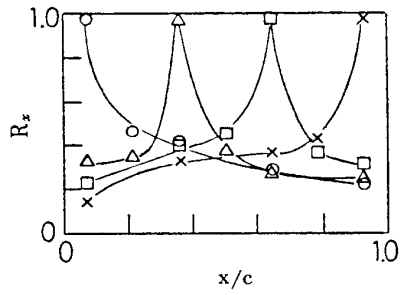


$R_x$, $z_0=0$
○:$x_0/c=0.067$, △:$x_0/c=0.356$
□:$x_0/c=0.644$, ×:$x_0/c=0.933$

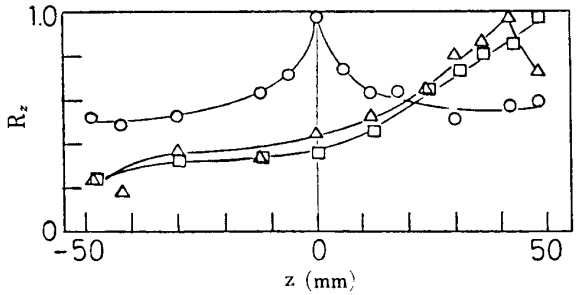


$R_z$, $x_0/c=0.356$
○:$z_0=0$, △:$z_0=42$, □:$z_0=49$

(a) $\alpha=60°$, s=100mm

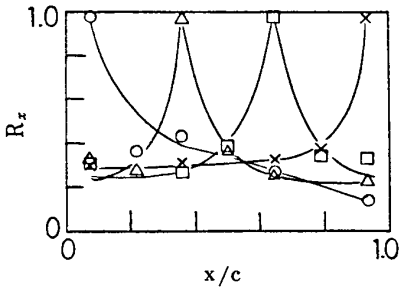


$R_x$, $z_0=0$
○:$x_0/c=0.067$, △:$x_0/c=0.356$
□:$x_0/c=0.644$, ×:$x_0/c=0.933$

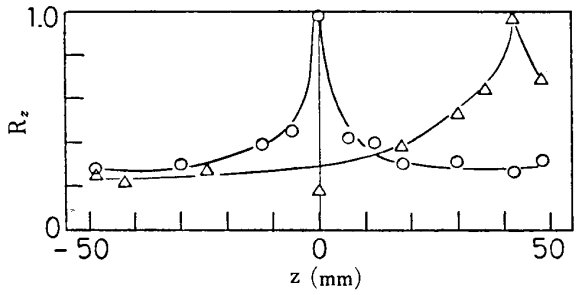


$R_z$, $x_0/c=0.356$
○:$z_0=0$, △:$z_0=42$

(b) $\alpha=90°$, s=100mm

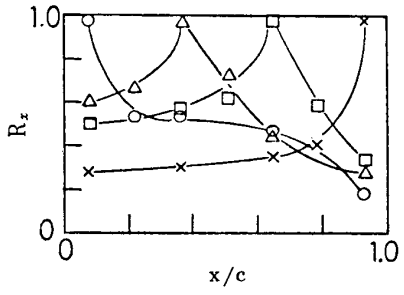


$R_x$, $z_0=0$
○:$x_0/c=0.067$, △:$x_0/c=0.356$
□:$x_0/c=0.644$, ×:$x_0/c=0.933$

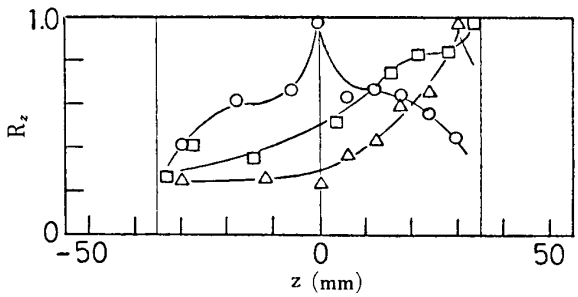


$R_z$, $x_0/c=0.356$
○:$z_0=0$, △:$z_0=30$, □:$z_0=34$

(c) $\alpha=30°$, s=70mm

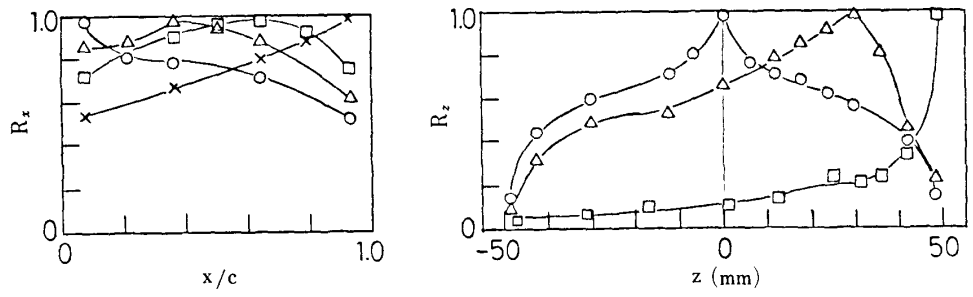


$R_x$, $z_0=0$
○:$x_0/c=0.067$, △:$x_0/c=0.356$
□:$x_0/c=0.644$, ×:$x_0/c=0.933$

$R_z$, $x_0/c=0.356$
○:$z_0=0$, △:$z_0=30$, □:$z_0=49$

(d) Upstream surface, $\alpha=30°$, s=100mm

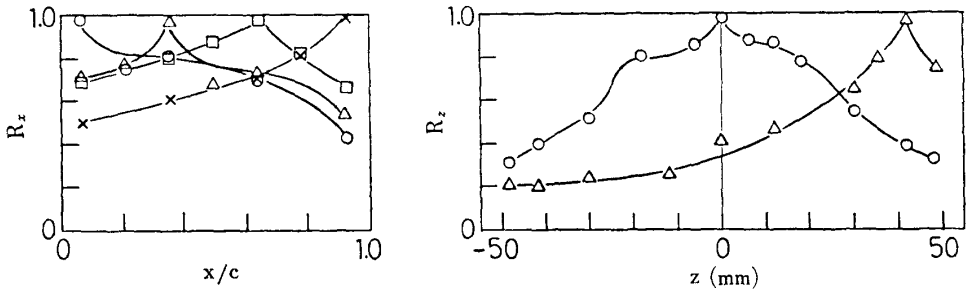


$R_x$, $z_0=0$
○:$x_0/c=0.067$, △:$x_0/c=0.356$
□:$x_0/c=0.644$, ×:$x_0/c=0.933$

$R_z$, $x_0/c=0.356$
○:$z_0=0$, △:$z_0=42$

(e) Upstream surface, $\alpha=60°$, s=100mm

FIG. 4–20. Distribution of correlation coefficients $R_x$ and $R_z$; $t\times c=5\times 45$, $U=40$ m/s.

Figure 4–22 gives the relationships of these correlation lengths with the oncoming flow velocity. The latter has little effect on the lengths. This is favorable for the prediction of the associated acoustic intensity with Eq. (8) in which only the surface-pressure time-derivative is relevant to the flow velocity.

In Fig. 4–23, the effect of the attack angle on the lengths is illustrated. $X_c$ hardly changes with the attack angle, whereas $Z_c$ changes markedly, taking a maximum at about $\alpha=60°$. In Fig. 4–24, the effect of the span lengh on the "constant" values of $X_c$ and $Z_c$ is shown. It is seen from the figure that $X_c$ takes a constant value for the span longer than $1.5c$. For shorter spans than $2.1c$, the values of $Z_c$ are approximately proportional to the span length; $Z_c=0.6s$,and for the larger than $2.2c$, they tend to keep constant; $Z_c=1.3c$. Thus, for the span length larger than about twice the chord, the lengths are not affected by the spanwise end condition of the plate, taking constant values uniformly over the plate surface which are a function of the attack angle.

The correlation areas defined by Eq. (11) are shown in Figs. 4–25(a) to (f). As well as the correlation lengths, the area takes uniformly a constant value over the large part of the plate surface except close to the end plate. In figures, the ratio of the correlation area to the geometrical plate-surface area is about 0.3 at $\alpha=30°$, 0.25 at $\alpha=60°$ and 0.15 at $\alpha=90°$, being decreased with the attack angle. In the case

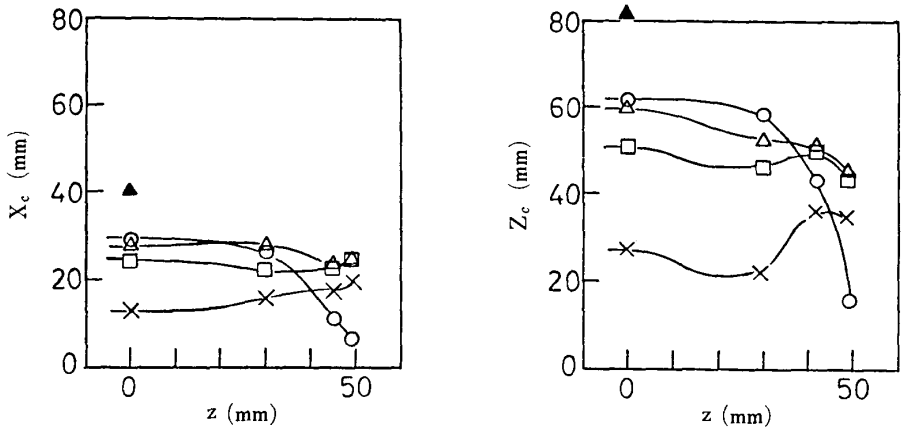


(a) $\alpha=30°$, s=100mm

○: x/c=0.067, △: x/c=0.356, □: x/c=0.644, ×: x/c=0.933
▲: $\langle p_s\ p_s \rangle$ correlation length (x/c=0.356)

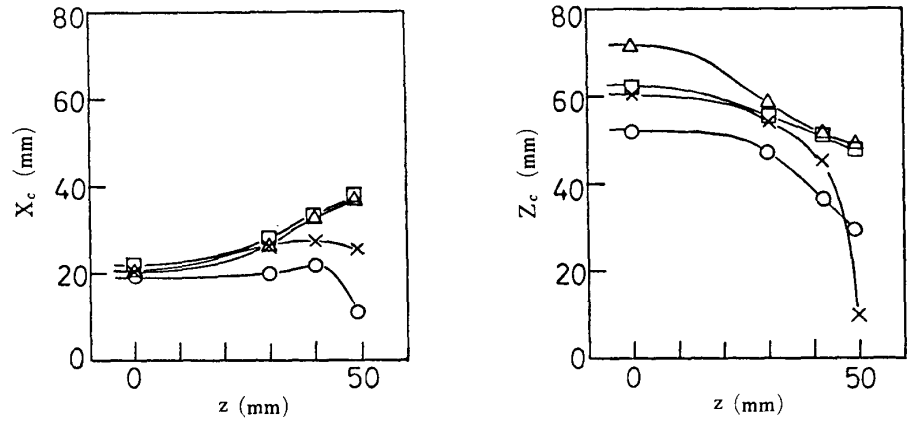


(b) $\alpha=60°$, s=100mm

○: x/c=0.067, △: x/c=0.356, □: x/c=0.644, ×: x/c=0.933

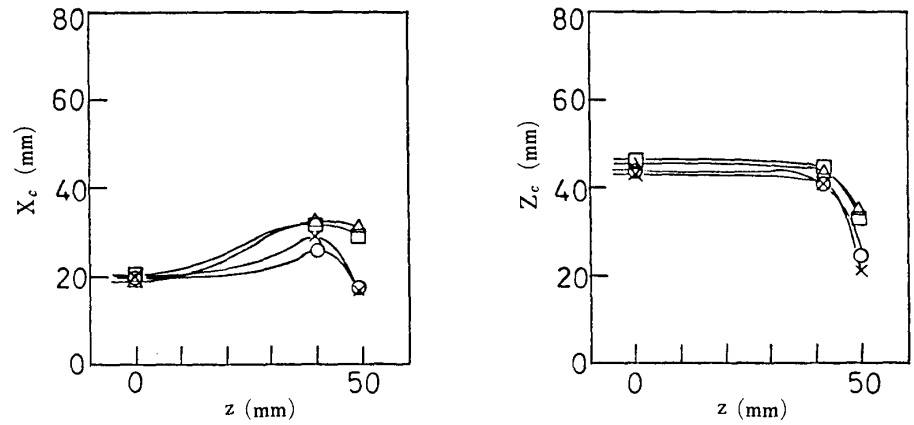


(c) $\alpha=90°$, s=100mm

○: x/c=0.067, △: x/c=0.356, □: x/c=0.644, ×: x/c=0.933

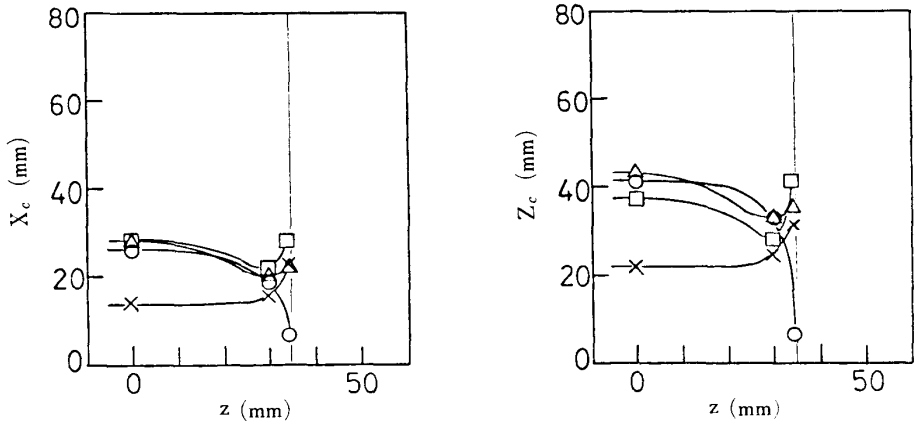


(d) $\alpha=30°$, s=70mm

○: x/c=0.067, △: x/c=0.356, □: x/c=0.644, ×: x/c=0.933

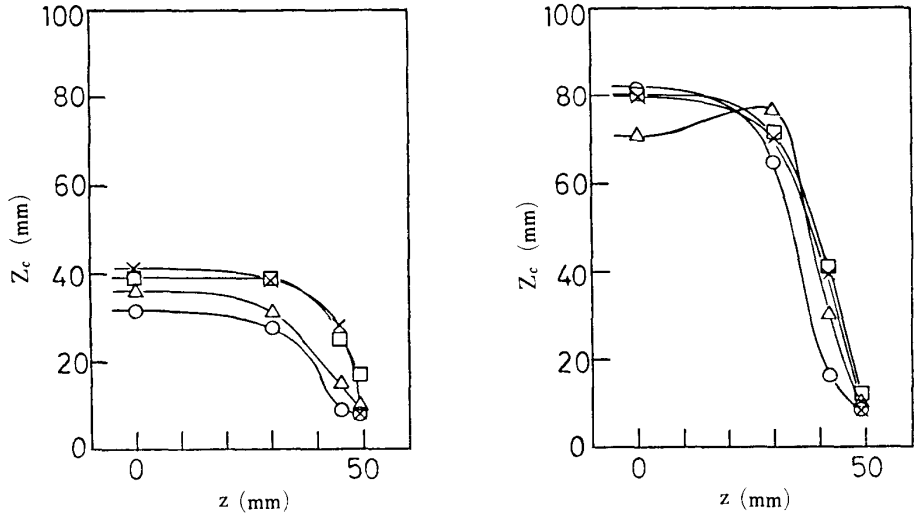


(e) Upstream surface, $\alpha=30°$, s=100mm

○: x/c=0.067, △: x/c=0.356, □: x/c=0.644, ×: x/c=0.933

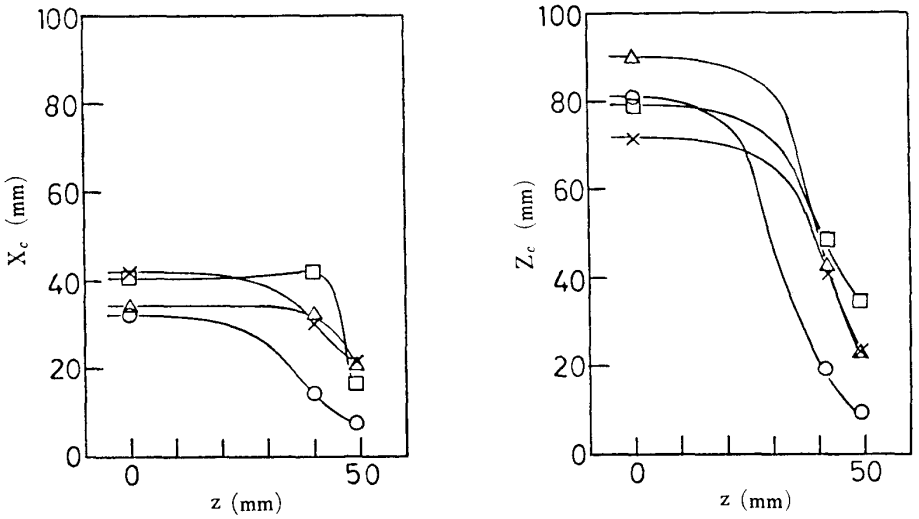


(f) Upstream surface, $\alpha=60°$, s=100mm

○: x/c=0.067, △: x/c=0.356, □: x/c=0.644, ×: x/c=0.933

FIG. 4-21. Correlation length distribution, $X_c$, $Z_c$; $t\times c=5\times 45$, $U=40$ m/s.

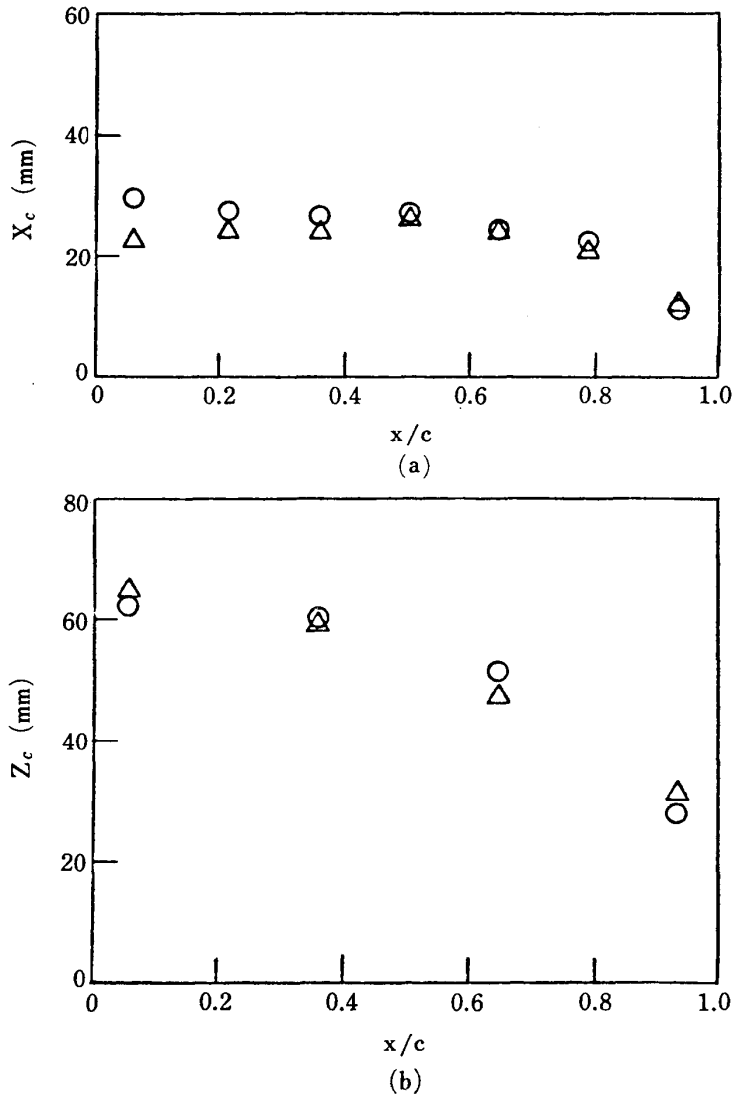


△ : U=20m/s, ○ : U=40m/s

FIG. 4-22. Effect of flow velocity on correlation lenghts; $t\times c=5\times 45$, $s=100$ mm, $\alpha=30°$, $z=0$.

of $s=70$ mm, it is also about 0.3 at $\alpha=30°$. On the upstream area, it becomes larger, being 0.5 at $\alpha=30°$ and at $\alpha=60°$. Referred to the chord length, these values of $A_c$ are $0.62c^2$ at $\alpha=30$, $0.51c^2$ at $\alpha=60°$ and $0.39c^2$ at $\alpha=90°$.

In summary, the correlation of surface-pressure time-derivatives has the following features;

(1) The surface-pressure time-derivatives are well-correlated both in the chordwise and spanwise directions except close to the end plate. On the upstream surface, they take higher correlations than on the separated surface.

(2) The correlation lengths take uniformly constant values except close to the end plate. The values are depend on the attack angle and not on the flow velocity. For spans longer than $2.2c$, they are approximately $X_c=0.6c$, $Z_c=1.3c$ at $\alpha=$

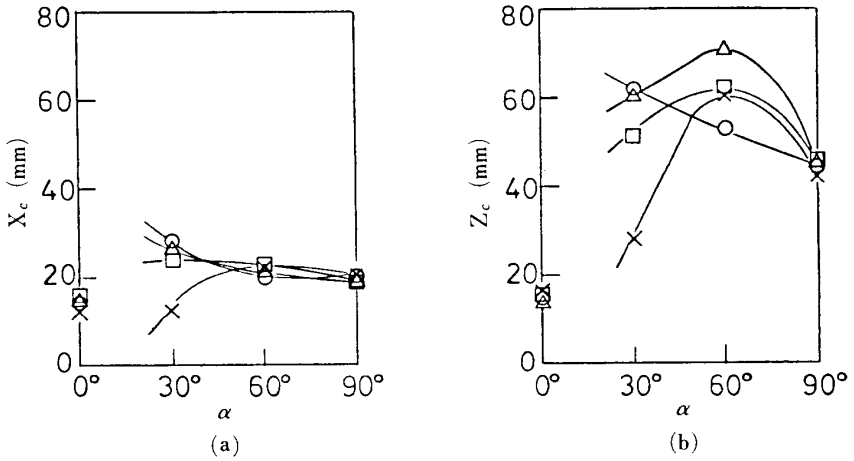


○: x/c=0.067, △: x/c=0.356, □: x/c=0.644, ×: x/c=0.933

Fig. 4-23. Effect of attack angle on correlation lengths; $t\times c=5\times 45$, $s=100$ m/s, $U=40$ m/s, $z=0$.

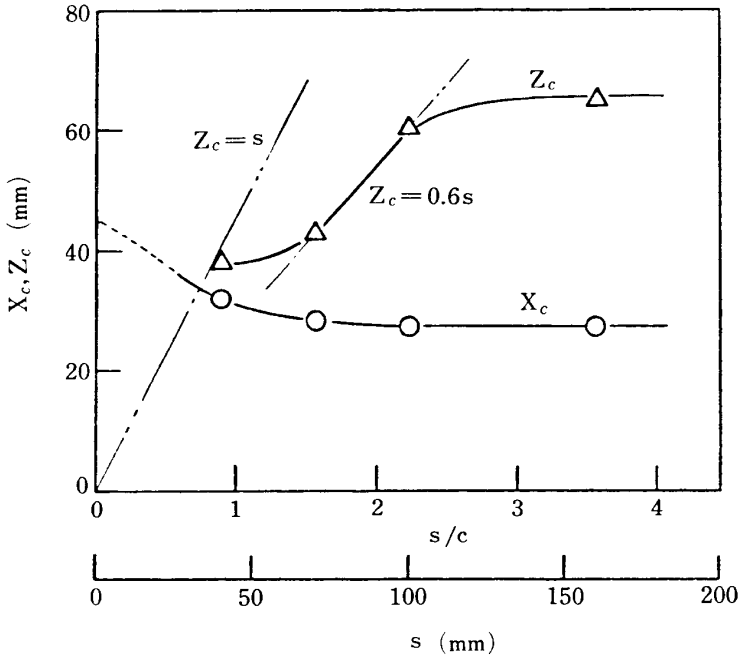


FIG. 4-24. Effect of span on correlation lengths; $t\times c=5\times 45$, $\alpha=30°$, $U=40$ m/s, $x/c=0.356$, $z=0$.

30°, $X_c=0.5c$, $Z_c=1.3c$ at $\alpha=60°$ and $X_c=0.5c$, $Z_c=1.0c$ at $\alpha=90$. On the upstream surface, they take larger values than those on the separated surface.

(3) The correlation area is also uniformly distributed over the large part of the plate surface, taking $A_c/c^2=0.62$ at $\alpha=30°$, 0.51 at $\alpha=60°$ and 0.39 at $\alpha=90°$. On the upstream surface, they take a larger value of about twice that on the separated surface.

4-4 *Noise source strength*

The associated acoustic strength can be evaluated by Eq. (9) with the mean-square

time derivatives of wall-surface pressure and the correlation area obtained in the preceding sections. For the purpose, it is convenient to introduce an expression of the source strength in decibel since the mean-square of surface-pressure time-derivatives (DPIL) are expressed in decibel. Taking a reference strength $Q_0=A_{c0}\cdot\overline{\dot{p}_{s0}^2}$, the source strength level can be defined as

$$QIL(\mathrm{dB})=10\log\frac{Q}{Q_0}=10\log\frac{A_c\overline{\dot{p}_s^2}}{A_{c0}\overline{\dot{p}_{s0}^2}}. \tag{15}$$

Since

$$DPIL(\mathrm{dB})=10\log\frac{\overline{\dot{p}_s^2}}{\dot{p}_{s0}^2}\qquad(\dot{p}_{s0}^2=(2\pi f_0)\dot{p}_{a0}^2,\ f_0=1000\ \mathrm{Hz})$$

the source strength level can be expressed as

$$QIL(\mathrm{dB})=10\log A_c/A_{c0}+DPIL(\mathrm{dB}). \tag{16}$$

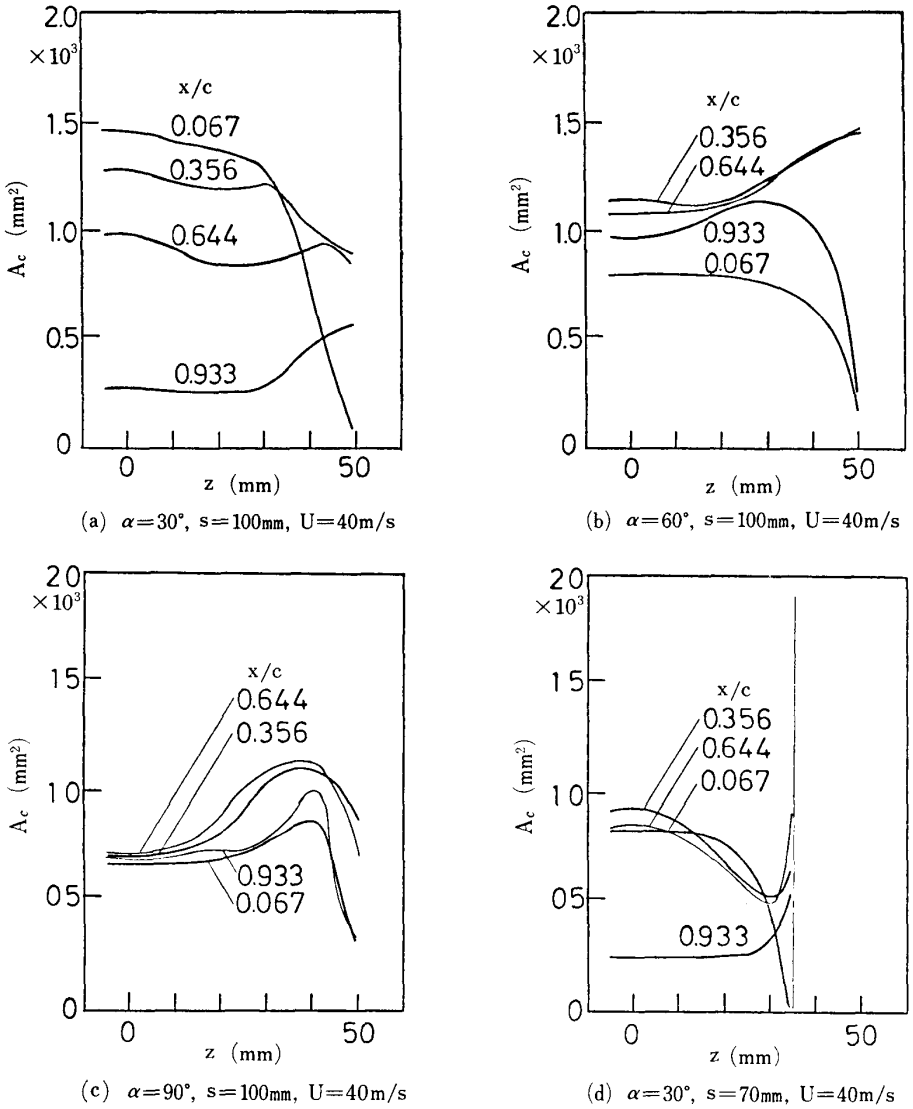


(a) $\alpha=30°$, s=100mm, U=40m/s

(b) $\alpha=60°$, s=100mm, U=40m/s

(c) $\alpha=90°$, s=100mm, U=40m/s

(d) $\alpha=30°$, s=70mm, U=40m/s

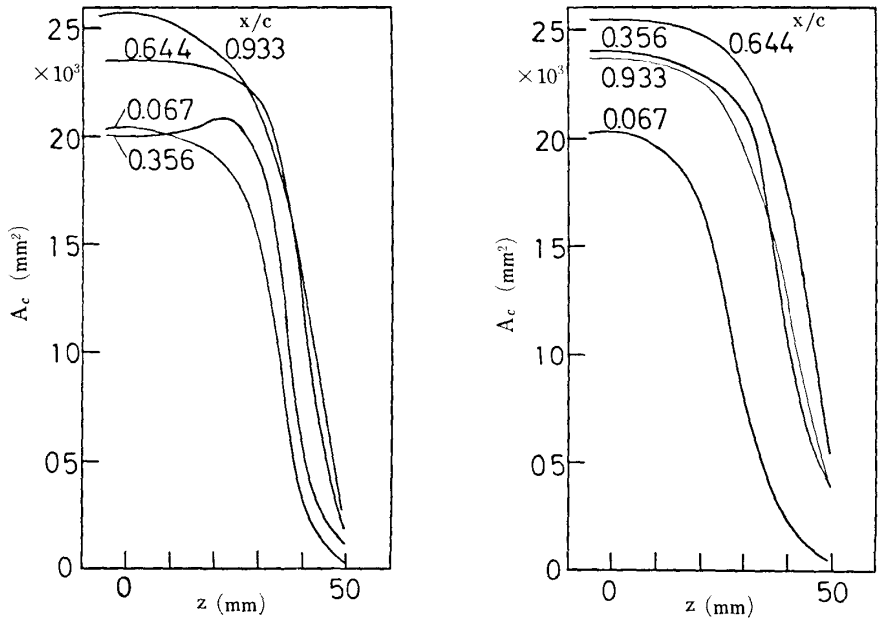


(e) Upstream surface, $\alpha=30°$, s=100mm, U=30m/s

(f) Upstream surface, $\alpha=60°$, s=100mm, U=30m/s

FIG. 4–25. Correlation area of surface-pressure time-derivatives; $t\times c=5\times 45$.

In the following figures, $A_{c0}=1$ mm² is chosen.

The source strength levels obtained in this way are presented in Figs. 4–26(a) to (f). In the spanwise direction, the source strength is uniformly distributed. Close to the leading edge, the source has slightly stronger strength than that near the trailing edge. The distributions are little affected by the attack angle and the span length. On the upstream surface, there are also the effective sources distributed as shown in Figs. 4–2(e) and (f). These strengths are of the same order as those on the separated surface.

The effect of the flow velocity on the source strength can be evaluated by the fact that only the mean-square of surface-pressure time-derivative is a function of the flow velocity, being proportional to the sixth power of it.

4–5 *Prediction of acoustic intensity*

With the source strength distribution obtained, the associated acoustic intensity can be predicted and compared with the experimental result. The far-field sound pressure level is given by

$$SPL(\mathrm{dB})=10\log\frac{\overline{p_a^2}}{p_{a0}^2}.$$

With Eqs. (8) and (16), it can be expressed as

$$SPL(\mathrm{dB})=20\log\frac{f_0\cos\chi}{2ar}+10\log\int_A A_c(x,z)10^{DPIL(x,z)/10}dxdz. \qquad (17)$$

The predicted sound pressure levels with the data of $A_c$ and $DPIL$ obtained in the

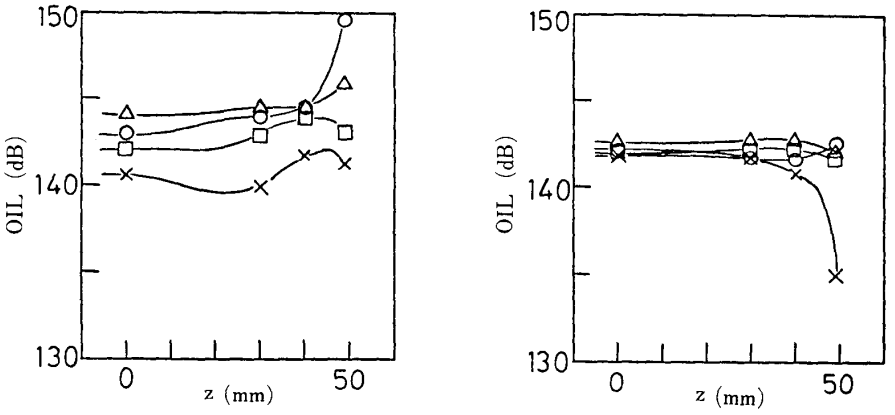


(a) $\alpha=30°$, s=100mm, U=40m/s (b) $\alpha=60°$, s=100mm, U=40m/s

○:x/c=0.067, △:x/c=0.356, □:x/c=0.644, ×:x/c=0.933

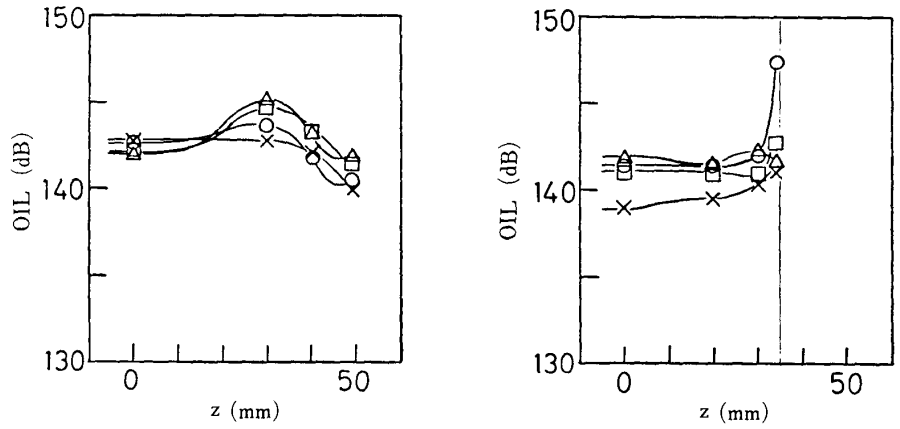


(c) $\alpha=90°$, s=100mm, U=40m/s (d) $\alpha=30°$, s=70mm, U=40m/s

○:x/c=0.067, △:x/c=0.356, □:x/c=0.644, ×:x/c=0.933

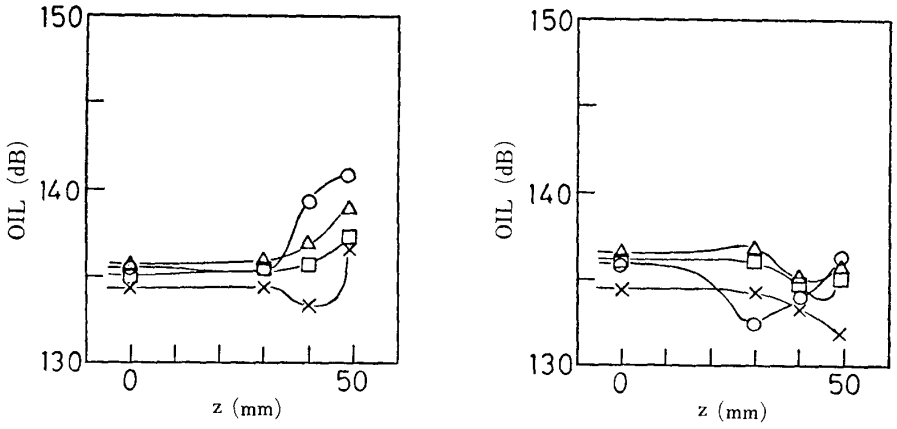


(e) Upstream surface, $\alpha=30°$, s=100mm, U=30m/s (f) Upstream surface, $\alpha=60°$, s=100mm, U=30m/s

○:x/c=0.067, △:x/c=0.356, □:x/c=0.644, ×:x/c=0.933

FIG. 4–26. Noise-source strength distribution; $t\times c=5\times 45$.

TABLE 1. Predicted sound pressure level; $t\times c=45$, $r=2m$.

| Span $s$ mm | Attack angle $\alpha°$ | Surface | Predicted SPL (dB) | | |
|---|---|---|---|---|---|
| | | | $U$ m/s 30 | 40 | 100 |
| 100 | 30 | separated | | 58.1 | 82.0 |
| 100 | 30 | upstream | 49.3 | 56.8 | 80.7 |
| 100 | 60 | separated | | 58.0 | 81.9 |
| 100 | 60 | upstream | 50.0 | 57.4 | 81.3 |
| 100 | 90 | separated | | 58.5 | 82.4 |
| 70 | 30 | separated | | 54.5 | 78.4 |

TABLE 2. Measured sound pressure level; $t\times c=5\times 45$, $s=84$ mm, $U=100$ m/s, $r=2$ m.

| $\alpha°$ | 30 | 60 | 90 |
|---|---|---|---|
| $SPL_m$ (dB) | 86.4 | 87.8 | 90.2 |

TABLE 3. Comparison between measured and predicted sound pressure levels; $t\times c=5\times 45$, $r=2$ m.

| $\alpha°$ | Predicted $SPL_p$ | | Difference (dB) |
|---|---|---|---|
| | $U=40$ m/s | $U=100$ m/s | $SPL_p-SPL_m$ |
| 30 | 60.5 | 84.4 | −2 |
| 60 | 61.0 | 84.9 | −3 |

preceding section are shown in Table 1. The integral on the right hand of Eq. (17) was obtained by a numerical integration by $\Delta x=6.5$ mm and $\Delta z=5$ mm steps. The levels at higher velocities were predicted with the sixth power relation of $\overline{p_s^2}$ to the flow velocity. The sound pressure levels to be compared with are presented in Table 2. The comparison of both values are found in Table 3, in which for the predicted values the contribution of both surfaces, separated and upstream, is taken into account. Figure 4–27 illustrates the comparison. The predicted values are always about 2 dB lower than the experimental values. The errors associated with calculation in the correlation area due to $\pm 15\%$ variation in the correlation coefficients may be estimated to be within $\pm 1.8$ dB, and those with measuring the fluctuating-pressure time-derivatives are $\pm 0.5$ dB. The sum of both errors is about $\pm 2.5$ dB. The difference between the predicted and experimental values can be considered to be within the level of these errors. The contribution of the non-uniform distributions of $A_c$ and $\overline{p_s^2}$ due to the end-plate effect to the predicted values is not so appreciable to be corrected strictly, being about 0.6 dB lower for the uniform distributed sources.

In the above prediction, since $A_c$ is proportional to $c^2$, the acoustic intensity should be proportional to $c^3$ in the case of $s/c\gtrsim 2$. Approximately, the correlation area and

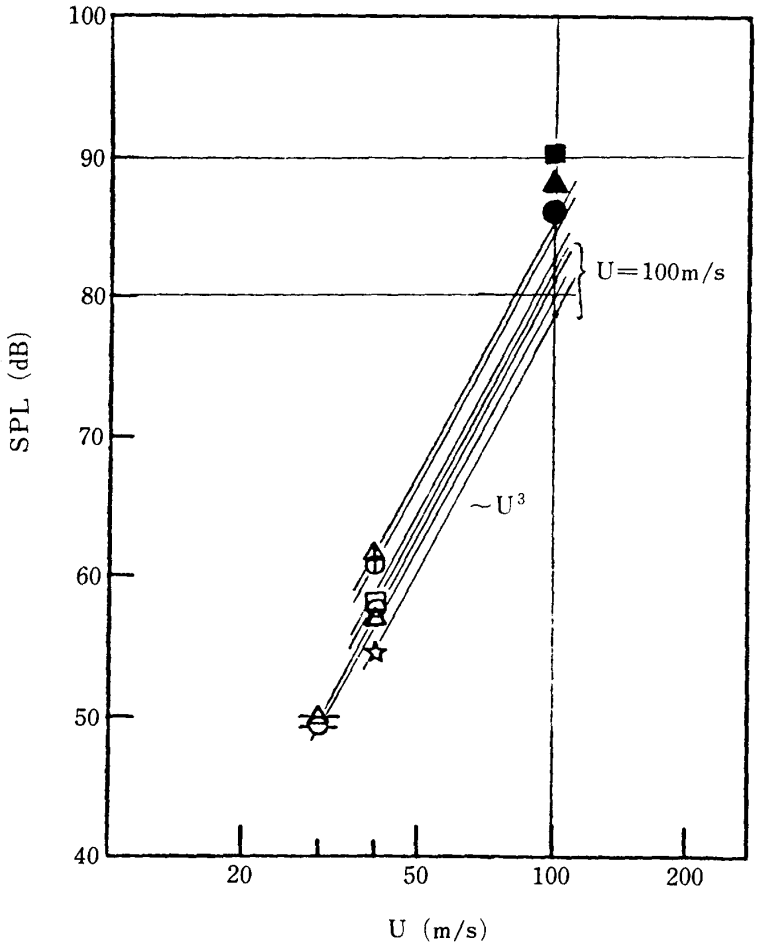


Predicted
- ○ : $\alpha=30°$, s=100mm, U= 40m/s, S
- ⊖ : $\alpha=30°$, s=100mm, U= 30m/s, U
- ⊕ : $\alpha=30°$, s=100mm, U= 40m/s, S,U
- △ : $\alpha=60°$, s=100mm, U= 40m/s, S
- ⟡ : $\alpha=60°$, s=100mm, U= 30m/s, U
- ◬ : $\alpha=60°$, s=100mm, U= 40m/s, S,U
- □ : $\alpha=90°$, s=100mm, U= 40m/s, S
- ☆ : $\alpha=30°$, s=100mm, U= 40m/s, S

Measured
- ● : $\alpha=30°$, s= 84mm, U=100m/s
- ▲ : $\alpha=60°$, s= 84mm, U=100m/s
- ■ : $\alpha=90°$, s= 84mm, U=100m/s

NB. S, Separated surface; U, Upstream surface

FIG. 4-27. Predicted sound intensity; $t\times c=5\times 45$, $r=2$ m, $\chi=0°$.

the mean-square of surface-pressure time-derivatives can be considered to be constant over the surface. Then, the associated sound pressure level is given by

$$SPL\,(\mathrm{dB})=20\log\left(\frac{f_0\cos\chi}{2ar}\right)+10\log\left(A\cdot A_c\right)+DPIL\,(\mathrm{dB}) \qquad (18)$$

In the case of $\alpha=30°$, $DPIL=113$ dB ($QIL=144$ dB), $X_c=0.6c$, $Z_c=1.3c$ ($A_c=1.27\times 10^2$ mm$^2$) lead to

$$SPL = 81.8\ \mathrm{dB}$$

which is close to the strictly predicted value.

## 5. Conclusion

Noise associated with separated flow of a flat plate was studied experimentally to obtain its acoustic characteristics and to understand its generation mechanism. From the acoustic features, it was found that the separated flow noise should be attributed to the wall-pressure fluctuation on the plate surface, being of the acoustic dipole source. By investigating the correlation of the acoustic pressure with the wall-surface pressure, the time derivative of the latter has been shown to have the dominant contribution to the associated acoustic radiation. Finally, of the surface-pressure time-derivatives, the intensity, frequency spectrum and cross-correlation were measured to evaluate the acoustic source strength distributed over the plate surface, and with these the associated noise field was predicted to be compared with the experimental result.

*Acoustic characteristics*

(1) The associated acoustic intensity is proportional to the sixth power of the oncoming flow velocity, having the directivity of the acoustic dipole source.

(2) The frequency spectrum is of a broad-band, taking a peak at the frequency of 0.3 nondimensionalized with the flow velocity and the chord length.

*Generation mechanism*

(1) With the acoustic pressure, the time derivative of the surface-pressure has a strong correlation but the surface-pressure itself has little correlation.

(2) In the separated flow, the correlation of the pressure in flow and its time-derivative with the acoustic pressure becomes higher as close to the surface wall, being independent of the turbulent velocity fluctuation.

(3) Consequently, the associated acoustic radiation can be attributed to the surface-pressure fluctuation on the plate surface.

*Noise source strength*

(1) The noise source strength is thus proportional to the mean-square time-derivative of surface pressure and its correlation area.

(2) The mean-square time-derivative is proportional to the sixth power of the oncoming flow velocity.

(3) The spectral density of the surface-pressure time-derivative has a broad-band peak at the nondimensional frequency of $0.3 \sim 0.4$ based on the flow velocity and the chord length.

(4) The acoustic source strength is distributed uniformly in the chordwise and spanwise directions, being slightly stronger close to the leading edge.

(5) These effective acoustic sources are also distributed over the upstream surface of the plate as well as over the separated surface due to the propagation of the fluctuating pressure on the latter to the former. The strengths on both surfaces are of the same order.

(6) For plates with the span longer than twice the chord, the correlation area of the surface-presssure time-derivative is a function of the chord length, being independent of the flow velocity; $0.62c^2$ at $\alpha=30°$, $0.51c^2$ at $\alpha=60°$, and $0.39c^2$ at $\alpha=90°$. On the upstream surface, it takes larger values, about twice those on the separated surface. Thus, the acoustic intensity is proportional to the third power of the chord length.
(7) These noise-source strengths enable one to predict the associated acoustic field within the error of the experimental measurement.

## Acknowledgement

The authors wish to acknowledge the helpful experimental assistance provided by Mr. Isao Aoki and Mr. Katsumi Takeda and useful advice for instrumentation by Dr. Masamichi Yamashita. The authors are also indebted to Prof. Syojiro Kaji, Prof. Yoshimichi Tanida, Prof. Hiroyuki Takata and Prof. Hideo Tanaka for their helpful and valuable discussions in the course of this work.

*Department of Propulsion*
*Institute of Space and Aeronautical Science*
*University of Tokyo*
*22 December 1980*

## References

[1] N. Curle, The influence of boundaries upon aerodynamic sound, Proc. Roy. Soc. Lond. **A231**, 505 (1955).
[2] C. G. Gordon, Spoiler generated flow noise I. The experiment, J. Acous. Soc. Amer. **43**, 1041 (1968).
[2] C. G. Gordon, Spoiler generated flow noise II. Results, J. Acous. Soc. Amer. **45**, 214 (1969).
[4] F. R. Fricke and D. C. Stevenson, Pressure fluctuation in a separated flow region, J. Acous. Soc. Amer. **44**, 1189 (1968).
[5] T. E. Siddon, Surface dipole strength by cross-correlation method, J. Acous. Soc. Amer. **53**, 619 (1973).
[6] Y. Maruta, S. Kotake and K. Takeda, Noise from separated flow of flat plate, Proc. 1977 Tokyo Joint Gas Turbine Congr. 449 (1977).

## Appendix A Acoustic field of flows around solid bodies

The equation of continuity

$$\frac{\partial \rho}{\partial t}+\frac{\partial}{\partial x_i}(\rho u_i)=0$$

and the equations of momentum under no external forces

$$\frac{\partial}{\partial t}(\rho u_i)+\frac{\partial}{\partial x_j}(\rho u_i u_j+p\delta_{ij}-\tau_{ij})=0$$

may be cast into the form of Lighthill's wave equation

$$\frac{\partial^2\rho}{\partial t^2}-a^2\frac{\partial^2\rho}{\partial x_i\partial x_i}=\frac{\partial^2}{\partial x_i\partial x_j}(\rho u_iu_j+p\delta_{ij}-\tau_{ij}-a^2\rho\delta_{ij}). \tag{A-1}$$

Herein, $\rho$ is the density, $t$ the time, $a$ the speed of sound in the undisturbed medium, $x_i$ the space coordinates, $u_i$ the velocity, $p$ the pressure, $\tau_{ij}$ the viscous stress. The left hand side of this equation describes the propagation of sound in a medium at rest, while the right hand side may be regarded a collection of all-comprehensive source terms different from zero only in the flow region and describing a number of different effects such as generation, refraction and scattering of sound. The effective stress tensor is denoted by

$$T_{ij}=\rho u_iu_j-\tau_{ij}+(p-a^2\rho)\delta_{ij}. \tag{A-2}$$

The acoustic radiation from a flow region containing embedded surfaces of solid body is formally solved by this wave equation [*1*]. By using a Green function which satisfies the homogeneous equation of Eq. (A-1) and its boundary conditions;

$$\frac{\partial^2G}{\partial t^2}-a^2\frac{\partial^2G}{\partial x_i\partial x_i}=\delta(\boldsymbol{x}-\boldsymbol{y},t-t')\qquad G=\frac{\delta(t'-\tau)}{4\pi r}\qquad \tau=t-\frac{r}{a},\ r=|\boldsymbol{x}-\boldsymbol{y}| \tag{A-3}$$

the solution of Eq. (A-1) can be expressed as

$$\begin{aligned}\rho(\boldsymbol{x},t)=&\frac{1}{a^2}\int_{-T}^{T}\int_V G\frac{\partial^2T_{ij}}{\partial y_i\partial y_j}d\boldsymbol{y}dt'\\&+\int_{-T}^{T}\int_A\left\{G\left(\frac{\partial\rho}{\partial n}+\frac{u_n}{a^2}\frac{\partial\rho}{\partial t'}\right)-\rho\left(\frac{\partial G}{\partial n}+\frac{u_n}{a^2}\frac{\partial G}{\partial t'}\right)\right\}dsdt'\end{aligned} \tag{A-4}$$

where the density $\rho$ means the excess density relative to the ambient density in the radiation field, $V$ the volume of the flow region, $A$ the surface area and $y_n$ the normal vector onto the surface. After some manupulation, the above equation is reduced to

$$\begin{aligned}\rho(\boldsymbol{x},t)=&\frac{1}{a^2}\int_{-T}^{T}\int_V\frac{\partial^2G}{\partial y_i\partial y_j}T_{ij}d\boldsymbol{y}dt'\\&+\frac{1}{a^2}\int_{-T}^{T}\int_A\left\{\frac{\partial G}{\partial y_i}(-p\delta_{in}+\tau_{in})+\rho u_n\frac{\partial G}{\partial t'}\right\}dsdt'\end{aligned} \tag{A-5}$$

Substitutihg the Green function into the integrals gives

$$\begin{aligned}p(\boldsymbol{x},t)=a^2\rho(\boldsymbol{x},t)=&\frac{\partial^2}{\partial x_i\partial x_j}\int_{-T}^{T}\frac{\delta(t'-\tau)}{4\pi r}T_{ij}d\boldsymbol{y}dt'\\&-\frac{\partial}{\partial x_i}\int_{T-}^{T}\int^{A}\frac{\delta(t'-\tau)}{4\pi r}(-p\delta_{in}+\tau_{in})dsdt'+\int_{-T}^{T}\int_A\frac{\rho u_n}{4\pi r}\frac{\partial}{\partial t'}\delta(t'-\tau)dsdt'\end{aligned} \tag{A-6}$$

or taking $T\to\infty$

$$p(\boldsymbol{x}, t)=\frac{\partial^2}{\partial x_i \partial x_j}\int_V \frac{1}{4\pi r}[T_{ij}]dv+\frac{\partial}{\partial x_i}\int_A \frac{1}{4\pi r}[p\delta_{in}-\tau_{in}]ds+\int_A \frac{1}{4\pi r}\left[\frac{\partial \rho u_n}{\partial t}\right]ds \tag{A-7}$$

where $dv=d\boldsymbol{y}$ and [ ] denotes evaluation at the retarded time $\tau=t-r/a$. This is the Curle's generalized solution of the Lighthill wave equation [*1*]. The first integral is associated with noise generation by the effective stress $T_{ij}$, being turbulence-generated quadrupole noise. The last two integrals mean noise generation by interaction between the fluid and the surface as local resultant fluctuating stresses acting on the surface (the second integral) and fluctuating fluid motion by the surface movement itself (the third integral), being dipole and monopole noise sources, respectively.

If the body surfaces are stationary or in rigid steady motion ($u_n\equiv 0$), Eq. (A-7) gives

$$p=\frac{\partial^2}{\partial x_i \partial x_j}\int_V \frac{1}{4\pi r}[T_{ij}]dv+\frac{\partial}{\partial x_i}\int \frac{1}{4\pi r}[p\delta_{in}]ds\equiv p_v+p_s \tag{A-8}$$

where $p_v$ and $p_s$ denote the fluctuating pressures associated with the quadrupole *volume* source and the dipole *surface* source, respectively. With the relation

$$\frac{\partial}{\partial x_i}\left(\frac{[T_{ij}]}{r}\right)=-\frac{x_i-y_i}{r^3}[T_{ij}]-\frac{x_i-y_i}{r^2}\frac{1}{a^2}\left[\frac{\partial T_{ij}}{\partial t}\right]$$

these pressures are further rewritten as

$$\begin{aligned} p_v=&\int_V \frac{(x_i-y_i)(x_j-y_j)}{4\pi a^2 r^3}\left[\frac{\partial^2 T_{ij}}{\partial t^2}\right]dv+\int \frac{(x_i-y_i)(x_j-y_j)}{4\pi a r^4}\left[\frac{\partial T_{ij}}{\partial t}\right]dv\\ &+\int \frac{(x_i-y_i)(x_j-y_j)}{4\pi r^5}[T_{ij}]dv \qquad\qquad (A\text{-}9)\\ p_s=&-\int_A \frac{x_i-y_i}{4\pi r^3}[p\delta_{in}]ds-\int \frac{x_i-y_i}{4\pi a r^2}\left[\frac{\partial p}{\partial t}\delta_{ni}\right]ds. \end{aligned}$$

Since, of these terms, the propagative one in the far-field radiation is of the order of $r^{-1}$ and the nonpropagative one is of the higher order of $r^{-2}$, $r^{-3}$, they can be classified by their contribution to either far-field or near-field radiation, $p^{(f)}$ and $p^{(n)}$, respectively.

$$\begin{aligned} p^{(f)}\equiv&\int_V \frac{(x_i-y_i)(x_j-y_j)}{4\pi a^2 r^3}\left[\frac{\partial^2 T_{ij}}{\partial t^2}\right]dv+\int_V \frac{(x_i-y_i)(x_j-y_j)}{4\pi a r^4}\left[\frac{\partial T_{ij}}{\partial t}\right]dv\\ &-\int_A \frac{x_i-y_i}{4\pi a r}\left[\frac{\partial p}{\partial t}\delta_{in}\right]ds\equiv p_v^{(f)}+p_s^{(f)} \qquad (A\text{-}10)_f\\ p^{(n)}\equiv&\int_V \frac{(x_i-y_i)(x_j-y_j)}{4\pi a r^4}\left[\frac{\partial T_{ij}}{\partial t}\right]dv+\int_V \frac{(x_i-y_i)(x_j-y_j)}{4\pi r^3}[T_{ij}]dv\\ &-\int_A \frac{x_i-y_i}{4\pi r^3}[p\delta_{in}]ds\equiv p_v^{(n)}+p_s^{(n)}. \qquad (A\text{-}10)_n \end{aligned}$$

Hence, the associated pressure is written as

$$p=p^{(n)}+p^{(f)}\simeq p^{(n)}+\frac{r}{a}\frac{\partial p^{(n)}}{\partial t}. \tag{A-11}$$

The acoustic pressure in the far-field is then

$$p_a=p^{(f)}=\frac{r}{a}\dot{p}^{(n)} \tag{A-12}$$

which leads to Eq. (1).

In the flow region, the near-field pressure is dominant;

$$p_v\simeq p^{(n)} \qquad |p^{(n)}|\gg|p^{(f)}|. \tag{A-13}$$

Hence, the acoustic pressure has little correlation with the pressure itself in the flow region due to this masking effect of the near-field pressure,

$$\langle p_v p_a\rangle=\langle p^{(n)}p_a\rangle=0 \tag{A-14}$$

In order to make the flow pressure correlate with the acoustic pressure, Eq. (A-12) should be employed as

$$\langle p_a p_a\rangle=\frac{r}{a}\langle\dot{p}^{(n)}p_a\rangle=\frac{r}{a}\{\langle\dot{p}_v^{(n)}p_a\rangle+\langle\dot{p}_s^{(n)}p_a\rangle\}. \tag{A-15}$$

In the present study, these correlations of fluctuating pressures in the separated flow are observed and shown in Figs 3–6, 3–8 and 3–10, for $\langle p_f p_f\rangle$, $\langle\dot{p}_f\dot{p}_f\rangle$ and $\langle\dot{p}_f p_a\rangle$, respectively. With Eq. (A-12), they correspond to $\langle p^{(n)}p^{(n)}\rangle$, $\langle\dot{p}^{(n)}\dot{p}^{(n)}\rangle$ and $\langle\dot{p}^{(n)}p_a\rangle$, respectively. From Figs. 3–6 and 3–8,

$$|p_v^{(n)}|\gg|p_s^{(n)}|, \qquad |\dot{p}_v^{(n)}|\gg|\dot{p}_s^{(n)}| \tag{A-16}$$

However, the result shown in Fig. 3–10 implies

$$\langle\dot{p}_s^{(n)}p_a\rangle\gg\langle\dot{p}_v^{(n)}p_a\rangle \tag{A-17}$$

that is

$$\langle p_s^{(f)}p_a\rangle\gg\langle p_v^{(f)}p_a\rangle. \tag{A-18}$$

Consequently, the contribution of turbulence-generated quadrupole source is much less than that of fluctuating surface-pressure dipole source, and the associated noise of flow separation could be attributed mainly to surface-pressure fluctuations.

## Appendix B Correlation of signals from probe-microphone

(1) Frequency response of a probe-microphone

A probe-tube and microphone system has been utilized successfully for measurement of fluctuating pressures in flows or on the wall surface. Its use is, however,

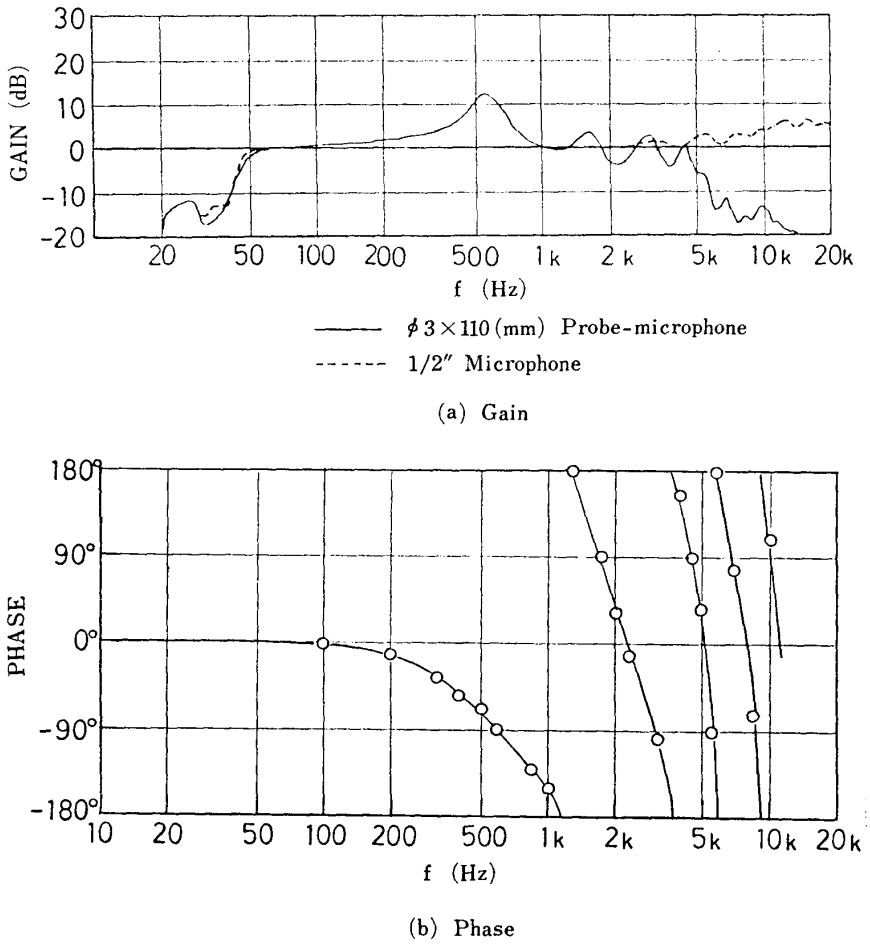


FIG. B-1. Frequency response of probe-microphone.

limited in the frequency range due to its frequency response. The response characteristics are determined by the resonant frequencies of the system and the viscous damping of high-frequency sounds. The former defect can be improved by adjusting the probe length and cavity or inserting absorptive materials of standing sound waves. For the frequency range up to 6 kHz, however, these methods scarcely provides appreciable improvement. Then, care should be taken only for less damping of high-frequency sounds due to the viscous effect. In the present study, a pipe of 3 mm in inner diameter and 110 mm long was employed. The size of the pinhole on the wall surface also is a matter of importance. Large size holes are favorable for reducing the high-frequency damping whereas small holes has higher resolution of local pressure fluctuations. By referring to W. W. Willmarth's study on "resolution and structure of the wall-pressure field beneath a turbulent boundary layer" (J. Fluid Mech. *22*, 81 (1965)), the pinhole size of 0.7 mm in diameter was selected after several tests. The final configuration of probe-microphone is shown in Fig. 3–2. The gain and phase characteristics of frequency response are shown in Fig. B-1. These were obtained by the method of pure-tone response. Alternatively, by using a white noise, the transfer function of frequency response may be obtainable. Consider the output signal of the probe-microphone $y(t)$ corresponding to an input of

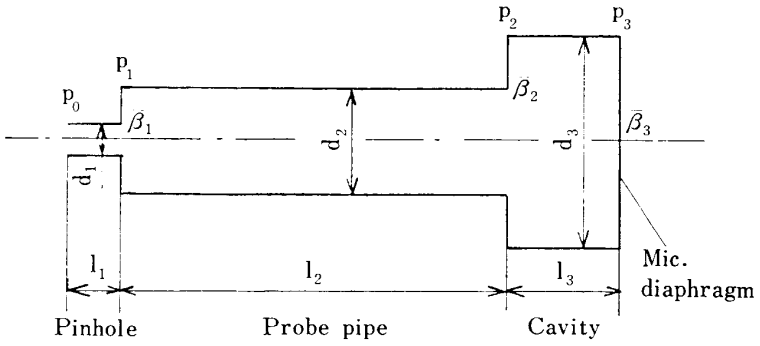


FIG. B-2. Linear acoustic model of probe-microphone.

white noise, $x(t)$. They are related with a transfer function $G(\omega)$ in the frequency space

$$Y(\omega)=G(\omega)\cdot X(\omega) \tag{B-1}$$

where $X(\omega)$ and $Y(\omega)$ are Fourier transforms of $x(t)$, and $y(t)$, respectively. The cross-correlation between two signals, $x(t)$ and $y(t)$, gives

$$\langle Y(\omega)X^*(\omega)\rangle = G(\omega)\langle X(\omega)X^*(\omega)\rangle$$

where $Y(\omega)X^*(\omega)$ is the frequency spectrum of correlation $\langle xy\rangle$, $\Phi_{xy}(\omega)$ and $\langle X(\omega)X^*(\omega)\rangle$ is that of autocorrelation $\langle xx\rangle$, $\Phi_{xx}(\omega)$. Thus,

$$G(\omega)=\frac{\Phi_{xy}(\omega)}{\Phi_{xx}(\omega)}. \tag{B-2}$$

The frequency response of the probe-microphone can also be expressed in a form of analytical function by the linear acoustic theory. Assume the geometrical configuration of the probe-microphone as shown in Fig. B-2. Herein, $d$ is the inner diameter, $l$ the length, and $\beta$ the admittance at the boundary of cross-section ($\beta\equiv\rho_0 au/p$). The acoustic pressure $p$ and the particle velocity $u$ of the plane wave of frequency $\omega$ in a pipe are written by

$$\begin{aligned} p(x,t)&=(Ae^{ikx}+Be^{-ikx})e^{i\omega t}\\ u(x,t)&=\frac{1}{\rho_0 a}(Ae^{ikx}-Be^{-ikx})e^{i\omega t} \end{aligned} \tag{B-3}$$

where $x$ is measured from the pipe end and $k$ the wave number ($=\omega/a$). With the boundary conditions at $x=0$ and $x=l$

$$\begin{aligned} p(0,t)&=p_1 e^{i\omega t}\\ p_2&=-\frac{\rho_0 a}{\beta_2}u_2. \end{aligned} \tag{B-4}$$

Eq. (B-3) gives

$$p_2 = p_1 (\cos kl_2 - i\beta_2 \sin kl_2)^{-1}.$$

In this way, the pressure ratios are obtained as

$$\begin{aligned} \frac{p_0}{p_1} &= \cos kl_1 - i\beta_1 \sin kl_1 \\ \frac{p_1}{p_2} &= \cos kl_2 - i\beta_2 \sin kl_2 \\ \frac{p_2}{p_3} &= \cos kl_3 - i\beta_3 \sin kl_3 \end{aligned} \tag{B-5}$$

and the admittances are

$$\begin{aligned} \beta_1 &= -\left(\frac{d_2}{d_1}\right)^2 \frac{\tan kl_2 + i\beta_2}{\beta_2 \tan kl_2 + i} \\ \beta_3 &= -\left(\frac{d_3}{d_2}\right)^2 \frac{\tan kl_3 + i\beta_3}{\beta_3 \tan kl_3 + i} \\ \beta_3 &= 0 \end{aligned} \tag{B-6}$$

where at the microphone surface zero admittance is assumed. The transfer function of the input $p_0$ to the output $p_3$, $G(\omega)$, can be obtained by

$$G(\omega) = \frac{p_3}{p_0} = \frac{p_1}{p_0}\frac{p_2}{p_1}\frac{p_3}{p_2}. \tag{B-7}$$

In practice, however, the viscous damping and acoustic inertia at open ends should be corrected appropriately. For the present system shown in Fig. 3–2, the transfer function well-fitted to Fig. B-1 is obtainable with the following parameters

$$\begin{aligned} &l_1 = 0.5\ \text{mm} \quad && l_2 = 125\ \text{mm} \quad && l_3 = 0.7\ \text{mm} \\ &d_1 = 0.7\ \text{mm} \quad && d_2 = 3\ \text{mm} \quad && d_3 = 12.7\ \text{mm} \\ &\beta_3 = 0.01i \quad && \gamma = 4.09 \times 10^4 + 1.82 \times 10^{-7} f(\text{Hz}) \end{aligned}$$

where $\gamma$ is a correction for viscous damping in the form

$$k = \omega/a + i\pi\gamma$$

(2) Correlation of signals from probe-microphone

The relation of the output signal of a probe-microphone, $y(t)$, to an input signal, $x(t)$, can be expressed by

$$y(t) = \int_{-\infty}^{\infty} g(\tau)x(t-\tau)d\tau \tag{B-8}$$

where $g(\tau)$ is a weight function, or in Fourier transform,

$$Y(\omega) = G(\omega)X(\omega) \tag{B-9}$$

where $X(\omega)$, $Y(\omega)$ and $G(\omega)$ are Fourier transforms of $x(t)$, $y(t)$ and $g(t)$, respectively;

$$X(\omega)=\int_{-\infty}^{\infty} x(t)e^{-i\omega t}dt \quad Y(\omega)=\int_{-\infty}^{\infty} y(t)e^{-i\omega t}dt \quad G(\omega)=\int_{-\infty}^{\infty} g(t)e^{-i\omega t}dt \quad \text{(B-10)}$$

Consider the correlation between two signals $x_1(t)$ and $x_2(t)$ of which the outputs through a microphone with a transfer function $G(\omega)$ are $y_1(t)$ and $y_2(t)$, respectively. They have the relation

$$Y_1(\omega)=G(\omega)X_1(\omega) \qquad Y_2(\omega)=G(\omega)X_2(\omega). \qquad \text{(B-11)}$$

The cross correlation of two signals gives

$$\langle Y_1(\omega)Y_2^*(\omega)\rangle = G(\omega)G^*(\omega)\langle X_1(\omega)X_2^*(\omega)\rangle.$$

Thus, the frequency spectrum of the cross correlation can be given by

$$\langle X_1(\omega)X_2^*(\omega)\rangle = \frac{\langle Y_1(\omega)Y_2^*(\omega)\rangle}{G(\omega)G^*(\omega)} \qquad \text{(B-12)}$$

and the cross correlation by

$$\langle x_1(t)x_2(t+\tau)\rangle = \int_{-\infty}^{\infty} \frac{\langle Y_1(\omega)Y_2^*(\omega)\rangle}{G(\omega)G^*(\omega)} e^{i\omega\tau}d\omega. \qquad \text{(B-13)}$$

If the one is a direct output of the microphone as in the case of Chapter 3,

$$Y_3(\omega)=X_3(\omega)$$

Eq. (B-12) is reduced to

$$\langle X_1(\omega)X_3^*(\omega)\rangle = \frac{\langle Y_1(\omega)Y_3^*(\omega)\rangle}{G(\omega)} \qquad \text{(B-14)}$$

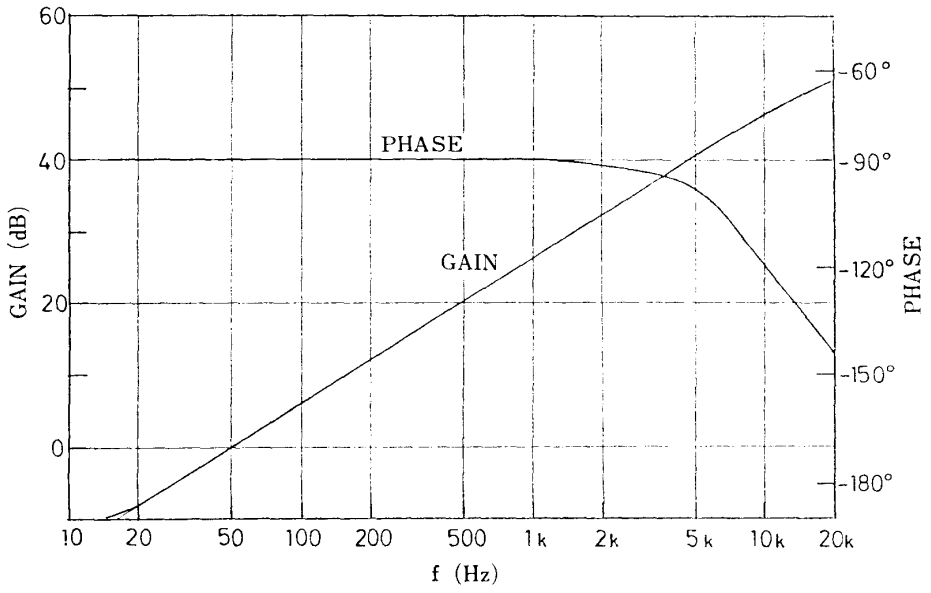


FIG. B-3. Frequency response of differentiator.

and the cross correlation is then

$$\langle x_1(t)x_3(t+\tau)\rangle = \int_{-\infty}^{\infty} \frac{\langle Y_1(\omega)Y_3^*(\omega)\rangle}{G(\omega)} e^{i\omega\tau} d\omega \tag{B-15}$$

The practical procedure for calculation of cross correlation by a computer used in the present study is as follows.

1. Set the number of sampling point ($=512$), the sampling time $\Delta t (=20\sim 50\,\mu s)$, the sampling cycle ($=50\sim 100$), and the window factor for spectrum.
2. Generate and store sine and cosine functions.
3. Generate and store a sine signal of 4 dB as a reference signal.
4. Calculate and store the transfer function $G(\omega)$ and $G^*(\omega)$ by measuring the output of the microphone $y(t)$ and its input $x(t)$ by the relation Eq. (B-2).
5. Input signals $y_1(t)$ and $y_2(t)$ or $y_3(t)$ and calculate the frequency spectrum of their correlation $\langle Y_1(\omega)Y_2^*(\omega)\rangle$ or $\langle Y_1(\omega)Y_3^*(\omega)\rangle$.
6. Calculate the frequency spectrum of the correct correlation $\langle X_1(\omega)X_2^*(\omega)\rangle$ by Eq. (B-12) or $\langle X_1(\omega)X_3^*(\omega)\rangle$ by Eq. (B-14).
7. Calculate their inverse Fourier transform and obtain the correlation $\langle x_1(t)x_2(t+\tau)\rangle$ by Eq. (B-13) and $\langle x_1(t)x_3(t+\tau)\rangle$ by Eq. (B-15).

To obtain the time-derivative of the surface pressure, an analog differentiator was used. Its frequency response is shown in Fig. B-3. It operated favorably within the frequency range between 20 Hz and 6 kHz.